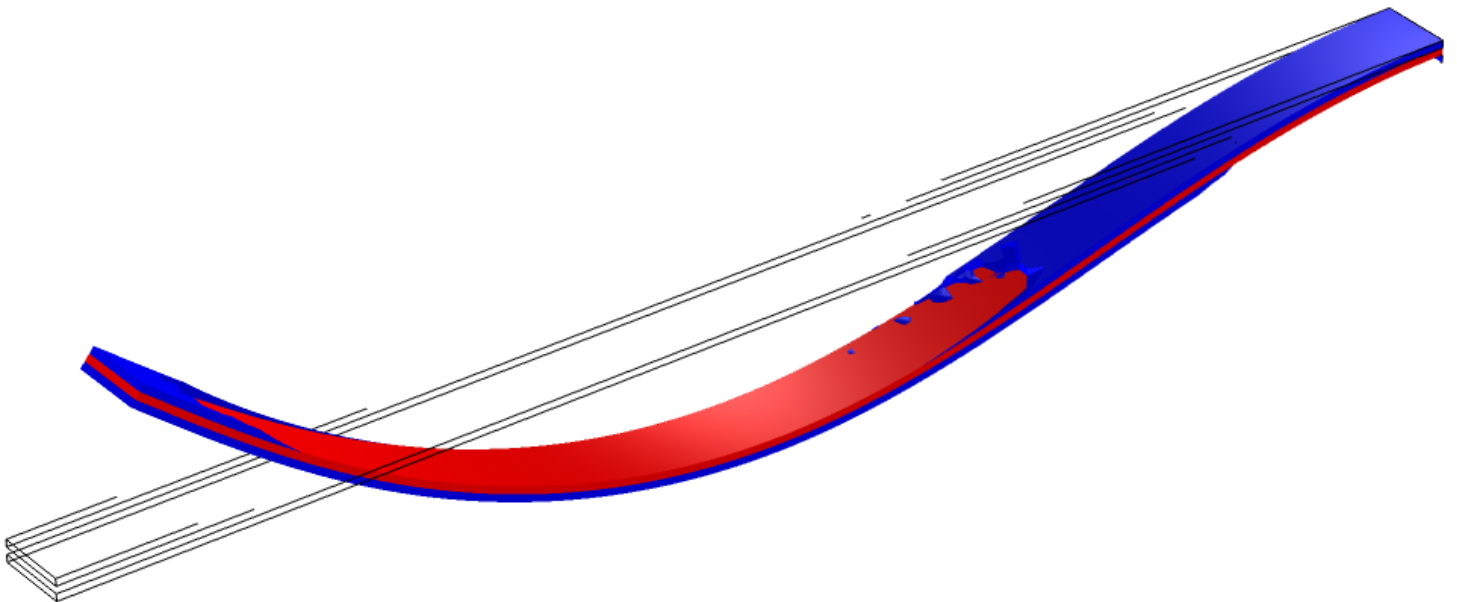


**Department of Precision and Microsystems Engineering**

**Topology Optimization for 4D-Printed Structures**

SARA ANNA PAKVIS

Report no : 2021.014  
Coach : dr.ir. Matthijs Langelaar  
Specialisation : Engineering Mechanics  
Type of report : Master Thesis  
Date : February 16, 2021





# TOPOLOGY OPTIMIZATION FOR 4D-PRINTED STRUCTURES

by  
Sara Anna Pakvis

A thesis submitted to  
Delft University of Technology,  
Mechanical, Maritime and Materials Engineering (3ME),  
Precision and Microsystems Engineering (PME).

In partial fulfillment of the requirements for the degree of  
Master of Science,

to be defended publicly on March 3rd, 2021 at 09:00.

Thesis committee:

Dr. Ir. Matthijs Langelaar (Delft University of Technology, PME)  
Dr. Ir. Ron van Ostayen (Delft University of Technology, PME)  
Dr. Ir. Giulia Scalet (University of Pavia, Department of Civil Engineering and Architecture)  
Ir. Stijn Koppen (Delft University of Technology, PME)

An electronic version of this thesis is available at [repository.tudelft.nl](https://repository.tudelft.nl).

# Preface

This thesis is a final work for the degree of Master of Science at the faculty of Mechanical, Maritime and Materials Engineering at Delft University of Technology, titled “Topology Optimization for 4D-Printed Structures”. In this work, the possibilities of combining topology optimization with 4D-printing are explored.

I sincerely express my gratitude towards my thesis supervisor dr.ir. Matthijs Langelaar for his good advice, guidance and support during the thesis project. Also, my thanks go to prof.dr.ir. Ferdinando Auricchio, dr.ir. Giulia Scalet, and dr.ir. Stefania Marconi of the University of Pavia in Italy, for sharing their expertise in 4D-printing as well as for their efforts in realizing experiments with printed structures.

The project has, in addition to this thesis, resulted in a paper titled “Modeling, Topology Optimization and Experimental Validation of Glass-Transition-Based 4D-Printed Polymeric Structures” written in cooperation with Giulia Scalet, Stefania Marconi, Ferdinando Auricchio and Matthijs Langelaar. It is to be submitted to the *11th Int. Conference on Couple Problems in Science and Engineering (COUPLED 2021)*. The conference will be held in Chia Laguna, South Sardinia, Italy on 13-16 June, 2021. I would like to thank the co-authors for their contributions to the paper.

Last but not least I would like to thank Lars, my family, and my friends for their support.

*Sara Anna Pakvis  
February 2021*

# Abstract

In recent developments in the field of multi-material additive manufacturing, differences in material properties are exploited to create printed shape memory structures, which are referred to as 4D-printed structures. New printing techniques allow for the introduction of prestresses in the specimen during manufacturing, such that the need for programming is omitted. This thesis focuses on bi-polymer 4D-printed structures, where the transformation process is based on a heat-induced glass transition in one of the materials, which is simulated by introducing a temperature-dependent stiffness in the material properties. The initial prestress is modeled into the other material. Upon the decrease in stiffness, the prestress is released, causing a bending behaviour. A methodology to find the design of 4D-printed structures is developed using a commercial software package, where a finite element model is combined with a density-based topology optimization method to describe the material layout. The objective of the optimization is to minimize the difference between a target displacement and the actual displacement. The linear elastic model coupled with geometrical nonlinearity is discretized by quadratic finite elements. This modeling approach is verified by a convergence analysis and validated by comparing its numerical results to analytical results of a bimorph beam model, published results, and experimental results.

The use of topology optimization to design 4D-printed structures is explored by applying the methodology to a variety of design problems. The approach can be expanded such that it matches the displacements of multiple points in the material domain to multiple target displacements. Another variation is to match an entire surface to a target function. Two-way transformation can be simulated using the modeling approach, by introducing a second prestress in the glassy polymer. Besides bending transformation, a twisting transformation can be obtained by changing the target displacement settings in the optimization. The number of layers can be expanded, such that the range of target displacements becomes larger. This way, more complex target shapes can be obtained, such as expanding lattices.

The prestress introduced by the printing process is dependent on many factors, which makes it difficult to predict. Bi-layer designs are printed and tests are performed, with the goal to find the prestress value and to further validate the modeling approach. Hereafter, the new prestress is used to generate, print and test topology optimized designs. Numerical and experimental results are compared to evaluate the performance of the modeling and topology optimization approach.

# Contents

<b>Preface</b>	<b>iii</b>
<b>Abstract</b>	<b>iv</b>
<b>1 Thesis Introduction</b>	<b>1</b>
1.1 Introduction . . . . .	1
1.2 Research Goal . . . . .	1
1.3 Reader's Guide . . . . .	1
<b>2 Topic Analysis</b>	<b>2</b>
2.1 4D-Printing . . . . .	2
2.1.1 Definition of 4D-printing . . . . .	2
2.1.2 Application fields . . . . .	2
2.1.3 Stimuli, mechanisms and materials . . . . .	3
2.1.4 Reversibility of 4D-transformation processes . . . . .	4
2.1.5 Bi-material 4D-printing with amorphous polymers . . . . .	5
2.1.6 Applying the pre-strain . . . . .	5
2.2 Overview of applications and demonstration devices of 4D-printing . . . . .	6
2.3 Topology Optimization in 4D-Printing . . . . .	7
2.3.1 Topology Optimization . . . . .	7
2.3.2 Level-Set methods . . . . .	8
2.3.3 Density-based methods . . . . .	9
2.3.4 Filtering and projection . . . . .	9
2.3.5 Objective function . . . . .	10
2.4 State-of-the-Art in topology optimization for 4D-printing . . . . .	11
2.4.1 Parabolic target shape simulation . . . . .	11
2.4.2 Adaptive wing simulation . . . . .	11
2.4.3 Active propeller simulation . . . . .	11
2.4.4 Self-folding origami simulation and experiment . . . . .	12
2.4.5 Soft actuator experiment . . . . .	12
2.4.6 Shape shifting lattice . . . . .	13
2.4.7 Composite beam experiment . . . . .	13
2.4.8 Complex composite structure experiments . . . . .	13
2.5 Research Scope . . . . .	14
<b>3 Development of the 2D-Model</b>	<b>17</b>
3.1 Model definition . . . . .	17
3.2 Physical modeling . . . . .	18
3.3 Convergence analysis . . . . .	21
3.4 Validation . . . . .	22
<b>4 Development of the 3D-Model</b>	<b>25</b>
4.1 Model definition . . . . .	25
4.2 Convergence analysis . . . . .	26
4.3 Validation . . . . .	27
<b>5 Topology optimization method</b>	<b>29</b>
5.1 Penalized Variables . . . . .	29
5.2 Objective Function . . . . .	29

5.3	Topology optimization results . . . . .	30
<b>6</b>	<b>Variations and Applications</b>	<b>32</b>
6.1	Optimal layer ratio geometry . . . . .	32
6.2	Two-way transformation . . . . .	32
6.3	Multiple probe points . . . . .	33
6.4	Shape matching . . . . .	34
6.5	Multiple active layers . . . . .	35
6.6	Topology optimization in active and passive layer (2D) . . . . .	36
6.7	Expanding lattice . . . . .	37
6.8	Twisting deformation (3D) . . . . .	38
<b>7</b>	<b>Experiments</b>	<b>40</b>
7.1	Experiment goal . . . . .	40
7.2	Sample specifications . . . . .	40
7.3	Printing process . . . . .	41
7.4	Method . . . . .	42
7.5	Results . . . . .	42
<b>8</b>	<b>Conclusion and Outlook</b>	<b>46</b>
8.1	Conclusion . . . . .	46
8.2	Future work . . . . .	47
	<b>Bibliography</b>	<b>49</b>
<b>A</b>	<b>Appendix</b>	<b>52</b>
A.1	Single material 4D-printing with amorphous polymers . . . . .	52
A.2	Genetic algorithm topology optimization methods . . . . .	52
A.3	Solver settings . . . . .	52
A.4	Research paper . . . . .	53

# Chapter 1

## Thesis Introduction

### 1.1 Introduction

Additive manufacturing or 3D-printing is a manufacturing technique where a material is deposited layer-wise to create three dimensional structures. The structures can be printed directly from computer-generated three dimensional model data. The main advantage of using 3D-printing is the ability to create very complex structures, which would be very difficult or even impossible to create using traditional manufacturing techniques. Using 3D-printing, customized parts can be created time- and cost-efficiently with minimized material losses. Since its invention in the 1980s, 3D-printing has evolved into a versatile and widely used method. It is used in application fields such as bio-mechanics, prototyping, and construction (Ngo et al., 2018). With the development of new 3D-printing methods, materials, and equipment over the past few decades, new possible applications arise. One of those newer applications is to use 3D-printing to create smart, responsive structures. This type of 3D-printing is referred to as ‘4D-printing’: a term initiated by the research group of Skylar Tibbits in 2014 (Tibbits, 2014). In this term, time is referred to as the fourth dimension. The initially printed structure evolves into a different configuration over time under the influence of a certain stimulus, such as heat, water, pH or electricity. This technique has some interesting application fields. Using 4D-printing, self-(dis)assembling, smart-behaving and self-repairing structures can be created (Momeni et al., 2017).

By carefully engineering the topology of the initial structure, a desired deformed structure can be obtained after 4D-transformation. However, to intuitively design an initial structure such that it deforms in the desired way is a non-trivial task. Therefore, combining 4D-printing with automated design approaches such as topology optimization seems promising. Topology optimization is a mathematical method which can be used to find the optimal material placement in a prescribed design domain, in order to obtain the best structural performance. It can potentially be used as a ‘design tool’ to create 4D-printed structures. To be able to use topology optimization in a 4D-printed structure, this structure should be modelled numerically, which is a challenge in itself. Some progress has already been made in the field of modeling 4D-printed structures in combination with topology optimization, and even a few experiments were done already. In the current state-of-the-art, material models that are used to model 4D-printing polymer structures are often rather complex. In order to be able to combine 4D-printing with topology optimization, the need for a simpler material model arises to reduce computation time and to allow for sensitivity analysis. To further reduce complexity, simpler topology optimization methods could be worth looking into.

### 1.2 Research Goal

The aim of this research project can be described as:

*“To explore the use of topology optimization to design 4D-printing structures”*

This final research goal can be divided in several smaller tasks:

- *Gathering context:* Background information about topology optimization in 4D-printing must be obtained, to get an insight in the state-of-the-art and research gaps to continue research.
- *Developing and validating a 2D modeling approach:* The development of the design tool should be done in steps of increasing complexity and, consequently, computation time. Therefore, the first step in developing is to create a model in 2D. An accurate, yet simple material model to describe the transforming behaviour

of printed structures should be found. Convergence studies will be performed to find the ideal mesh element size and order. After obtaining numerical results from simulations using the 2D-model, these numerical results will be validated using data from literature and analytical results.

- *Performing topology optimization in 2D*: Once a the 2D-model is developed and validated, a topology optimization method can be formulated to find the optimal initial printing structure for a given objective.
- *Developing and validating a 3D modeling approach*: Using the previously developed 2D-model, a more complex 3D-model can be created. Switching from 2D to 3D will introduce challenges that lead to changes in design choices of the model. The 3D-model will be validated using the same methods as for the 2D-model.
- *Performing topology optimization in 3D*: In 3D, more complex geometries can be achieved. Topology optimization will be performed on a variety of geometries, with different objective functions.
- *Validating the optimized designs in 3D*: Experimental validation can be used to validate the optimized designs. An experiment setup must be made where printed samples can be tested to gather experimental data.
- *Drawing conclusions*: Conclusions can be drawn from all the data gathered during this research. This will lead to a discussion and recommendations for further research in this field.

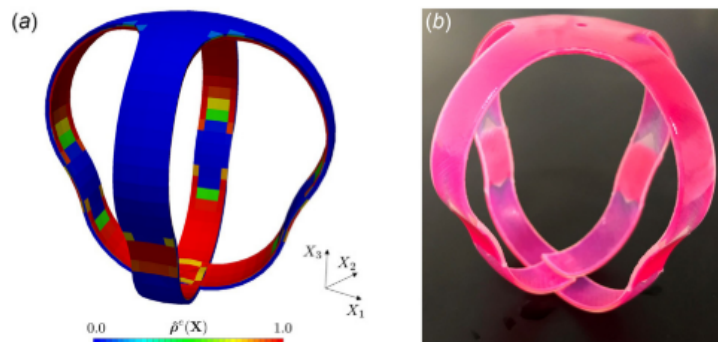


Figure 1.1: Optimized design of a 4D-printed gripper (Geiss et al., 2019), (a) Numerical design, (b) Printed design

### 1.3 Reader's Guide

The structure of this thesis is aligned with the tasks outlined above. To get a better understanding of the underlying principles of both 4D-printing and topology optimization, the fundamental ingredients of this research, a broader introduction to these topics is given in Chapter 2: *'Topic Analysis'*. This chapter also gives an overview of the current state-of-the-art. Following this, a more detailed and narrowed down research goal can be introduced, which will be given in Section 2.5: *'Research Scope'*. The design choices made during the development of the two-dimensional model are described in Chapter 3: *'Development of the 2D-Model'*. This chapter includes verification and validation of the modeling approach as well. In the next chapter, Chapter 4: *'Development of the 3D-Model'*, the difficulties that are introduced by switching from 2D to 3D and the changes that have been made to the preliminary model are discussed. The topology optimization method is introduced in Chapter 5: *'Topology Optimization Method'*. Some variations and applications of the 'standard' 2D- and 3D-models are given in Chapter 6: *'Variations and Applications'*. To be able to validate the optimized 3D designs, experimental data have to be obtained. The method to do so, along with the results will be presented in Chapter 7: *'Experiments'*. Chapter 8: *'Conclusion, Discussion and Future Work'* follows logically as the final chapter in this report. For the interested reader, a detailed description of how to implement the 2D- and 3D-model in the software package that was used during the project is given in the Appendix.

# Chapter 2

## Topic Analysis

### 2.1 4D-Printing

#### 2.1.1 Definition of 4D-printing

4D-printing is described as 3D-printing a structure with a targeted evolution (Tibbits, 2014; Momeni et al., 2017). Here, time is referred to as the fourth dimension. 4D-printed structures are sometimes referred to as printed smart materials (Sossou et al., 2019), printed active structures (Maute et al., 2015; Wu et al., 2016) and printed shape memory architectures (Ge et al., 2016). Their configuration changes upon exposure to a specific stimulus. Many sorts of stimuli are used, depending on the properties of the printed structure. Stimuli that are often used in practice are heat, water, electricity, magnetic field and pH.



Figure 2.1: An initially flat printed structure is transformed into a three-dimensional closed cube by submerging it into water, causing active material in the hinges to swell (Tibbits, 2014).

#### 2.1.2 Application fields

4D-printing is not presently used in existent products, but has many potential application fields. Four categories of those applications are self-assembly, smart functionality, self-disassembly and self-repair (Momeni et al., 2017). The reader should notice that the application fields in 4D-printing are overlapping those of traditional shape memory structures, which are not necessarily made with additive manufacturing. Therefore, some of the examples from the potential application fields originate from before the invention the term 4D-printing. Producing shape memory structures with additive manufacturing can allow for more complexity and therefore a wider range of applications.

- Self-assembling structures bring the advantage that the volume for storage and transport can be decreased. Once the structure has arrived at the desired location, it can be activated by the stimulus to achieve its final configuration. Some examples from the field are self-locking clamps (Inverardi et al., 2020), self-folding origami structures (Tolley et al., 2014), and self-deploying solar panels for spaceflight usage (Chen et al., 2019). Illustrations of these examples can be found in Figure 2.3 and Figure 2.4 respectively.
- 4D-printed structures are smart structures, meaning that they can act both as a sensor and an actuator at once. This can lead to a decrease in the number of parts and electronic circuits, which take up volume and can be prone to failure. According to Sydney Gladman et al. (2016), practical examples can especially be found in the biomedical field, such as drug delivery systems (Fernandes and Gracias, 2012; Melocchi et al., 2019) and 4D-printed medical stents (Bodaghi et al., 2016). In both of these examples, the change from room- to body temperature initiates the 4D-transformation.



Figure 2.2: Self-locking of a clamp (Inverardi et al., 2020)

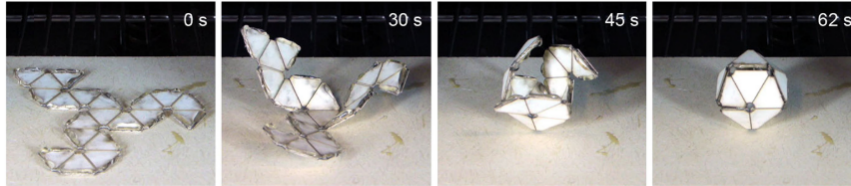


Figure 2.3: Self-assembling of a three-dimensional icosahedron by folding (Tolley et al., 2014)

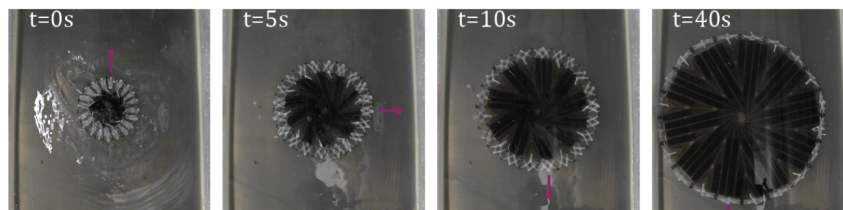


Figure 2.4: Self-assembling of a solar panel (Chen et al., 2019)

- Disassembly of products allows for separation of waste material and increases component reuse. 4D-printed structures that self-disassemble when exposed to a stimulus could be beneficial to the environment. A practical example is using snap-fit connections in shape memory polymers for self-disassembly (Willems et al., 2007; Carrell et al., 2011). In a snap-fit connection, two flexible parts are joined by pushing the interlocking components together. Here, one of the interlocking components deforms when exposed to heat, causing the parts to disconnect. This process is illustrated in Figure 2.5.

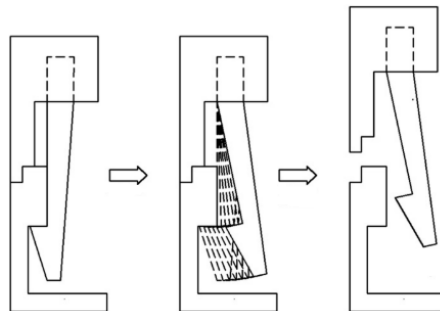


Figure 2.5: Heat activated release of a snap-fit connection (Carrell et al., 2011)

- 4D-printing can potentially be used to create self-repairing structures, by exploiting the self-repairing abilities of certain hydrogels. Some hydrogels create new molecular bonds when exposed to a stimulus such as light, pH or electricity (Taylor and in het Panhuis, 2016). A potential application is self-healing artificial tissue. Here, hydrogel scaffolds loaded with biological cells are 3D-printed to generate the artificial, self-healing tissue (Miao et al., 2017).

### 2.1.3 Stimuli, mechanisms and materials

Many different underlying principles or mechanisms behind 4D-transformation are found in literature. The mechanism must always be activated by a stimulus. Table 2.1 gives an overview of stimulus and mechanism combinations that are found in literature publications, of which the first four are found to be the most popular. Printed structures that transform due to glass transition or thermal expansion are often made out of polymers, while structures that have absorption or osmotic pressure as a mechanism usually consist of hydrogels.

Table 2.1: Stimuli and mechanisms found in literature

Stimulus	Mechanism	Literature example
Heat	Glass transition	Kwok et al. (2015); Bodaghi et al. (2016); Maute et al. (2015); Ge et al. (2016); Geiss et al. (2019)
Heat	Thermal expansion	Geiss and Maute (2018); Hamel et al. (2019)
Water	Absorption	Sydney Gladman et al. (2016); Tibbits (2014)
Electricity	Osmotic pressure	Zolfagharian et al. (2019)
Solvent	Chemical reaction	Ionov (2011)
Magnetic field	Magnetostriction	Sossou et al. (2019)
pH	pH-sensitivity	Ionov (2011)

Hydrogels are commonly used as a 4D-printing material. They consist of hydrophilic networks of polymer chains, which swell due to water absorption (Ahmed, 2015). This absorption can be enhanced by applying electricity, which increases the difference in the number of moving ions. As a result, the difference in osmotic pressure increases and thus the water absorption is stimulated (Zolfagharian et al., 2019). Although widely used, there are a few downsides to using hydrogels for creating 4D-printed structures. Firstly, a hydrogel structure is not very stiff, which makes it suitable for a limited number of applications. Secondly, the response of the osmotic pressure mechanism to the stimulus is slow compared to other mechanisms. And finally, the final transformed state of the structure is not stable: once the stimulus is removed, the structure will return to its initial state (Ding et al., 2017). In hydrogel 4D-printing, the working principle relies on anisotropy in the material. Usually, anisotropy in 3D-printing is seen as a disadvantage, because it can cause unwanted irregularities in material properties in certain directions (Liu et al., 2018). However, in 4D-printing it can be used as an advantage. For example in the study by Sydney Gladman et al. (2016), where a hydrogel material with cellulose fibrils is used. By aligning the fibrils in a certain way during printing, the hydrogel swells anisotropically. Another example of hydrogel 4D-printing is the study by Zolfagharian et al. (2019), where swelling is enhanced further by applying electricity to create a soft hydrogel actuator.

According to Shin et al. (2017), most literature examples use amorphous polymers as a printing material (Kwok et al., 2015; Maute et al., 2015; Bodaghi et al., 2016; Ge et al., 2016; Geiss et al., 2019; Bodaghi et al., 2020). One advantage of using polymers is that they are already commonly used in 3D-printing (Ngo et al., 2018). Secondly, amorphous polymers are non-crystalline materials and thus have a glass transition temperature which can be used as a transformation mechanism, activated by heat as seen in Table 2.1. Once an amorphous polymer is heated above its glass transition temperature  $T_g$ , the material experiences a transition from a stiff, solid state to a more flexible, rubbery state. In other words, the Young’s modulus of the material decreases strongly with temperature (Shrivastava, 2018). Since this research is focused on structural applications of 4D-printing, amorphous polymers are a good choice to use as a printing material. These polymers are very well suited for creating relatively stiff, fast and stable 4D-printing structures.

#### 2.1.4 Reversibility of 4D-transformation processes

In many cases, the structure remains in the transformed configuration after 4D-transformation. This is referred to as one-way 4D-printing: the structure cannot return to its initial configuration, unless it is reprogrammed. However, for some applications it is desired to have a reversible transformation. This is referred to as two-way 4D-printing. One-way and two-way shape memory effects are illustrated in Figure 2.6. Usually, the transformed state is unstable for two-way 4D-printed objects: the structure returns to its original state when the stimulus is removed. For those applications which need a two-way transformation, but also need the transformed configuration to be stable (i.e. the structure remains in the transformed state after the stimulus is removed), the reprogramming of the prestrain can be integrated in the transformation process. This can be achieved when using two different stimuli. An example is combining a polymer structure with a hydrogel. The polymer is stimulated by heat, while the hydrogel is activated by water. Swelling of the hydrogel programs the prestress into the polymer structure. This allows the structure to switch between two stable configurations. A downside to this method is that every transformation requires five steps: soaking, heating, cooling, drying and heating again (Lee et al., 2017).

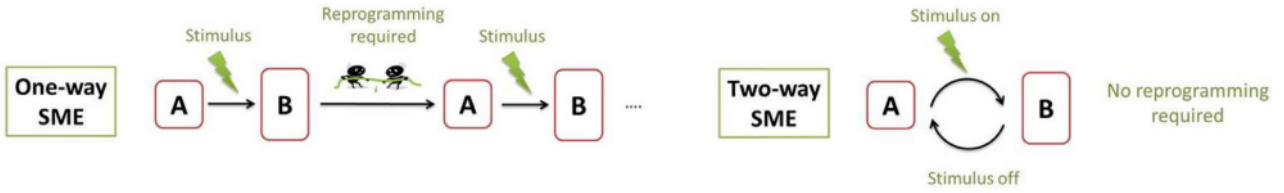


Figure 2.6: One-way and two-way shape memory materials (Hager et al., 2015)

### 2.1.5 Bi-material 4D-printing with amorphous polymers

Many types of 4D-printing exist with many stimulus-mechanism combinations. As explained earlier, using the glass transition mechanism of amorphous polymers is a popular choice in structural applications. This specific type of 4D-printing will be discussed here. Single amorphous polymer 4D-printing methods exist (see Appendix A.1), however they exhibit many uncertainties. When using two different materials, a bending deformation can be achieved as shown in Figure 2.7. Bi-material 4D-printed polymer structures comprise an active and a passive material. In most cases, one of the materials is pre-strained. The pre-strain is applied in a rubbery polymer, which is printed on top of a glassy polymer, to create a bi-layered structure. The pre-strain can be applied either indirectly (after printing) or directly (during printing). When the glassy polymer is heated above its glass transition temperature, it allows for the rubbery polymer to release the pre-strain. This causes the structure to bend from its initial configuration directly after printing (a) towards the transformed configuration (b). Most literature sources refer to the pre-strained material as the active material, since this material initiates the transformation. However, the reader should keep in mind that some other literature sources refer to the pre-strained material as passive, since it does not undergo glass transition. The concept of using two polymers can be expanded by using multiple glassy polymers with different glass transition temperatures. A multi-stage 4D-transformation can be achieved, which allows for more complicated 4D-printed structures and deployment sequences.

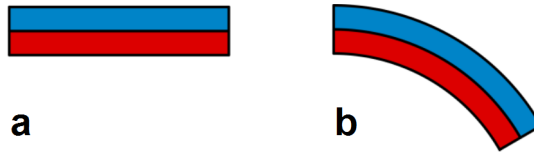
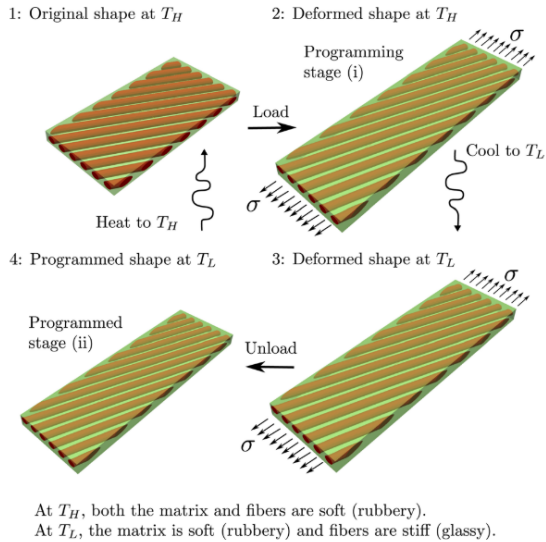


Figure 2.7: Active pre-strained layer (blue) and passive glassy layer (red), in the initial configuration (a) and the transformed configuration (b)

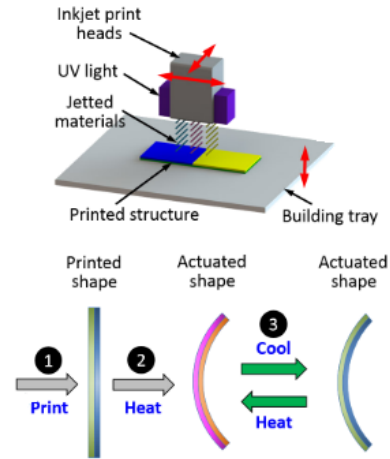
### 2.1.6 Applying the pre-strain

Methods of applying the pre-strain in the active layer of the multi-material structure can be divided into two different types: the indirect and the direct 4D-printing method. In the **indirect 4D-printing method**, the pre-stresses are applied by programming after printing. It could be argued that this makes the printed structure nothing more than an ordinary one-way multi-material shape memory polymer. An example of a programming scheme is given in Figure 2.8a. In the programming stage (i), the original structure is heated to a temperature above the glass transition temperature of the glassy polymer. Both polymers are now in a rubbery state. A load is applied to achieve a prescribed deformation. Then, the structure is cooled below the glass transition temperature, while maintaining the deformed shape. The glassy polymer stiffens and thus after unloading, the structure will only slightly deform compared to the previous step. A prestrain has now been applied in the rubbery polymer in the programmed stage (ii) (Maute et al., 2015). The structure is ready to undergo its 4D-transformation by heating it again (not shown in figure).

In **direct 4D-printing**, no programming is required. Instead, the prestrain is directly applied in the structure during printing. This method of 4D-printing requires a good understanding of how prestrains can be applied during the printing process. A method to apply prestrains is to use photopolymerization by UV-light, which is illustrated in step 1 of Figure 2.8b (Ding et al., 2017). The advantage is that the programming stage can be fully omitted: the structure is ready for its 4D-transformation directly after printing. Heating (step 2) stimulates the transformation. This is a one-way shape memory effect, so further heating and cooling (step 3) have no significant effect on the structure.



(a) Indirect 4D-printing (Maute et al., 2015)



(b) Direct 4D-printing (Ding et al., 2017)

## 2.2 Overview of applications and demonstration devices of 4D-printing

4D-printing can be used in **biomimetics**, such as mimicking complex flower geometries (Sydney Gladman et al., 2016). Figure 2.9 shows an orchid which is 4D-printed using a composite hydrogel material, containing anisotropic fibrils. Once the originally flat structure is placed in a water bath, the geometry transforms due to anisotropic swelling of the hydrogel. This demonstration shows how complex the geometry of a transformed 4D-printed structure can be.

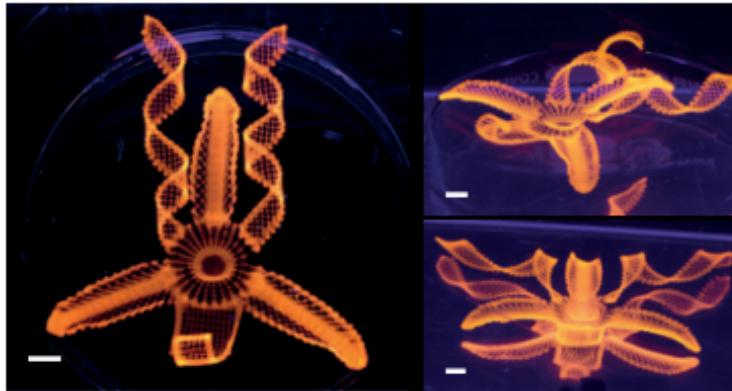


Figure 2.9: 4D-printed *Dendrobium Helix* orchid. The scale bar indicates 5 mm (Sydney Gladman et al., 2016).

Another application of 4D-printing is a **gripper**, as designed by Ge et al. (2016). Figure 2.10 shows a time lapse of a multi-material gripper grabbing an object. It is made out of multiple polymers. The polymer at the tips of the gripper (pink) has a high stiffness to be able to safely grab an object. The joints (orange) are made out of multiple polymers. An indirect 4D-printing method is used: the gripper is originally printed in a closed configuration and after programming, it is in an opened configuration. During programming, a prestress is introduced in one of the polymers. The gripper transforms towards the originally printed shape when heated above the glass transition temperature  $T_g$  of one of the other polymers. This is an example of a one-way 4D-transformation. To reuse the gripper, it has to be reprogrammed. A similar concept is used to create a **release system**, which can potentially be used for the delivery of drugs inside the human body. The structure should now be printed in the open configuration and be programmed into the closed configuration. By heating the structure, an object or substance can be released.

Bodaghi et al. (2016) created a 4D-printed meta-material lattice which could potentially be used as a **cardio-vascular stent**. However, there are also important stiffness and fatigue requirements for stents, and it is not clear whether these can be reached by this design concept. The tubular lattice is composed of multiple identical

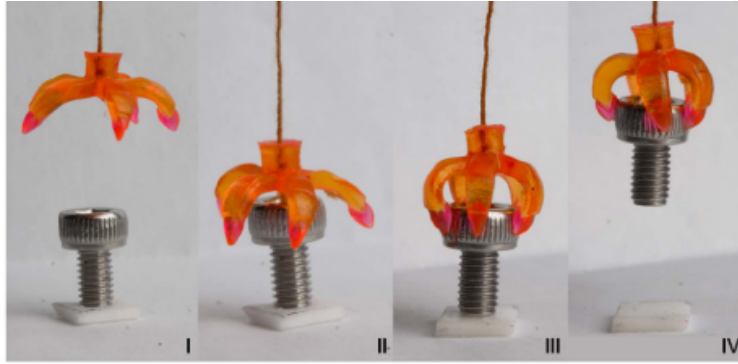
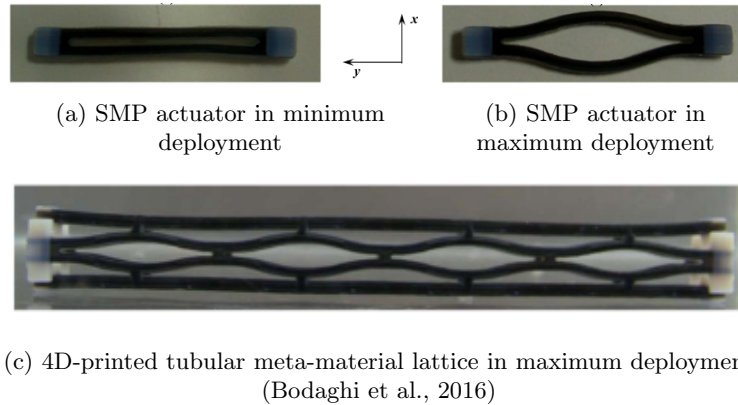


Figure 2.10: Multi-material 4D-printed gripper grabbing an object (Ge et al., 2016)

actuators, which consist of three different types of printed polymers. The total width in  $x$ -direction of each actuator will increase when the structure is heated above  $T_g$ , which is shown in Figures 2.11a and 2.11b. This causes the diameter of the entire lattice to expand. Figure 2.11c shows the lattice in an expanded state. The structure can be placed inside a catheter in its original, minimal diameter state. Once it is in the desired place, it can be expanded. Ideally,  $T_g$  should be between room temperature and human body temperature, such that the transformation is activated when the structure is placed inside the body.



(c) 4D-printed tubular meta-material lattice in maximum deployment (Bodaghi et al., 2016)

Figure 2.11

Another gripping application is the **smart hook** by Wu et al. (2016). This hook can be used to both lift and release a small container, as can be seen in Figure 2.13. It consists of two printed arms, each having two different glassy polymer fibers and a polymer matrix. This allows for a multi-stage 4D-transformation. The material configuration in one of the arms is shown in Figure 2.12. The glass transition temperature  $T_g$  of the low  $T_g$  polymer fiber ranges from  $\sim 20$  to  $\sim 55$  °C. The high  $T_g$  polymer fiber has a  $T_g$  of  $\sim 57$  °C and the matrix polymer has a  $T_g$  of 2 °C. Before deploying, both arms of the hook are heated above the glass transition temperature of both of the polymer fibers (70°C). The arms are straightened by an external load. The structure is then cooled to 0 °C while holding the straight shape. All polymers are now below their  $T_g$ , which means the straight shape will hold once the structure is released from the load. The structure is now programmed. Putting the hook in a water bath of 30 °C causes the hook to bend, because the low  $T_g$  polymer is heated above its  $T_g$ . When putting it in a water bath of 70 °C afterwards, the pre-stresses in both polymer fibers are released causing the arm to straighten again.

## 2.3 Topology Optimization in 4D-Printing

### 2.3.1 Topology Optimization

In order to exploit the possibilities of 4D-printing, it is key to have a systematic design approach. Topology optimization is a numerical design approach that finds the optimal lay-out of a structure within a specified domain, as visualized in Figure 2.14 (Bendsoe and Sigmund, 2003). The optimization problem consists of an objective function that should either be maximized or minimized and which is possibly subjected to constraints. The method of topology optimization has already been used in a few recent 4D-printing and 4D-printing related

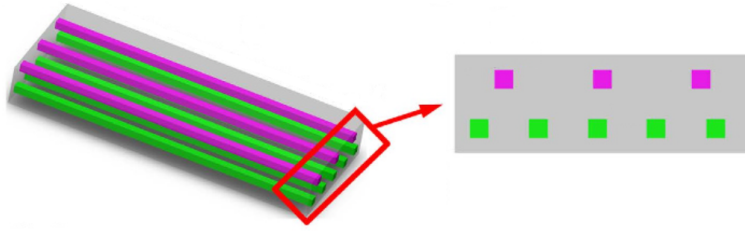


Figure 2.12: Configuration of the three materials: high  $T_g$  polymer (magenta), low  $T_g$  polymer (green) and polymer matrix (grey)

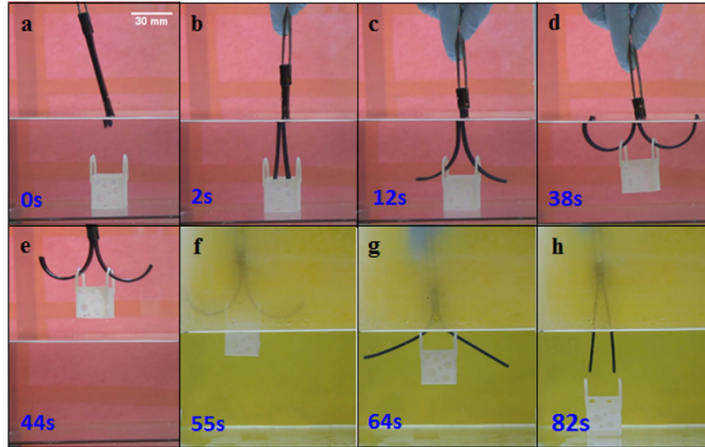


Figure 2.13: 4D-printed smart hook: (a-e) Bending deformation in a water bath of 30°C (f-h) Releasing deformation in a water bath of 70°C (Wu et al., 2016)

studies. Three types of methods are frequently used in combination with 4D-printing: level-set methods, genetic algorithm-based (GA) methods and density-based methods. Although GA-based methods have been used in studies by Hamel et al. (2019) and Sossou et al. (2019), they are relatively computationally expensive (see also Appendix A.2). Therefore, only level-set and density-based methods will be reviewed in this chapter.

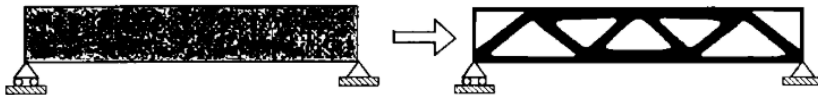


Figure 2.14: Topology optimization (left: initial problem, right: optimal solution) (Bendsoe and Sigmund, 2003)

### 2.3.2 Level-Set methods

Level-set methods define the interface of different materials with isocontours of a level-set function  $\varphi$  (Van Dijk et al., 2013). This level-set function is updated in each optimization step. The simplest case of a level-set method involves a material and a void space. The entire domain is defined as  $D$ . Within that domain, a material domain is defined as  $\Omega$ . The interface between material and void is  $\Gamma$ :

$$\begin{aligned}
 \varphi(\mathbf{X}) > c &\Leftrightarrow \mathbf{X} \in \Omega && \text{(material),} \\
 \varphi(\mathbf{X}) = c &\Leftrightarrow \mathbf{X} \in \Gamma && \text{(interface),} \\
 \varphi(\mathbf{X}) < c &\Leftrightarrow \mathbf{X} \in D \setminus (\Omega \cup \Gamma) && \text{(void),}
 \end{aligned} \tag{2.1}$$

where  $c$  is a constant and  $\mathbf{X}$  is a point in the design domain  $D$ . Figure 2.15 (a) gives a visual representation, where the material domain  $\Omega$  is indicated in blue and the void domain  $D \setminus (\Omega \cup \Gamma)$  is indicated in grey. 4D-printing is often done with more than one material. Therefore it is useful to look at a multi-material adaptation of the description of the

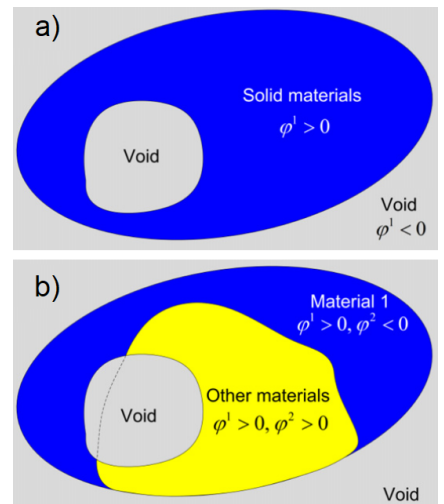


Figure 2.15: Multi-material level-set method, a) Single material, b) Multimaterial (Wang et al., 2015)

domains in Equation 2.1. The research by Wang et al. (2015) uses the following domains for multi-material topology optimization:

$$\begin{aligned}\phi_i(\mathbf{X}) > c &\Leftrightarrow \mathbf{X} \in \Omega_i \setminus \Gamma_i && \text{(material),} \\ \phi_i(\mathbf{X}) = c &\Leftrightarrow \mathbf{X} \in \Gamma_i && \text{(interface),} \\ \phi_i(\mathbf{X}) < c &\Leftrightarrow \mathbf{X} \in D_i \setminus (\Omega_i \cup \Gamma_i) && \text{(void),}\end{aligned}\tag{2.2}$$

where  $i = 1, \dots, m$  and  $m$  is the number of materials. A downside of the level-set method with multiple materials is that the result is strongly dependent on the initial design, because the emergence of new material volume inclusions within another material volume is not promoted. In the study by Maute et al. (2015), which uses a bi-material level-set method for printing active structures, this problem is solved by using an initial design with a high density of inclusions. This method might also work for more than two materials and a void.

### 2.3.3 Density-based methods

Density-based methods are widely used for topology optimization. They use a density field to describe the material distribution in the domain, and a penalization to steer the density towards 0 (void) or 1 (solid material). Intermediate density values are unwanted and can be difficult to realize in practice. These intermediate values are often referred to as grey areas. The relation between the penalized Young's modulus  $E(\theta_p)$  and penalized material volume factor of the material  $\theta_p$ , for problems with one material and one void, is given by the law (Sigmund and Maute, 2013):

$$E(\theta_p) = E_0\theta_p,\tag{2.3}$$

where  $E_0$  is the Young's modulus of the material. The definition of  $\theta_p$  depends on whether the Simplified Isotropic Material with Penalization (SIMP) density method or the Rational Approximation of Material Properties (RAMP) density method is used. In the SIMP method, which was introduced by Bendsøe (1989), the penalized material volume is given by:

$$\theta_p = \theta_{min} + (1 - \theta_{min})\theta^p,\tag{2.4}$$

where  $p \geq 1$  the penalization factor, which makes intermediate density values provide less stiffness compared to what they cost in weight. Increasing  $p$  leads to a decrease of grey area in the topology. Usually, the penalization factor is chosen as  $p = 3$ . A visualization of the effect of  $p$  can be found in Figure 2.16. The  $\theta_{min}$  term (where  $\theta_{min} > 0$ ) is introduced to make sure the penalized Young's modulus  $E(\theta_p)$  is never equal to zero. This is done for numerical reasons. In the RAMP method, which was introduced by Stolpe and Svanberg (2001), the penalized material volume is:

$$\theta_p = \theta_{min} + \frac{\theta(1 - \theta_{min})}{1 + q(1 - \theta)},\tag{2.5}$$

where  $q > 0$  is a penalization parameter with an effect that is analogous to that of  $p$  in the SIMP method. In the field of topology optimization in 4D-printing, no cases of RAMP topology optimization were found. However, the SIMP topology optimization method is used for 4D-printing by Fuchi et al. (2015) to design folding liquid crystal elastomers and by Zolfagharian et al. (2019) to design a soft hydrogel actuator. It has also been combined with the level-set method in the research by Geiss and Maute (2018) and Geiss et al. (2019).

### 2.3.4 Filtering and projection

If there is no constraint on the design freedom, the optimization result could become very complex, with features so small they cannot be resolved by the mesh. Therefore, a constraint should be imposed on the feature size. An implicit constraint on the minimum length scale can be imposed using a Helmholtz filter (Lazarov and Sigmund, 2011):

$$\theta_f = R_{min}^2 \nabla^2 \theta_f + \theta_c,\tag{2.6}$$

where  $\theta_f$  is the filtered material volume factor,  $R_{min}$  is the minimum length scale, and  $\theta_c$  is a domain control variable, where  $0 \leq \theta_c \leq 1$ . Usually,  $R_{min}$  is set to the mesh edge size  $h$ . It is recommended to change  $R_{min}$

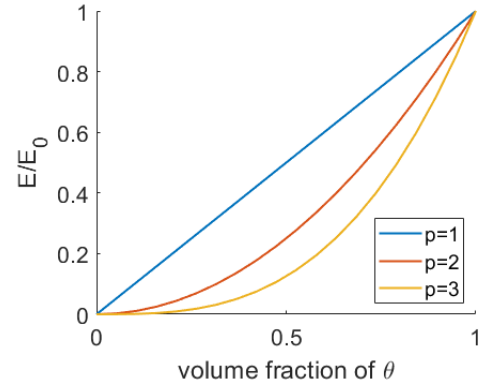


Figure 2.16: The effect of penalization factor  $p$  in Equation 2.4

to a fixed value, to get mesh-independent results (COMSOL, 2018). The effect of the filter is illustrated in Figure 2.17, where Figure 2.17a shows the material volume factor without a filter  $\theta_c$  and Figure 2.17b shows the filtered material volume factor  $\theta_f$ .

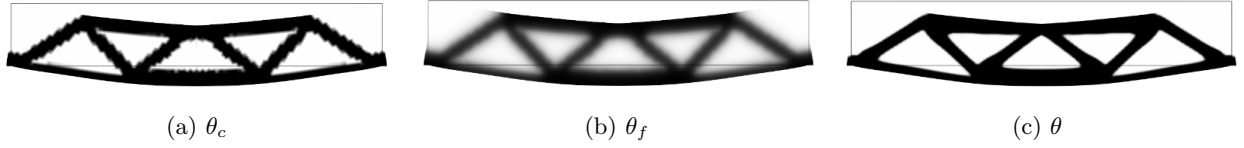


Figure 2.17: The effect of a filter and projection

Essentially, the filter blurs out the result, introducing more grey. To reduce the grey region, a smooth Heaviside projection is used (Wang et al., 2011):

$$\theta = \frac{\tanh \beta(\theta_f - \theta_\beta) + \tanh \beta\theta_\beta}{\tanh \beta(1 - \theta_\beta) + \tanh \beta\theta_\beta}, \quad (2.7)$$

where  $\beta$  is the projection slope and  $\theta_\beta$  is the projection point. The effect of both of these parameters can be observed in Figures 2.18a and 2.18b respectively. The effect of the projection can be observed in Figure 2.17c. The resulting topology is a well-defined black and white design. The use of a projection can decrease grey area, but it also slows the convergence of the optimizer down.

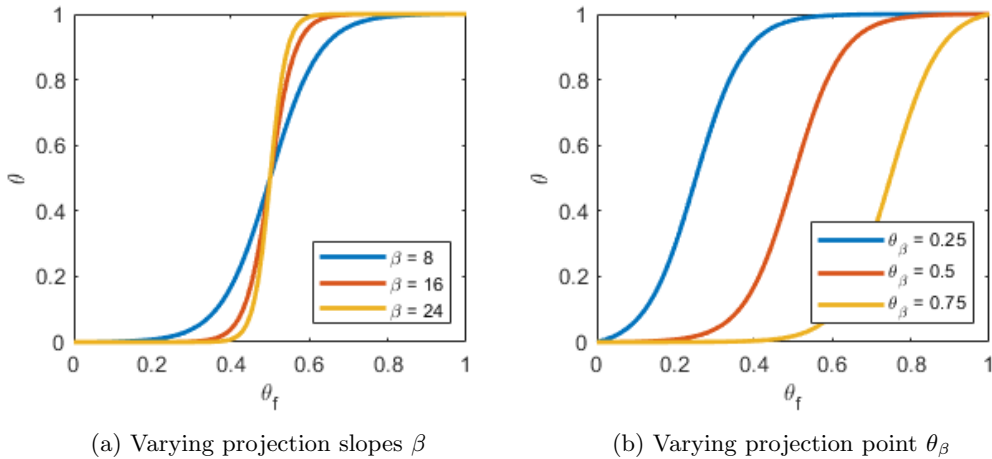


Figure 2.18: Plot of the material volume factor  $\theta$  after projection vs. the filtered material volume factor  $\theta_f$

### 2.3.5 Objective function

In 4D-printing, the geometry of the transformed structure is usually known. The initial geometry or material layout to achieve this transformed geometry is what remains to be found by the use of topology optimization. A suitable objective function should be formulated to do so. In literature, the target shape is approached by matching a desired displacement to the actual displacement. This is sometimes referred to as displacement matching (Geiss et al., 2019). The goal of the optimization is to minimize the difference between nodal displacement and target displacement. In the works of Maute et al. (2015) and Geiss et al. (2019), this has led to the following contribution to the objective function:

$$F_{target} = \int_{\Gamma_{target}} (u_i - u_{target,i})^2 dA, \quad (2.8)$$

where  $\Gamma_{target}$  is the target set,  $u$  is the nodal displacement and  $u_{target}$  is the target displacement. The studies of Hamel et al. (2019) and Sossou et al. (2019), which both use GA for optimization, use a fitness function very similar to Equation 2.8:

$$F_{target} = \frac{1}{N} \sum_{i=1}^N \sqrt{(u_i - u_{target,i})^2} \quad (2.9)$$

where  $N$  is the number of nodes. The study of Fuchi et al. (2015), which uses the SIMP method for optimization, uses the following objective function:

$$F_{target} = \frac{1}{N}(\mathbf{u} - \mathbf{u}_{target})^T \mathbf{W}(\mathbf{u} - \mathbf{u}_{target}), \quad (2.10)$$

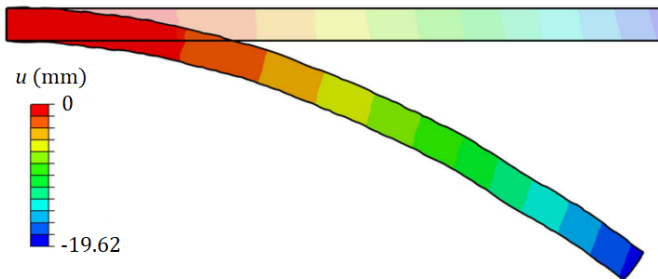
where  $\mathbf{W}$  is a matrix containing the degrees of freedom that are included in the optimization process.

## 2.4 State-of-the-Art in topology optimization for 4D-printing

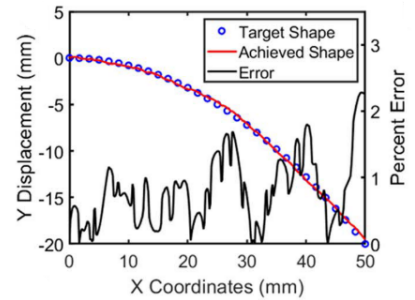
In this section, some examples from research field of topology optimization in 4D-printing are shown. Different stimuli, mechanisms and topology optimization methods will be discussed. Most examples consist of numerical simulations only, however some also show experimental data. These experiments merely show a qualitative comparison between the numerically determined design and the activated printed structure. Not many quantitative results were yet found in literature.

### 2.4.1 Parabolic target shape simulation

In the research by Hamel et al. (2019), a topology optimization is performed on the domain area of a beam to achieve a parabolic target shape as seen in Figure 2.19a. A genetic algorithm is used to match the displacement to a parabola shape. The optimizer is able to choose between two different materials. One of these materials is referred to as the active material, by which is meant that this material will respond to a certain stimulus. The stimulus here is heat, however the mechanism behind the transforming behaviour of the active material is not stated in the paper. The reader should notice that this nomenclature of active and passive is different from what was explained in Section 2.1.5: ‘Multi-material 4D-printing’, where the material responding to the stimulus is referred to as passive. Figure 2.19b shows that the optimizer was able to find a topology that approaches the target deformation very well.



(a) Parabolic deformation of the optimized beam



(b) Topology optimization performance

Figure 2.19: Results of the parabolic bending simulation

### 2.4.2 Adaptive wing simulation

A similar approach as described in the previous section is used in the paper by Sossou et al. (2019). Here, a genetic algorithm-based topology optimization is used to design an active shape-changing wing. The wing should be able to deform into a twisted formation, to optimize the lift on the plane. No voids can be introduced by the optimization and three different materials are used: a silicone (blue) and two magnetostrictive materials (red and orange). Magnetostrictive materials expand or shrink when exposed to a magnetic field, depending on the nature of the magnetic field. In a multi-layer orientation, this material property can be exploited to achieve bending. The silicon functions merely as a matrix and does not respond to the magnetic field. A multi-material genetic algorithm method is used to find the optimal topology for a displacement matching objective function. This objective function is formulated such that the target twisting angle of the wing is  $15^\circ$ . An image of the wing in maximum deformation can be found in Figure 2.20. The twisting angle that is achieved in this simulation is  $12^\circ$ , which is less than the desired twisting angle. In the paper, it is suggested that the performance of the optimization can be improved by for example optimizing the magnetic field or allowing voids in the design domain.

### 2.4.3 Active propeller simulation

The study of Geiss and Maute (2018) shows the optimized design of a 4D-printed active propeller. The topology optimization method is a combination of the level-set and the SIMP method. The optimization is done with

a void phase and two material phases: an active and a passive material. The active material expands when heated, causing the structure to deform. The objective of the topology optimization is to match the twisting of the tips of the propeller arms to a desired amount. A visualisation of the optimized propeller topology is shown in Figure 2.21. A braided pattern of active material (blue) can be identified on the passive material (red). This pattern causes the twisting deformation. The target twisting angle of  $45^\circ$  could not be fully achieved, however it was quite close. A side note from the authors is that the twisting angle is probably overestimated in the simulation, since a linear elastic material model is used. They recommend a nonlinear elastic material model to obtain more realistic simulations.

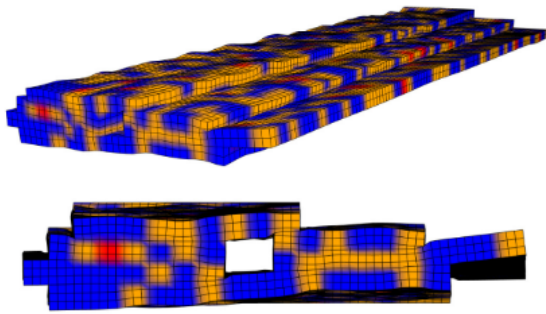


Figure 2.20: Topology optimized design of an adaptive wing (Sossou et al., 2019)

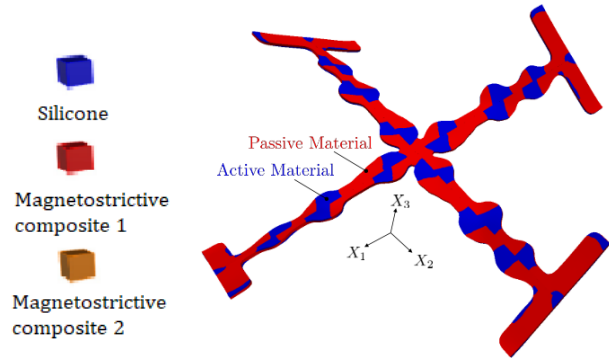


Figure 2.21: Topology optimized design of an active propeller (Geiss and Maute, 2018)

#### 2.4.4 Self-folding origami simulation and experiment

Topology optimization is applied to self-folding applications in the paper by Fuchi et al. (2015). Although the structure is not created using additive manufacturing, there are still similarities with our topic of research. The folding deformation is induced by hinges made of an active material that bends when heated. The mechanism behind this bending behaviour is not stated in the paper. A SIMP topology optimization is used to find the optimal placement of the active material, to achieve the sharpest folding edge possible. The objective function is formulated as such that the shape is matched with that of a perfect hinge. This way, an optimized hinge is created, as can be seen in Figure 2.22. The design of this hinge was adapted to create a multi-hinge self-folding origami box as shown in Figure 2.23. At a temperature of  $100^\circ\text{C}$  the box is fully closed, in a shape very close to the target shape. However, the structure is multi-stable and easily deformed into another mode shape different from a closed box. Since the energy levels of the mode shapes lie close to each other, small errors in fabricating or applying of the stimulus could cause the structure to transform into the wrong mode shape. In the paper, it is suggested to incorporate the multi-stability effects in the model, to improve the simulation.

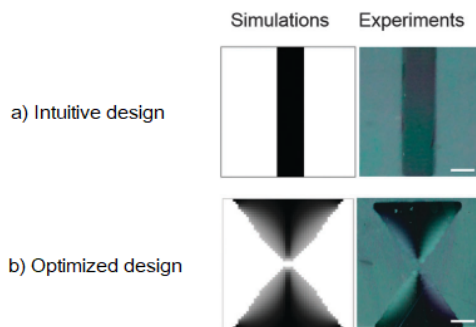


Figure 2.22: Designs of a folding hinge (a) intuitive design, (b) topology optimized design (Fuchi et al., 2015)

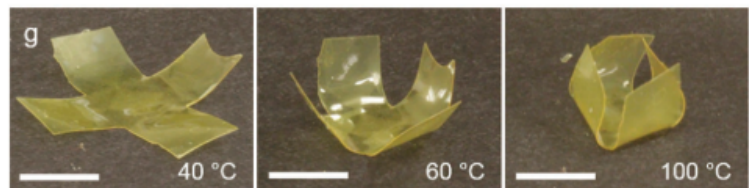


Figure 2.23: Experimental results of a topology optimized self-folding origami box (Fuchi et al., 2015)

#### 2.4.5 Soft actuator experiment

In the research by Zolfagharian et al. (2019), a SIMP topology optimization method is used to find the optimal topology of a soft hydrogel actuator. The transformation is activated by an electrical stimulus, which increases the osmotic pressure in the hydrogel. This causes the hydrogel to swell. Figure 2.24a compares a uniform lattice structure (I) to the topology optimized actuator (II). Figure 2.24b shows the test setup that was used

for experiments with the optimized actuator. Here, the deflection with respect to a reference (red dotted line) is shown (blue dotted line). Although no numerical results are given in the paper, it is clear that the optimized actuator outperforms the uniform lattice actuator.

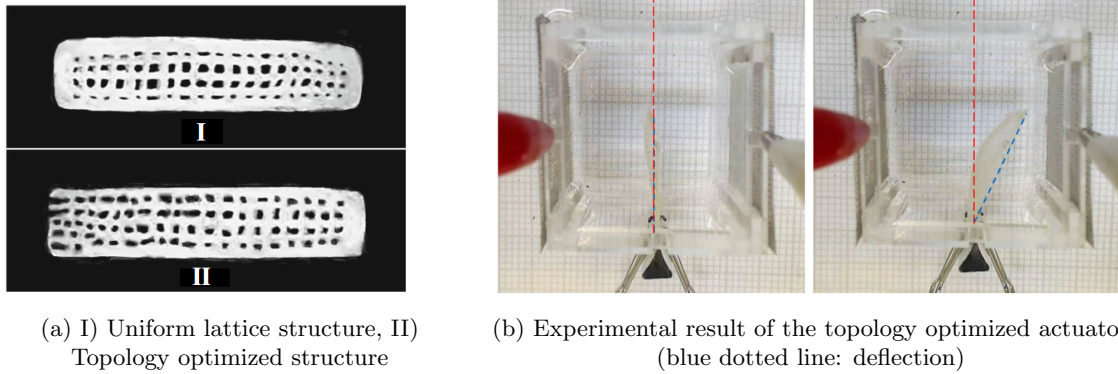


Figure 2.24: Soft hydrogel actuator (Zolfagharian et al., 2019)

### 2.4.6 Shape shifting lattice

Multi-material 4D-printing is used to create shape shifting lattices in the study by Boley et al. (2019). All four materials used in the printing process consist of an elastomer matrix, which is filled with different amounts of glass fibers and silica to tune the material properties. The main working principle of this shape shifting is the difference in thermal expansion between the materials, which leads to a bending transformation when heated. Besides that, the material swells when immersed into a solvent. This property is exploited to achieve multiple stable configurations. The printed lattice consists of ribs connecting a grid of nodes, of which the cross section exhibits four material domains to control both in-plane and out-of-plane curvature. Figure 2.25 shows that various degrees of in-plane curvature can be achieved by configuring the materials in the four domains. Another design variable is the initial curvature of the ribs. The material distribution and the initial curvature are chosen to match a target shape. Target shapes of a hemispherical patch antenna and a face are used to demonstrate the performance of the printed lattice.

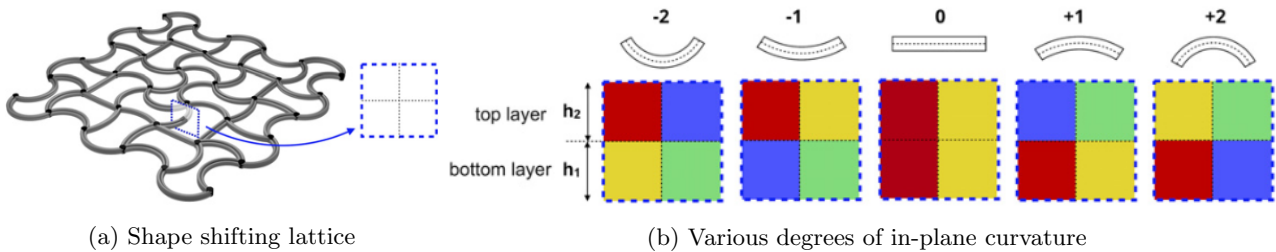


Figure 2.25: Material configurations in a 4D-printed shape shifting lattice

### 2.4.7 Composite beam experiment

The study of Maute et al. (2015) shows several experiments using a simple composite beam. Experiments with different target displacements were done, such as parabolic bending. They can be found in Table 2.2, along with their target displacement functions. Figure 2.26 shows the result of level-set topology optimization for a parabolic shape. The gray area shows the layout of the active material, which is a printed active composite, while the passive material is transparent. Both designs are printed and tested. The maximum measured deflection is approximately 18% larger than in the numerically determined deflection, which is a rather large difference. The results of other target shapes have an even larger difference. This difference can be attributed to errors in the model and errors in the experimental method, of which the latter will not be discussed here because the paper does not provide details. The model that is used assumes infinitesimal strains and a linear material behaviour. It is expected that, in order to get more accurate results, a model should be used that accounts for large strains and large displacements.

### 2.4.8 Complex composite structure experiments

In the study by Geiss et al. (2019), several experiments with composite designs of a higher level of complexity are shown. Here, the difference with the numerically determined design, which is generated using the level-set

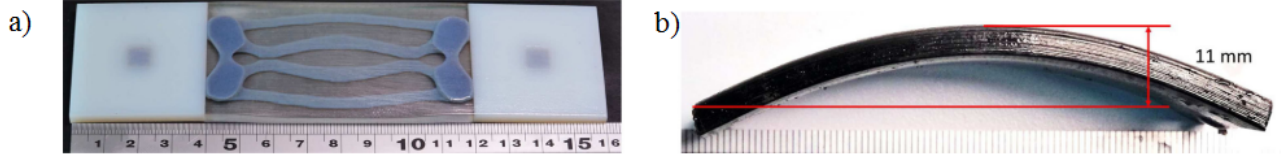


Figure 2.26: a) Printed composite beam structure before transformation b) Printed composite beam structure after transformation Maute et al. (2015)

Table 2.2: Composite beam experiments with results

Target shape	Target displacement function*	Difference with theoretical design**
Parabolic bending	$u_{target} = -A\left(\frac{2x_1}{L}\right)^2$	18%
Cosine wave	$u_{target} = -A\left(1 - \cos \frac{\pi x_1}{L}\right)$	75%
Twisted parabolic bending	$u_{target} = -2A\left(\frac{x_1}{L}\right)^2 \sin \frac{\pi x_2}{L}$	30%

$$* 0 \leq x \leq L$$

\*\*Difference between the maximum displacement of the experiment and the theoretical design

method, is only evaluated visually. To achieve more complex shapes, target displacements are imposed on points of a target set. A hyperelastic material model is used in the simulations. The target sets and target displacements can be found in Table 2.3. One example is a twisted figure-eight, which is initially printed in the shape of a flat, symmetric cross as shown in Figure 2.27a. The symmetry is exploited, such that only a quarter of the design domain has to be analyzed. Two target points  $\mathbf{X}_1$  and  $\mathbf{X}_2$  are located on the tips of two of the arms. The target displacements  $u_{target1}$  and  $u_{target2}$  are chosen as such that the structure becomes a figure-eight after transformation. The numerically determined design (Figure 2.27b) shows a slight overlap of the arms after transformation. This is because the model does not take self-penetration into account. In the printed design (Figure 2.27c), this issue is avoided by slightly changing the  $X_3$  target. Besides that, the 4D-printed structure looks very similar to the numerically determined design. The other designs, shown in Figures 2.28, 2.29 and 2.30, show results of similar quality.

Table 2.3: Complex composite structure experiments

Target shape	Target set (mm)	Target displacement functions (mm)
Twisted figure-eight	$\mathbf{X}_1 = [80.0, 0.0, 0.0]$ $\mathbf{X}_2 = [0.0, 80.0, 0.0]$	$u_{target1} = [-80.0, 0.0, 50.0]$ $u_{target2} = [0.0, -80.0, -50.0]$
Cylindrical gripper	$\mathbf{X}_1 = [0.0 \leq X_1 \leq 30.0, 75.0 \leq X_2 \leq 80.0, -0.5]$ $\mathbf{X}_1 = [0.75 \leq X_1 \leq 80.0, 0.0 \leq X_2 \leq 30.0, -0.5]$	$u_{target1,z} = u_{target2,z} = -45.0$ Cylinder aligned with $X_3$ , $R_{target} = 50.0$
Four-legged gripper	$\mathbf{X}_1 = [0.0, 80.0, 0.0]$ $\mathbf{X}_2 = [80.0, 0.0, 0.0]$	$u_{target1} = [-80.0, 0.0, -50.0]$ $u_{target2} = [0.0, -80.0, -50.0]$
Self-elevating plane	$\mathbf{X}_1 = [105.0 \leq X_1 \leq 120.0, 0.0 \leq X_2 \leq 5.0, 0.0]$ $\mathbf{X}_2 = [0.0 \leq X_1 \leq 5.0, 105.0 \leq X_2 \leq 120.0, 0.0]$ $\mathbf{X}_3 = [0.0 \leq X_1 \leq 15.0, 0.0 \leq X_2 \leq 15.0, 0.0]$	$u_{target1,z} = 0.0$ $u_{target2,z} = 0.0$ $u_{target3} = [0.0, 0.0, 40.0]$

## 2.5 Research Scope

Now that a context on the topics of this research project is provided, a more detailed and narrowed down version of the research goal from Section 1.2: ‘*Research Goal*’ will be given. A variety of methods for both 4D-printing and topology optimization was discussed. This section will explain which of these methods will be the in scope of this research.

- The two most common 4D-printing materials are hydrogels and polymers, of which **polymers** are very well suited for structural applications, while hydrogels are less so due to their low stiffness.
- Most polymer 4D-printing studies focus on the use of **multiple materials** (Momeni et al., 2017). Even though single polymer 4D-printing is possible, it is not often mentioned in literature. Both of these methods have many uncertainties and are therefore less reliable compared to multi-material methods.

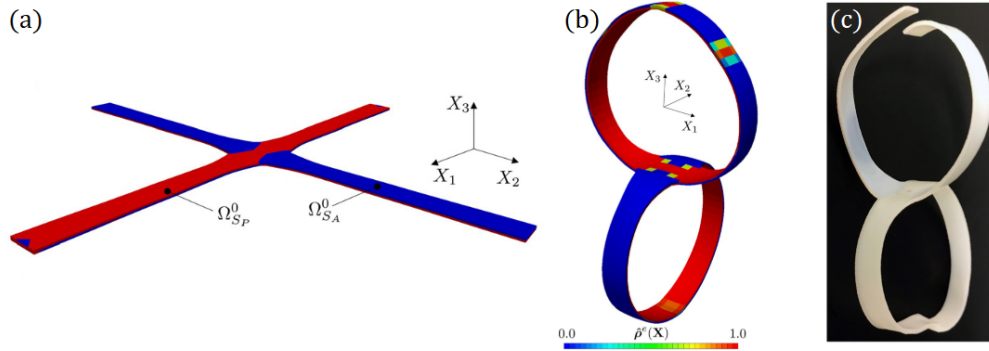


Figure 2.27: Twisted figure-eight, a) Numerical model before transformation, b) Numerical model after transformation, c) Printed structure after transformation

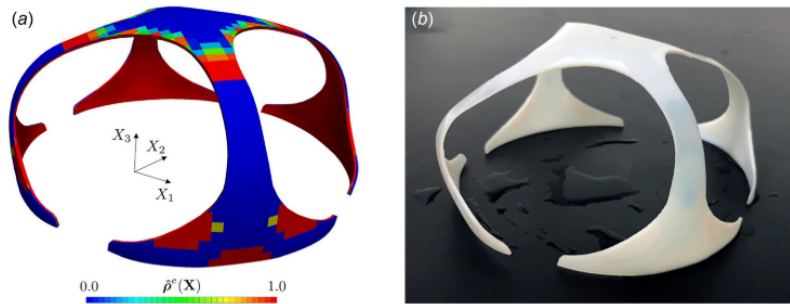


Figure 2.28: a) Numerically determined design of the cylindrical gripper b) 4D-printed cylindrical gripper after transformation

- A convenient stimulus for activating polymer 4D-structures is **heat**. Heat can easily be applied, for example by putting the structure into a hot water bath.
- **Glass transition** is chosen as a transforming mechanism, to achieve a one-way (non-reversible) 4D-transformation process as explained in Section 2.1.4: ‘*Reversibility of 4D-transformation processes*’. This means the transformed state of the structure is stable. Depending on the application, this might be an advantage. The product of this research project will potentially be suitable for self-assembling and disassembling applications.
- The numerical model that is going to be used to do the finite element analysis is going to be created using **COMSOL Multiphysics software**. As the name indicates, this software program is capable of combining multiple physics fields. This may be convenient, since both structural mechanics and heat are involved in the research problem. Furthermore, COMSOL Multiphysics has a built-in topology optimization module. And lastly, this particular software program is chosen because of the author’s familiarity with the program and the possibility to follow a course to learn to work with it.
- Density-based topology optimization methods as discussed in Section 2.3.3: ‘*Density-based methods*’ are widely used. The **SIMP method** is the simplest of the three topology optimization methods that were discussed. It can easily be adapted to a multi-material method as well. Since the goal of this research project is to create a design tool that is as simple as possible, using the SIMP topology optimization method is an appropriate choice. Another advantage is that the SIMP method is already integrated in the finite element software package that is going to be used during the project.
- Similar to what is seen literature, as described in Section 2.8: ‘*Objective function*’, an objective function that uses **displacement matching** is going to be used as a basis for the topology optimization. It might be necessary to later add other terms to the objective function.
- The study by **Geiss et al. (2019)** is close to what will be researched during this project: it also uses topology optimization in amorphous polymer 4D-printed structures that have glass transition as a mechanism. It is also the most advanced literature source in terms of numerical and experimental data results existing close to our research scope. These results will be taken as the starting point of this thesis and from there, the goal is to create even more complex 4D-printed structures.

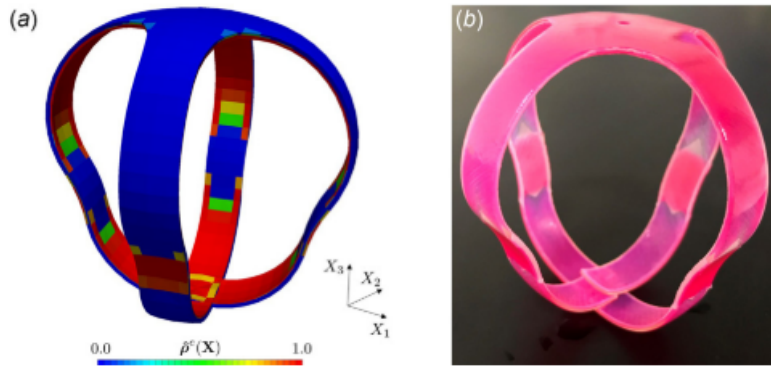


Figure 2.29: a) Numerically determined design of the four-legged gripper b) 4D-printed four-legged gripper after transformation

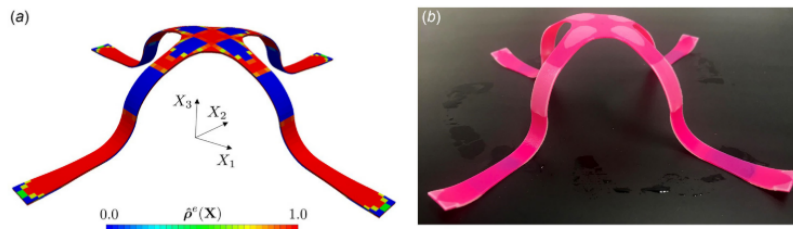


Figure 2.30: a) Numerically determined design of the self-elevating plane b) 4D-printed self-elevating plane after transformation

Summarizing, already quite some research has been done on the specific kind of 4D-printing described here. However, there is still enough challenge in this area of research. More complex structures can be investigated, such as structures with a double active layer and structures with multiple glass transitions. More complex objectives can be assigned to the topology optimization, such as the objective to achieve twisted bending. Different approaches in achieving a desired target configuration can be tried, for example to match the transformed configuration to a shape function instead of only matching a set of target points. Experiments will be performed to validate the designs and to collect numerical data. The transformation process as a function of temperature can be further examined, instead of only looking at the final results.

# Chapter 3

## Development of the 2D-Model

This section will explain the methodology of developing a 2D modeling approach that describes deformation of 4D-printed structures. The modeled structures consist of an active, prestrained polymer and a passive, glassy polymer. The Young's modulus of the glassy polymer decreases when material is heated to a temperature above the glass transition temperature  $T_g$ . Because of the decrease in stiffness, the prestress in the active layer causes a bending deformation. The model is used to analyze a given geometry that is heated step-wise from an initial temperature  $T_i$  to a final temperature  $T_f$ , causing the deformation. Throughout the report, this model will be referred to as the 'default' 2D model. In later chapters, variations of the parameters in this default model will be discussed as well.

### 3.1 Model definition

When researching topology optimization in 4D-printing, it is interesting to study many different geometries to explore the possibilities. To begin with, the simplest version of a 4D-printed structure will be considered: a bi-layered beam with an active, prestrained top layer and a passive bottom layer. The dimensions of this default geometry can be found in Table 3.1. The symmetry of the geometry can be exploited such that only half of it has to be modeled. This will speed up the computation time, because there are less degrees of freedom in the simulation. The symmetry axis is located at  $x = 0.04$  m. A visualisation of half of the domain is given in Figure 3.2. The  $x, y$ -coordinate convention in this figure will be used throughout this chapter.

Table 3.1: Dimensions of the 2D geometry

Parameter	Symbol	Value (mm)
Height of passive layer	$h_1$	0.5
Height of active layer	$h_2$	0.5
Length	$L$	80



Figure 3.1: 2D mesh (zoomed in)

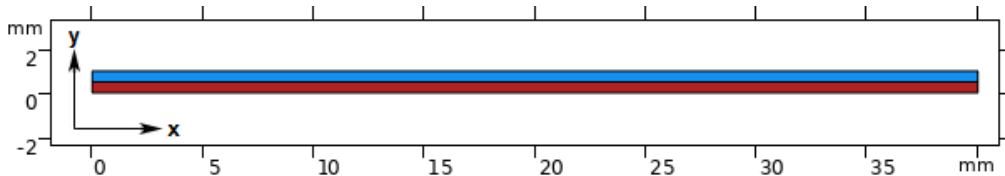


Figure 3.2: 2D geometry with active layer (blue) and passive layer (red)

The geometry that is described here is actually a 2D representation of the cross-section of a 3D structure, with a depth of  $d = 10$  mm in  $z$ -direction (perpendicular to the  $x, y$ -plane). That means an assumption needs to be made about the out-of-plane deformation of the cross-section. In a plane stress assumption, the structure can expand or shrink in the out-of-plane direction. This is a suitable assumption for slender structures that have a very small depth compared to their length. In a plane strain assumption, there is no deformation in the out-of-plane direction. This assumption is suited for structures with a larger depth, such as the geometry that is described here. Therefore, the plane strain assumption will be used. All edges of the geometry are free except for the rightmost edge, which is also the symmetry axis (indicated in green in Figure 3.2). One point

on that edge has a fixed boundary condition, which is shown in Figure 3.3a. The rest of this edge has a roller boundary that restrains movement in the  $x$ -direction, which is visualized in Figure 3.3b. A mapped mesh with quadrangular elements with quadratic shape functions will be used. The element size is equal to the layer height  $h_1 = h_2$ . An image of the mesh can be found in Figure 3.1.

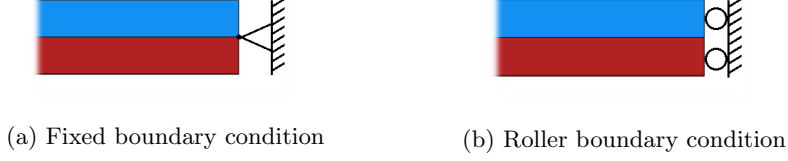


Figure 3.3: Boundary Conditions

Two different materials are going to be used during printing. Tango+ is used for the active parts of the structure and VeroClear is used for the passive parts of the structure. The relevant material properties of these materials can be found in Table 3.2. The Young’s modulus  $E$  of VeroClear is highly dependent on temperature. In the work of Akbari et al. (2018), sample tests were done to find the relation between  $E$  and  $T$ . Results of these tests can be found in Figure 3.5.

Table 3.2: Material properties of Tango+ and VeroClear

Property	Tango+	VeroClear
Young’s modulus	0.6 MPa	see Figure 3.5
Poisson’s ratio	0.4	0.4
Mass density	1.14-1.15 g/cm <sup>3</sup>	1.18-1.19 g/cm <sup>3</sup>
Glass transition temperature	-10 °C	58 °C

### 3.2 Physical modeling

The mechanism behind the deformation of the bi-layered structure can be simulated in different ways. Two different methods will be discussed here: the thermal expansion model and the glass transition model. The effect of using glass transition to achieve bending of a partly prestressed beam is very similar to the effect that is seen in thermally actuated bimorph actuators. In this type of actuator, the difference in thermal expansion of two materials is exploited to create a difference in thermal strain, causing the structure to bend. The field of bimorph actuators is well-established and the thermal expansion effect is very easy to model in the software. Since the effect of a prestress in the active material combined with glass transition in the passive material is very similar, it might be convenient to use a thermal expansion model to simulate the effect. This method was already seen in literature, for example in the papers of Hamel et al. (2019) and Geiss et al. (2019). In the paper by Geiss et al. (2019), a coefficient of thermal expansion (CTE) of 0.05 1/K is used for the Tango+ material and a CTE of 0.00 1/K is used for the VeroClear material.

Another way to simulate the deforming effect is to stay closer to what is truly happening during the transformation. In this method, the glass transition curve of the VeroClear material should be approximated. The active Tango+ layer will be given an initial strain of  $\varepsilon = 0.03$  in  $x$ -direction, just as it would have after printing (Ding et al., 2017). An advantage of using this method, is that the intermediate deformation results as a function of temperature are more accurate. Therefore, this type of simulation does not only give an insight in the final deformation of the structure: it is also able to give an insight in intermediate deformations of the transformation process.

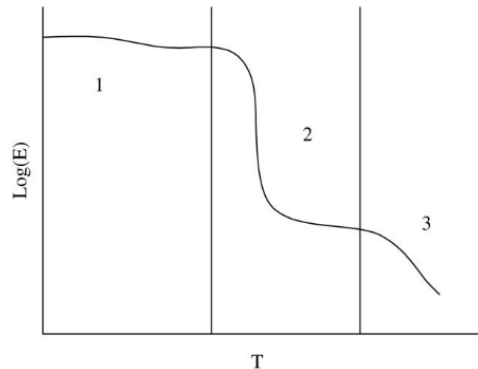


Figure 3.4: Graph of standardized  $E$ - $T$  relation (Mahieux and Reifsnider, 2001)

In a paper by Mahieux and Reifsnider (2001), a standardized equation for approximating the Young’s modulus-temperature curve of amorphous polymers is introduced. This equation is plotted in Figure 3.4. This figure

shows three types of transitions: the beta transition (region 1), glass transition (region 2) and melting transition (region 3). The beta transition and melting transition occur outside the range of temperatures that are of interest. Therefore, a simplified version of the standardized equation can be used:

$$E(T) = (E_r - E_g) \exp\left(-\left(\frac{T}{T_1}\right)^{m_1}\right) + E_g \exp\left(-\left(\frac{T}{T_2}\right)^{m_2}\right), \quad (3.1)$$

where  $E_r$  represents the Young's modulus at the beginning of the rubbery plateau and  $E_g$  is the Young's modulus at the beginning of the glassy plateau.  $T_1$  and  $T_2$  are the temperatures at the beginning of the glass transition and melting transition. Note that these temperatures are not necessarily equal to the glass transition temperature and the melting temperature, as those are usually the temperatures in the middle of the transition.  $m_i$  are the Weibull moduli, which correspond to the statistics of bond breakage. The parameters in the equation cannot be found in literature, so they have to be found by fitting the equation to data provided in the publication of Akbari et al. (2018). The fitted curve can be seen in Figure 3.5. The parameters that are used to create the fitted curve can be found in Table 4.1.

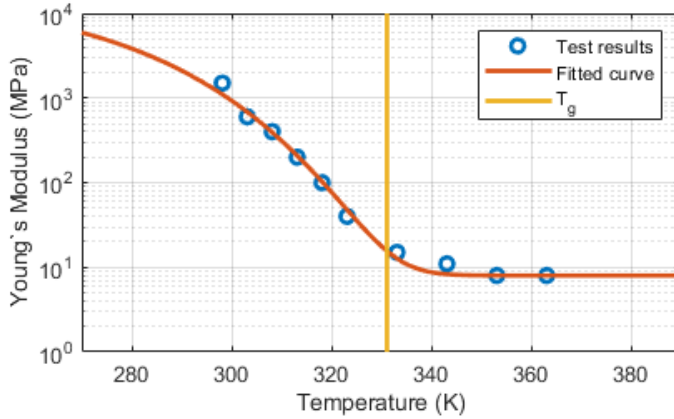


Table 3.3: Parameters used for fitting Equation 3.1 to the test result data

Parameter	Value
$E_r$	16 GPa
$E_g$	8 MPa
$T_1$	270 K
$T_2$	1000 K
$m_1$	10
$m_2$	10

Figure 3.5: Data from the paper by Akbari et al. (2018) fitted to Equation 3.1

The transformation will be activated by heating the structure from initial temperature  $T_i$  to final temperature  $T_f$ . During experiments, the samples will be heated by putting them in a water tank and increasing the temperature of the water. The goal is to realistically model this process and therefore, the possible testing temperatures in the simulation are limited between the melting and boiling temperatures of water (273 and 373 K). For convenience, the initial temperature will be equal to room temperature (293 K). In Figure 3.5, it can be observed that the Young's modulus of the VeroClear material does not change for temperatures between 353 K and 373 K. This means the sample will not deform anymore when increasing the temperature above 353 K. In the experiments, temperatures close to the boiling temperature of the water should be avoided for safety reasons. A final temperature of 353 K will be used in the experiments. However in the simulations, the temperature is easily increased slightly further without safety risks. Therefore, the final temperature in the simulations will be set to 373 K, to be able to identify possible further deformation due to side effects. The temperature will be increased with steps of 1 K in the simulations.

Since large deformations occur in the simulations, it is necessary to include geometrical nonlinearities. This means the strains in the material are represented by the Green-Lagrange strain tensor:

$$E_{ij} = \frac{1}{2} \left( \frac{\partial U_i}{\partial X_j} + \frac{\partial U_j}{\partial X_i} + \frac{\partial U_k}{\partial X_j} \frac{\partial U_k}{\partial X_i} \right) = \frac{1}{2} (\mathbf{F}^T \mathbf{F} - \mathbf{I}) \quad (3.2)$$

where  $U$  are the displacements and  $X$  are the coordinates in the material (Lagrangian) field.  $\mathbf{F}$  is the deformation gradient tensor and  $\mathbf{I}$  is the identity tensor. The stresses are represented by the Second Piola-Kirchhoff tensor:

$$\mathbf{S} = J \mathbf{F}^{-1} \boldsymbol{\sigma} \mathbf{F}^{-T}, \quad (3.3)$$

where  $J$  is the determinant of the deformation gradient tensor  $\mathbf{F}$  and  $\boldsymbol{\sigma}$  is the Cauchy stress. Figures 3.6 demonstrates the difference between simulation results without and with geometrical nonlinearities included.

Both figures show the fully transformed configuration at 373 K. Only half of the geometry is shown, because of symmetry. The figures show substantial differences. It can be concluded that the displacement is slightly overestimated when using a geometrically linear approximation. The transformed shapes are very different, because the displacement in  $x$ -direction is zero in the geometrically linear result. This becomes more problematic as the curvature increases. Therefore, geometrical nonlinearities must be included in the model at all times.

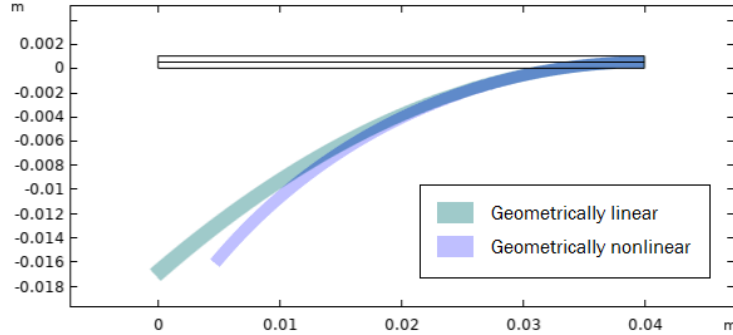
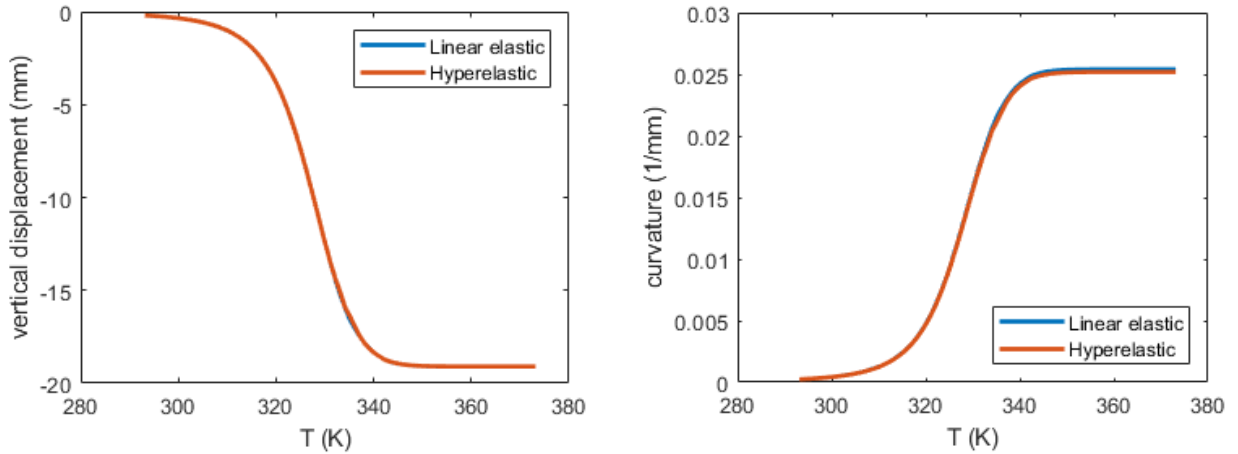


Figure 3.6: Simulated deformation without geometrical nonlinearities included

In the research by Geiss et al. (2019), a hyperelastic Saint Venant-Kirchhoff material model is used. Since this paper can be seen as the starting point of this research, it may seem logical to adopt this material model. The hyperelastic model is especially suitable for large deformations and small strains, which applies to the type of simulations that will be done in this research. However, in terms of computation time, it is more beneficial to use a linear elastic material model. If the strains in the structure are sufficiently small, it is safe to use a linear elastic material model. To find out which of the two material models should be used, a simulation should be done with both of them. However, it should be noted that in the COMSOL software, it is not possible to define an initial strain in a hyperelastic material. To still be able to compare the hyperelastic to the linear elastic material model, an external strain of 0.03 is imposed on the active layers. A comparison of displacement and curvature using both material models are shown in Figure 3.7. The linear elastic and hyperelastic data show almost no difference. Therefore, it can be concluded that it is safe to use a linear elastic material model.



(a) Vertical tip displacement-temperature plot for a linear and a hyperelastic material model (b) Curvature-temperature plot for a linear and a hyperelastic material model

Figure 3.7: Comparison of curvature and displacement of a linear elastic and a hyperelastic model

When using a linear material model, the stress tensor  $\boldsymbol{\sigma}$  is related to the elastic strain tensor  $\boldsymbol{\varepsilon}_{el}$  by Hooke's law:

$$\boldsymbol{\sigma} = \boldsymbol{\sigma}_{ad} + \boldsymbol{C} : \boldsymbol{\varepsilon}_{el}, \quad (3.4)$$

where  $\boldsymbol{\sigma}_{ad}$  represents extra added stresses, such as initial stress or visco-elastic stress.  $\boldsymbol{C}$  is the elasticity tensor, which is a fourth order tensor defined by the Young's modulus and the Poisson's ratio if the material is isotropic. The elastic strain tensor can also be expressed as  $\boldsymbol{\varepsilon}_{el} = \boldsymbol{\varepsilon} - \boldsymbol{\varepsilon}_{inel}$ . Since a geometrically nonlinear model is used, it is convenient to express Equation 3.4 in terms of the Second Piola-Kirchhoff tensor  $\boldsymbol{S}$  and the Green-Lagrange

strain tensor  $\mathbf{E}$ :

$$\mathbf{S} = \mathbf{S}_{ad} + J\mathbf{F}_{inel}^{-1}(\mathbf{C} : \mathbf{E})\mathbf{F}_{inel}^{-T}, \quad (3.5)$$

where  $\mathbf{S}_{ad}$  represents extra stresses and  $\mathbf{F}_{inel} = \mathbf{F}\mathbf{F}_{el}^{-1}$  is the inelastic deformation gradient tensor (COMSOL, 2008).

When choosing a study type, a decision has to be made whether time-dependent effects in the transformation can be neglected or not. Time-dependent effects can originate from inertial forces caused by fast changes in the loading parameter, which is temperature in our case, and visco-elasticity. It is assumed that inertial forces can be ignored, since the temperature rate can easily be controlled to be sufficiently low. If visco-elastic effects cannot be neglected, a linear visco-elastic material model should be used, meaning that the stress-strain relation becomes a function of time. When using a time-dependent study, computation times in the simulation will be very high. Especially when moving forward to 3D, this could become problematic.

In the study of Ding et al. (2017), the time-dependent effect in 4D transformation of printed samples is researched by doing experiments. Here, beam curvature data was gathered using both continuous and discrete heating. Figure 3.8 shows a curvature plot of two identical composite beam sample transformations, both obtained in different ways. For one of the samples, the water temperature is gradually increased (continuous heating). For the other sample, the water is heated in time steps of 20 seconds (discrete heating). At the end of each time step, the curvature is measured. The results of both methods are very similar, which implies that there is no need to include time-dependent effects. Therefore, a stationary study type is chosen to do the simulations.

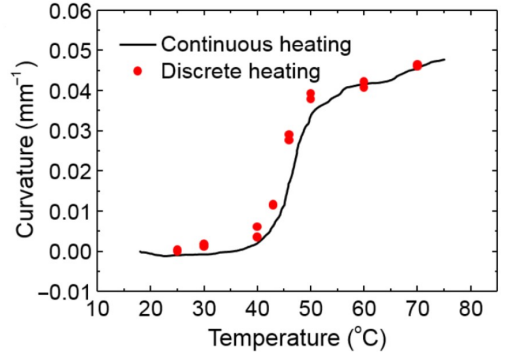


Figure 3.8: Temperature-curvature plot for continuous and discrete heating of a composite beam sample (Ding et al., 2017)

### 3.3 Convergence analysis

To check whether the mesh size is small enough to generate accurate results, a mesh size convergence analysis is done. The simulation will be repeated for different mesh sizes, while the other parameters are kept constant. In all cases, quadrangular elements are used with bilinear shape functions. The default geometry is used. Table 3.4 shows results of the mesh size convergence analysis. In the bottom row, the average relative deviations (RD) with respect to the finest mesh (0.0125 x 0.0125 mm) results are shown. Figure 3.9 shows a plot of the temperature and the vertical displacement for different mesh sizes. From these results can be concluded that having only one element per layer in y-direction gives quite a large relative deviation. Halving the mesh size already leads to a substantial improvement. It is safe to say that the mesh size of 0.05 x 0.05 mm used in the initial study is small enough, because the relative deviation is only 0.66%.

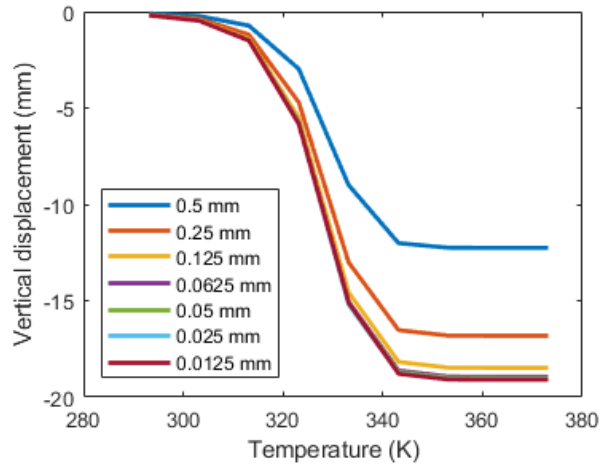


Figure 3.9: Temperature-vertical displacement plot for different element sizes

A similar analysis can be done for the element order. In this analysis, the mesh size is 0.5 x 0.5 mm, which is equal to the layer height  $h$ . Table 3.5 shows results of the element order convergence analysis. Figure 3.10 shows a plot of the temperature and the vertical displacement for different element orders. From elements of order quadratic and up, no significant improvement is found because the relative deviation is already very small. Therefore, changing from linear elements to quadratic elements is worth considering. The substantial decrease of relative deviation that is introduced by increasing the element order can be explained. When using quadratic elements, the displacement is represented by a quadratic function. Its derivative is a linear function and thus the strain field in the element becomes linear. This is the case for pure bending problems, such as the problem

Table 3.4: Vertical displacements (mm) of the element size convergence analysis

T (K)	Element size						
	0.5 mm	0.25 mm	0.125 mm	0.0625 mm	0.05 mm	0.025 mm	0.0125 mm
293	-0.0917	-0.1538	-0.1844	-0.1940	-0.1953	-0.1970	-0.1975
303	-0.2245	-0.3716	-0.4436	-0.4662	-0.4691	-0.4731	-0.4741
313	-0.7264	-1.1881	-1.4119	-1.4816	-1.4905	-1.5025	-1.5056
323	-2.9712	-4.7052	-5.5062	-5.7507	-5.7815	-5.8231	-5.8336
333	-9.0024	-13.0120	-14.5780	-15.0660	-15.1270	-15.1970	-15.1020
343	-12.0140	-16.5250	-18.1730	-18.6250	-18.7000	-18.7750	-18.7930
353	-12.2500	-16.8110	-18.4740	-18.9350	-18.9920	-19.0680	-19.0870
363	-12.2580	-16.8190	-18.4820	-18.9470	-19.0000	-19.0790	-19.0990
373	-12.2580	-16.8190	-18.4820	-18.9430	-19.0000	-19.0760	-19.0950

RD	43.4%	16.2%	4.59%	1.11%	0.66%	0.07%	-
----	-------	-------	-------	-------	-------	-------	---

that is solved here, where the deformation can be described by the arc of a circle. This means the analytical solution can be found by using quadratic elements.

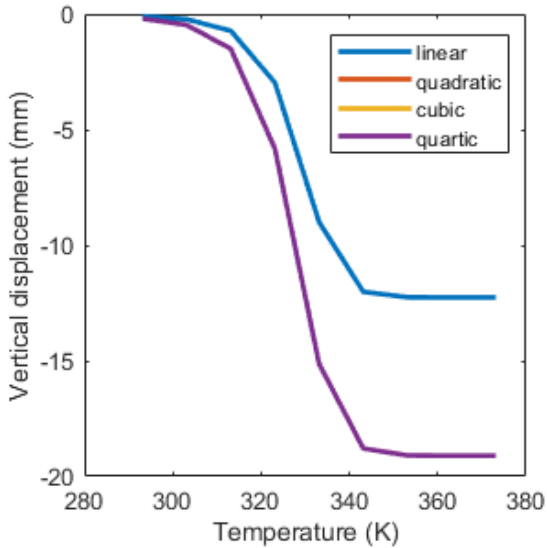


Figure 3.10: Temperature-vertical displacement plot for different element orders

Table 3.5: Vertical displacements (mm) of the element type convergence analysis

T (K)	Element order			
	linear	quadratic	cubic	quartic
293	-0.0917	-0.1963	-0.1973	-0.1973
303	-0.2245	-0.4731	-0.4741	-0.4741
313	-0.7264	-1.5052	-1.5063	-1.5063
323	-2.9712	-5.8355	-5.8369	-5.8368
333	-9.0024	-15.1360	-15.1390	-15.1380
343	-12.0140	-18.7900	-18.7910	-18.7910
353	-12.2500	-19.0920	-19.0930	-19.0930
363	-12.2580	-19.1040	-19.1050	-19.1050
373	-12.2580	-19.1000	-19.1010	-19.1010

RD	43.5%	0.09%	0.00%	-
----	-------	-------	-------	---

To further examine if these quadratic elements work for other transformation shapes than an arc of a circle, an irregular structure is tested. The irregular geometry is shown in Figure 3.11. The displacement is measured in two different points, which are indicated in green. The results of this analysis can be found in Tables 3.6 and 3.7. In this analysis, it is shown again that quadratic elements have a very small relative deviation compared to linear elements, although in this case it is not exactly zero. It can be concluded that the optimal mesh for this model has quadratic elements of 0.5 x 0.5 mm (or one element per layer in y-direction).

### 3.4 Validation

To get a preliminary insight in the validity of the model, the order of magnitude of the curvatures that are found using the model can be checked with simulation and experiment results from literature. The simulation results shown in Figure 3.8 from the paper by Geiss et al. (2019) are well suited for this purpose. Similar to our case study, the structure studied here consists of an active layer (blue) and a passive layer (red). The active layer has an initial strain of  $\epsilon = 0.05$ . One half domain will be considered, such that a simple bi-layered

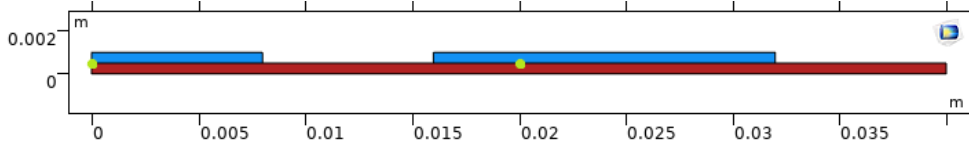


Figure 3.11: Irregular geometry

Table 3.6: Vertical displacements (mm) of the element type convergence analysis with an irregular structure of point 1

T (K)	Element type			
	linear	quadratic	cubic	quartic
293.15	-0.0150	-0.0239	-0.0248	-0.0249
303.15	-0.0249	-0.0428	-0.0438	-0.0439
313.15	-0.0634	-0.1207	-0.1220	-0.1222
323.15	-0.2482	-0.4739	-0.4771	-0.4772
333.15	-0.6433	-0.9276	-0.9353	-0.9366
343.15	-0.7886	-1.0831	-1.0918	-1.0936
353.15	-0.8027	-1.0976	-1.1064	-1.1083
363.15	-0.8054	-1.1004	-1.1093	-1.1111
373.15	-0.8078	-1.1029	-1.1117	-1.1136

Avg. error	35.7%	1.47%	0.18%	-
------------	-------	-------	-------	---

Table 3.7: Vertical displacements (mm) of the element type convergence analysis with an irregular structure of point 2

T (K)	Element type			
	linear	quadratic	cubic	quartic
293.15	0.0049	0.0095	0.0095	0.0095
303.15	0.0122	0.0239	0.0239	0.0240
313.15	0.0410	0.0864	0.0865	0.0866
323.15	0.1943	0.3645	0.3655	0.3653
333.15	0.5422	0.6477	0.6503	0.6507
343.15	0.6758	0.7488	0.7515	0.7520
353.15	0.6894	0.7592	0.7618	0.7623
363.15	0.6921	0.7612	0.7639	0.7644
373.15	0.6944	0.7630	0.7657	0.7662

Avg. error	28.0%	0.33%	0.09%	-
------------	-------	-------	-------	---

beam is obtained with a geometry similar to the basic geometry. The curvature around the  $X_2$ -axis for different volume fractions of Tango+ can be found in Table 3.9. The simulations are re-done using the COMSOL model described in this chapter, with an initial strain in the active layer of  $\varepsilon = 0.05$ . The resulting curvatures can be found in Table 3.9. The beam deforms into a half-circle just as in the published result, although the curvature is overestimated by 14-33 % by the COMSOL model. This difference can be explained by the fact that a linear elastic material model is used in the simulation, and the strains in this problem may not be small enough for this material model to give an accurate result. The hyperelastic material model used in the publication is more likely to simulate this problem with a higher accuracy.

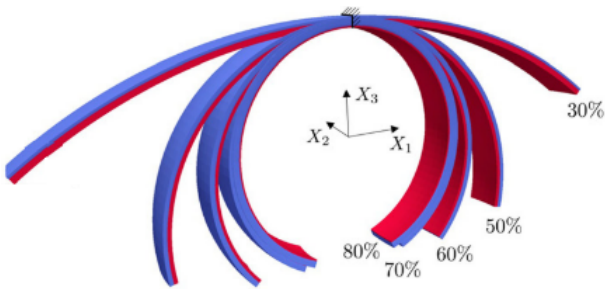


Table 3.8: Deformation simulation results for different volume fractions of Tango+ (Geiss et al., 2019)

Table 3.9: Comparison of published and COMSOL curvature results

Volume fraction of Tango+	$r_{literature}^{-1}$ (1/mm)	$r_{comsol}^{-1}$ (1/mm)	RD
0.3	0.015	0.020	33%
0.5	0.042	0.049	17%
0.6	0.054	0.063	17%
0.7	0.062	0.072	16%
0.8	0.064	0.073	14%

To find out whether the bending behaviour of the 2D model can be validated by an analytical model, a bimorph equation is used. The curvature of a bimorph actuator is given by the following equation (Shettar and Sheeparamatti, 2013):

$$\frac{1}{r} = \frac{6L_1L_2E_1E_2h_1h_2(h_1+h_2)(\alpha_1-\alpha_2)\Delta T}{(L_1E_1h_1^2)^2 + (L_2E_2h_2^2)^2 + 2L_1L_2E_1E_2h_1h_2(2h_1^2 + 3h_1h_2 + 2h_2^2)}, \quad (3.6)$$

where  $L_i$  is the length,  $E_i$  is the Young's modulus,  $h_i$  is the individual layer height,  $\alpha_i$  is the coefficient of

Table 3.10: Comparison of bimorph and COMSOL curvature results

$t$ (mm)	$\varepsilon$	$L$ (mm)	$r_{bimorph}^{-1}$ (1/mm)	$r_{comsol}^{-1}$ (1/mm)	<b>RD</b>
0.5	0.03	80	0.0263	0.0262	0.38%
1	0.03	80	0.0131	0.0130	0.76%
2	0.03	80	0.00660	0.00645	2.3%
0.5	0.06	80	0.0525	0.0508	3.2%
1	0.06	80	0.0263	0.0252	4.2 %
2	0.06	80	0.0131	0.0125	4.6 %

thermal expansion and  $\Delta T$  is the difference in temperature. Since both layers of the geometry have the same length and height ( $L_1 = L_2 = w$ ,  $h_1 = h_2 = h$ ), the equation can be further simplified to:

$$\frac{1}{r} = \frac{12E_1E_2(\alpha_1 - \alpha_2)\Delta T}{h(E_1^2 + E_2^2 + 14E_1E_2)}. \quad (3.7)$$

This formula is depth-independent. The arc angle is given by:

$$\theta = L/r, \quad (3.8)$$

where  $L$  is the length of the beam and the final vertical displacement is:

$$v = r - r \cos \theta. \quad (3.9)$$

The parameters of the default geometry are used:  $h_1 = h_2 = h = 0.5$  mm,  $L = 80$  mm and  $E_{tango} = E_1 = 0.6$  MPa. The strain in the active layer is specified as  $(\alpha_1 - \alpha_2)\Delta T = \varepsilon = 0.03$ . The values of  $E_{vero} = E_2$  are found by using the fitted Equation 3.1. The curvature results for the default parameters are plotted in Figure 3.12. They can be found in Table 3.10, along with some variations of the parameters. From the results can be concluded that the COMSOL model approximates the bimorph equation very well, because all relative deviations in final curvature are below 5%. The best performance is obtained for smaller strains.

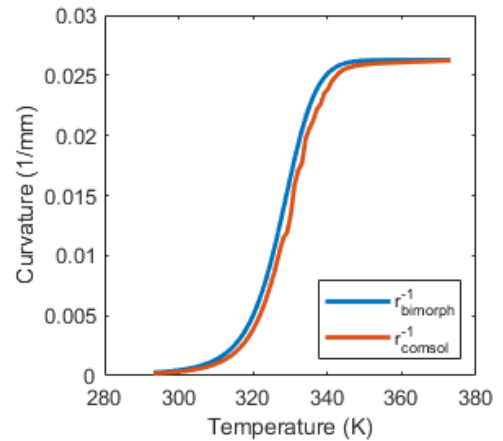


Figure 3.12: Curvature-temperature plot for COMSOL results and analytical results ( $t = 0.5$  mm,  $\varepsilon = 0.03$ )

# Chapter 4

## Development of the 3D-Model

To switch from 2D to 3D, some changes have to be made in the model. Those changes will be described in this chapter. Some modeling aspects are exactly the same as for the 2D model and therefore they will not be discussed here again. Thus, for more information on the material properties, simulating the glass transition effect, the temperature range, the geometrical model, the material model and the study type that is used, the reader is redirected to the previous chapter.

### 4.1 Model definition

The parameters of the default geometry in 3D can be found in Table 4.1. The geometry described here is a 3D version of the geometry described in the previous chapter. Again, the symmetry axis at  $x = 0.04$  m can be used, such that only half of the geometry has to be modeled. Half of the geometry, intersected at the plane of symmetry indicated as  $y, z$ -plane A, is shown in Figure 4.1. All boundaries of the geometry are free, with the exception of the symmetry plane. One point on this plane is fixed, while another point has a roller boundary condition with restricted movement in  $x$  and  $z$ -direction. Furthermore, the movement in the  $x$ -direction of the rest of the plane is restricted to zero. Instead of the mapped mesh that was used in the 2D modeling approach, a mesh consisting of tetrahedral elements will be used as shown in Figure 4.2.

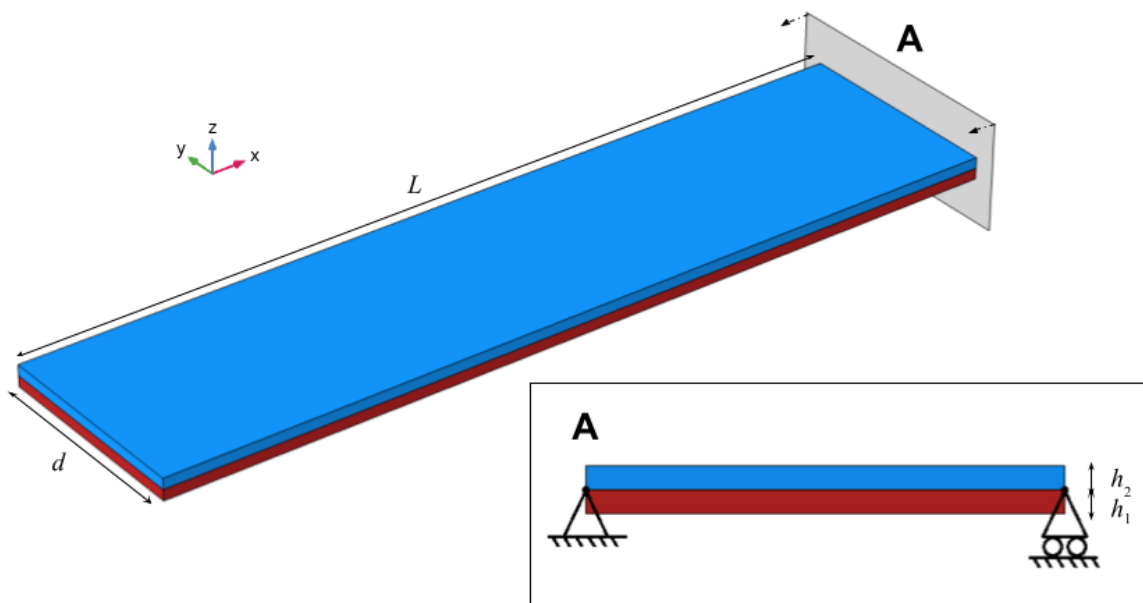


Figure 4.1: 3D geometry with active layer (blue) and passive layer (red), with boundary conditions indicated in cross-section A

Table 4.1: Dimensions of the 3D geometry

Parameter	Symbol	Value
Height of passive layer	$h_1$	0.5 mm
Height of active layer	$h_2$	0.5 mm
Length	$L$	80 mm
Depth	$d$	10 mm

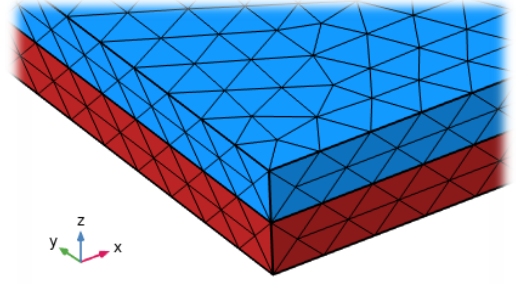


Figure 4.2: Mesh in 3D (zoomed in)

## 4.2 Convergence analysis

To find an appropriate mesh size for the 3D model, an element size convergence analysis is done. In 3D, the number of degrees of freedom is substantially larger than in 2D. This causes the computation time to become a limiting factor. When choosing the mesh size, a trade-off between minimizing the computation time and minimizing the relative deviation has to be made. Table 4.2 and Figure 4.3 show the results for a convergence analysis with tetrahedral elements with trilinear shape functions, with mesh sizes ranging from 0.5 mm to 0.0625 mm. The table also includes the computation times of all analyses. From the results can be concluded that using small elements leads to very high computation times, while the deviation relative to the finest mesh result is only slightly decreased. Ideally, analyses should be done with even smaller element sizes, until the relative deviation is approaching zero. However, there is a limitation of computational power, and running these even finer mesh analyses would cost an impractical amount of time.

Table 4.2: Vertical displacements (mm) of the element size convergence analysis

$T$ (K)	Element size			
	0.5 mm	0.25 mm	0.125 mm	0.0625 mm
293	-0.0604	-0.4396	-0.0923	-0.20151
303	-0.1824	-0.6528	-0.1767	-0.48985
313	-0.6494	-1.4469	-1.1896	-1.5596
323	-2.5844	-4.8422	-5.4355	-5.8732
333	-7.8724	-12.2770	-14.1430	-14.890
343	-10.5060	-15.4850	-17.2780	-18.141
353	-10.6300	-15.7800	-17.5200	-18.389
363	-10.6360	-15.7410	-17.5260	-18.396
373	-10.6360	-15.7410	-17.5260	-18.396

RD	51.4%	27.9%	19.3%	-
Computation time	0:01:00 hr	0:14:02 hr	3:38:22 hr	33:02:57 hr <sup>1</sup>

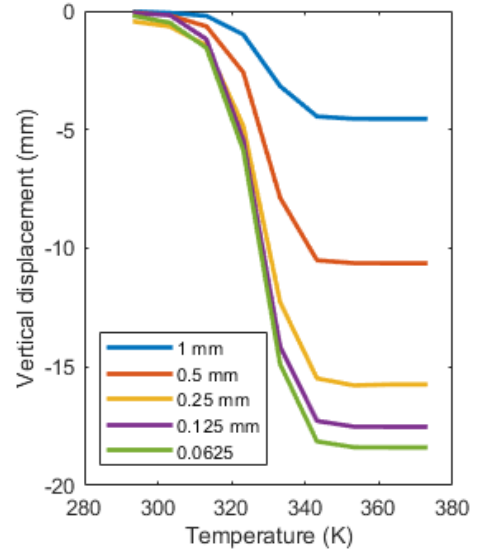


Figure 4.3: Temperature-vertical displacement plot for different element types

The use of trilinear shape functions makes the elements appear stiffer than they should be. When using linear elements, the displacement is represented by a linear function. These elements are unable to capture the kinematics of the deformation, which introduces a shear stress in the element. This additional shear stress changes the equilibrium equation, which leads to smaller deformations. This phenomenon is referred to as ‘shear locking’ (Briassoulis, 1989). A way to decrease the shear locking effect is to use elements of a higher order. To find out whether the solution can be approximated more accurately when using higher element orders, an element order convergence analysis is done. In Figure 4.4 and Table 4.3, results of this analysis with element orders ranging from linear to quartic can be found. In all cases, a mesh size of 0.5 mm is used. The results for the convergence analysis are similar to those that were found using the 2D modeling approach. Changing from

<sup>1</sup>This analysis was ran on a different computer, and its computation time can therefore not be compared to the other computation times.

linear to quartic discretization significantly decreases the relative deviation, while the computation time is still reasonably low. Further increasing the element order is not recommended, because it brings the disadvantage of high computation times while only slightly improving the relative deviation. Quadratic elements lead to more accurate displacements, because they allow for a better representation of a curved boundary. It is expected that quadratic elements lead to less accurate results for problems that do not involve pure bending only. For the 2D modeling approach, an analysis is done to examine such a problem. There, the relative deviation is only slightly larger than for the pure bending problem. For a detailed description of this analysis, the reader is redirected to Section 3.3.

Table 4.3: Vertical displacements (mm) of the element order convergence analysis

$T$ (K)	Element order			
	linear	quadratic	cubic	quartic
293	-0.0589	-0.2053	-0.2058	-0.2061
303	-0.1806	-0.4991	-0.5003	-0.5036
313	-0.6469	-1.5900	-1.5938	-1.5970
323	-2.5934	-6.0570	-6.0693	-6.0762
333	-7.8492	-14.9750	-15.0110	-15.0121
343	-10.4130	-18.2820	-18.2990	-18.2424
353	-10.6440	-18.5390	-18.5550	-18.5562
363	-10.6420	-18.5390	-18.5560	-18.5633
373	-10.6420	-18.5390	-18.5560	-18.5633

<b>RD</b>	52.35%	0.27%	0.10%	-
<b>Computation time</b>	0:01:09 hr	0:13:38 hr	1:06:10 hr	2:57:32 hr <sup>1</sup>

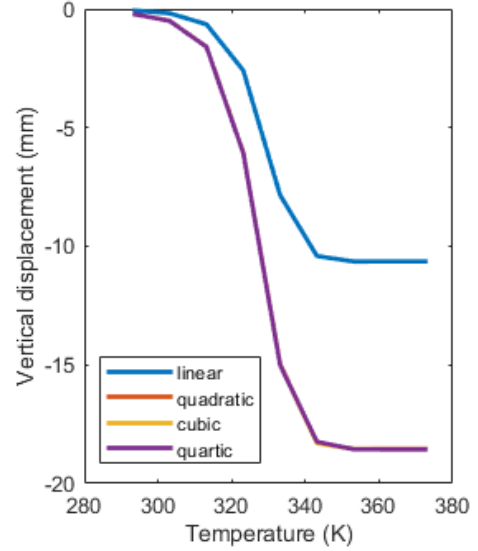


Figure 4.4: Temperature-vertical displacement plot for different element types

### 4.3 Validation

As a preliminary validation, the data obtained using the 3D modeling approach can be compared to that of the 2D modeling approach as described in Chapter 3. Figure 4.5 shows a comparison of the curvature results. The results of the 3D model match well with those of the 2D model. The average relative deviation is 4.0%.

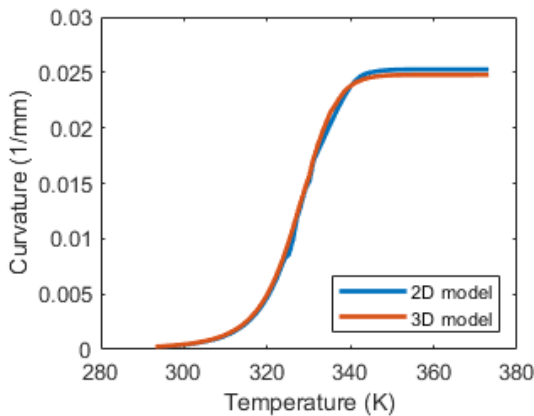


Figure 4.5: Curvature-temperature plot comparing 2D and 3D model results

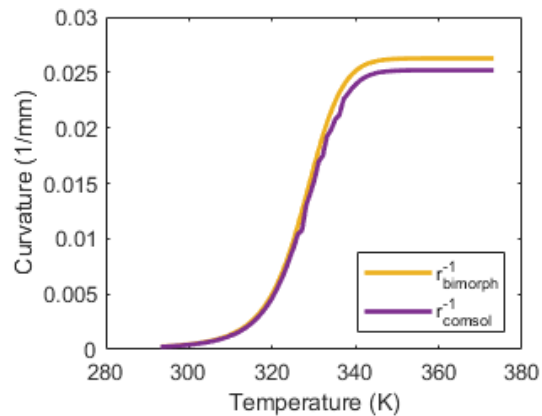


Figure 4.6: Curvature-temperature plot for COMSOL results and analytical results ( $t = 0.5$  mm,  $\varepsilon = 0.03$ )

The 3D modeling approach can be validated with literature in the same way as the 2D modeling approach. A comparison of the curvature results from the experiments of Geiss et al. (2019) and the curvature results from the 3D COMSOL model can be found in Table 4.4. The relative deviation values in the curvatures of the 3D model designed in COMSOL range from 2.6-12%. This means the 3D model approaches the published results better than the 2D model, where relative deviations in the range of 14-33% were found. As explained earlier,

the deviation is probably caused by the fact that another material model is used in the publication.

Table 4.4: Comparison of published and COMSOL curvature results (3D)

<b>Volume fraction of Tango+</b>	$r_{literature}^{-1}$ (1/mm)	$r_{comsol}^{-1}$ (1/mm)	<b>RD</b>
0.3	0.015	0.014	4.7%
0.5	0.042	0.041	2.6%
0.6	0.054	0.058	6.5%
0.7	0.062	0.070	12%
0.8	0.064	0.070	8.6%

Equation 3.7, the bimorph equation that was used to validate the 2D modeling approach, can be used in the 3D case as well. Table 4.5 shows the curvature results obtained by using the bimorph equation and the COMSOL model. In Figure 4.6, the curvature results are plotted. The relative deviations compared to the bimorph equation curvature results range from 3.8 to 11.4%. This makes the average relative deviation of the 3D model slightly larger than the average relative deviation of the 2D model. This result was expected, since the bimorph equation is based on the same plane strain assumption as the 2D model.

Table 4.5: Comparison of bimorph and COMSOL curvature results (3D)

$t$ (mm)	$\varepsilon$	$L$ (mm)	$r_{bimorph}^{-1}$ (1/mm)	$r_{comsol}^{-1}$ (1/mm)	<b>RD</b>
0.5	0.03	80	0.0263	0.0249	5.3%
1	0.03	80	0.0131	0.0126	3.8%
2	0.03	80	0.00660	0.00632	4.2%
0.5	0.06	80	0.0525	0.0465	11%
1	0.06	80	0.0263	0.0242	8.0%
2	0.06	80	0.0131	0.0122	6.9%

# Chapter 5

## Topology optimization method

The topology optimization is aimed at achieving a particular deformation at the final temperature  $T_f$ . It uses the solution of the first study, as described in Chapter 3: ‘*Development of the 2D model*’ and Chapter 4: ‘*Development of the 3D model*’, as an initial solution. The SIMP method will be used to do the topology optimization. The topology optimization will only be performed on the active material layer.

### 5.1 Penalized Variables

The Young’s modulus of the material layer that is optimized, is penalized such that less stiffness is provided for intermediate density values. The penalized Young’s modulus  $E(\theta_p)$  is obtained by multiplying the Young’s modulus  $E_0$  of the optimized material with the penalized material factor  $\theta_p$ :

$$E(\theta_p) = E_0\theta_p = E_0(\theta_{min} + (1 - \theta_{min})\theta^p), \quad (5.1)$$

where the minimum penalized material volume factor  $\theta_{min}$  is chosen as  $10^{-9}$  and the penalization factor is  $p = 3$ . The stress in the top layer, which is induced by printing, is modeled as an initial stress in the top layer material. To avoid stress being assigned to intermediate density values, the stress will be penalized as well. This makes sure only solid areas have an initial stress. The stress  $\sigma_0$  is penalized by multiplying it with the penalized material volume factor  $\theta_p$ :

$$\sigma(\theta_p) = \sigma_0\theta_p = \sigma_0(\theta_{min} + (1 - \theta_{min})\theta^p), \quad (5.2)$$

where the ‘default’ initial stress  $\sigma_0$  is equal to 18 kPa.

### 5.2 Objective Function

The following objective function is used:

$$f = w \left( \frac{v - v_{target}}{v_{target}} \right)^2 + (1 - w)V, \quad (5.3)$$

where  $v$  is the vertical tip displacement and  $v_{target}$  is the targeted vertical tip displacement.  $V$  is the average material volume fraction, which is the normalized volume. The first term,  $(\frac{v - v_{target}}{v_{target}})^2$ , is what can be referred to as a ‘displacement matching’ function, because the difference between the displacement and the targeted displacement is minimized. The second term,  $V$ , minimizes the volume. Minimizing the volume helps in decreasing grey areas in the optimization. The weight factor  $0 \leq w \leq 1$  is introduced to be able to change the importance of the difference terms in the function.

Figure 5.1 shows 2D topology optimization results for different weights  $w$ . Voids are indicated in white, while solid active material is indicated in black. The passive layer is shown in red. To visually demonstrate the effect of  $w$ , the individual layer height of the initial geometry is increased to  $h_1 = h_2 = h = 4$  mm. The targeted vertical tip displacement in each simulation is set to  $v_{target} = -2$  mm. Table 5.1 shows the number of iterations,

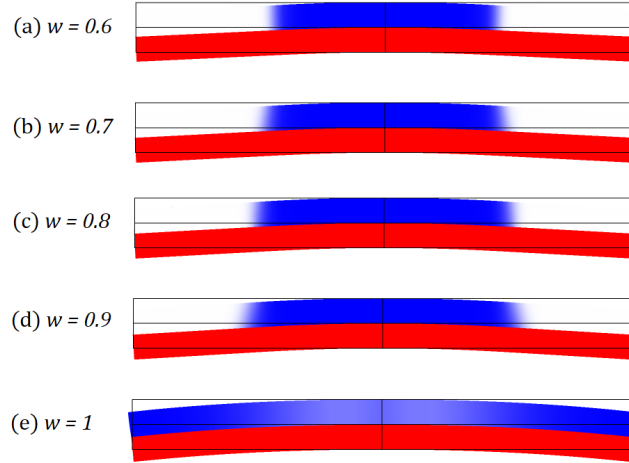


Figure 5.1: Topology optimization results for different weight factors  $w$  (blue: active material, red: passive material)

the vertical tip displacement and the material volume fraction for different values of  $w$ . From these results, it can be concluded that including the volume term leads to a much more defined topology. However, if too much emphasis is put on this volume term, the difference between the vertical displacement and the targeted displacement becomes too large. A weight factor of  $w = 0.9$  leads to both a well-defined topology and a sufficient displacement match. Unfortunately, a high number of iterations is needed for this value.

Table 5.1: Topology optimization results for different weights  $w$

$w$	#iterations	$v$ (mm)	deviation from $v_{target}$	$V$
0.6	15	-1.6106	19%	0.47085
0.7	55	-1.7275	14%	0.50418
0.8	42	-1.8155	9.2%	0.53449
0.9	152	-1.9168	4.2%	0.57131
1	9	-2.0038	0.19%	0.90659

### 5.3 Topology optimization results

In the initial study, the final tip displacement using the default parameters is -19 mm. The targeted vertical tip displacement must be chosen smaller than this value, otherwise the objective is unattainable. Figures 5.2 and Table 5.2 show topology optimization results for different target displacements. In all cases, the vertical tip displacements are close to the targeted vertical tip displacements. The target displacement is approached by the optimizer by creating gaps in the active layer, starting in what seems an arbitrary position in the beam. The introduction of gaps neutralizes the stress, which results in a smaller deflection.

Table 5.2: Topology optimization results for different target displacements  $v_{target}$

$v_{target}$ (mm)	#iterations	$v$ (mm)	deviation from $v_{target}$	$V$
0	14	0.0	0.0%	1.00
-5	413	-4.9517	1.0%	0.21
-10	7	-9.6720	3.3%	0.73
-15	52	-14.373	4.2%	0.49

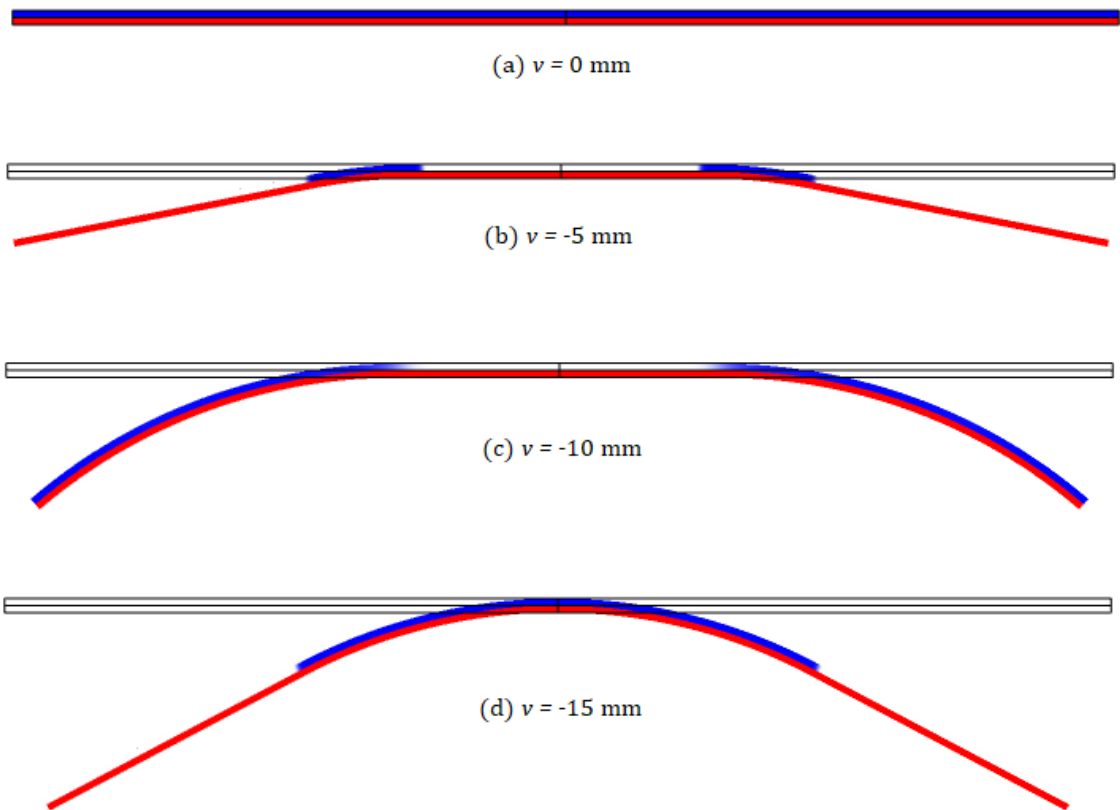


Figure 5.2: Topology optimization results for different target displacements  $v_{target}$  (blue: active material, red: passive material)

# Chapter 6

## Variations and Applications

This chapter demonstrates the capabilities of the modeling and topology optimization approach that is described earlier in this report, by showing variations and its potential applications. Variations of the original approach include an optimization study to find the layer thickness ratio for which the largest curvature is obtained. The resulting layer ratio is validated by comparing it to the optimal layer ratio that is found using an analytical approach. Also, a numerical two-way transformation is demonstrated by applying the initial stress in both of the layers instead of only in the active layer. This allows the structure to transform from the initial configuration to a deformed configuration, and to return again to the initial deformation under further heating. Additionally, different ways to achieve a target shape are explored, by adding more probe points and by matching an edge of the material domain to a target function that describes the desired shape. The possibilities that are introduced by adding a second active layer are studied. Lastly, an example of a potential application in expanding lattices is shown.

### 6.1 Optimal layer ratio geometry

In the default geometry, both layers have the same height. It is possible to change the layer heights to achieve a larger curvature. This section shows an optimization of the ratio between the two layers, such that the largest possible curvature can be achieved. To find the optimal layer height ratio, the simulation is done for multiple layer heights where the total layer height is always equal to one. Results of these simulations can be found in Table 6.1, and are plotted in Figure 6.1. From the results, it can be concluded that for the considered material combination and geometry, the maximum curvature is achieved when the thickness of the active material layer is 0.75 mm and the thickness of the passive material layer is 0.25 mm. This layer ratio of 75% active material can be used as an initial geometry for the topology optimization study, to get maximized tip displacements for a relatively low initial stress in the active layer. The simulation results can be compared to analytical results generated using Equation 3.6, which are plotted in Figure 6.1 as well. The analytical approach leads to the same optimal thickness ratio, which validates the optimization study.

### 6.2 Two-way transformation

A simple method to achieve a two-way transformation is to introduce a compressive prestress in the glassy polymer layer as well as in the rubbery polymer, such that both layers become active. For simplicity, the same prestress value of 18 kPa is used in both of the material layers. This two-way 4D-transformation can potentially be used in grip- and release systems. Two (fictive) polymers with equal Young's moduli above a certain temperature  $T_f$  are used in this simulation. The structure is gradually heated from room temperature  $T_i$  to the glass transition temperature of  $T_g = 370$  K. At a temperature of approximately 340 K, the bottom layer has softened enough to bend downwards due to the prestress that is being released from the top layer. A maximum displacement is reached at  $T_g$ . The structure remains in this configuration when the temperature is decreased. It can be brought back to the initial configuration by increasing the temperature to  $T_f$ . As the temperature is increased further, the Young's modulus of the top layer approaches that of the bottom layer. In this temperature region, the structure is transforming back to the original configuration because of the prestress in the top layer. Heating above  $T_f = 400$  K has no further effect on the structure, because the Young's modulus remains constant. After the second transformation, no prestresses are left in the material. Therefore, when the sample is cooled down and the stiffness of the passive layer increases, it remains in the original configuration.

Table 6.1: Curvature results for different layer thickness ratios

Passive layer thickness (mm)	Active layer thickness (mm)	Curvature, simulation (1/mm)	Curvature, analytic (1/mm)
0.55	0.45	0.0203	0.0213
0.50	0.50	0.0252	0.0263
0.45	0.55	0.0302	0.0313
0.40	0.60	0.0350	0.0361
0.35	0.65	0.0391	0.0401
0.30	0.70	0.0421	0.0431
0.25	0.75	0.0439	0.0447
0.20	0.80	0.0444	0.0449
0.15	0.85	0.0436	0.0438
0.10	0.90	0.0412	0.0411

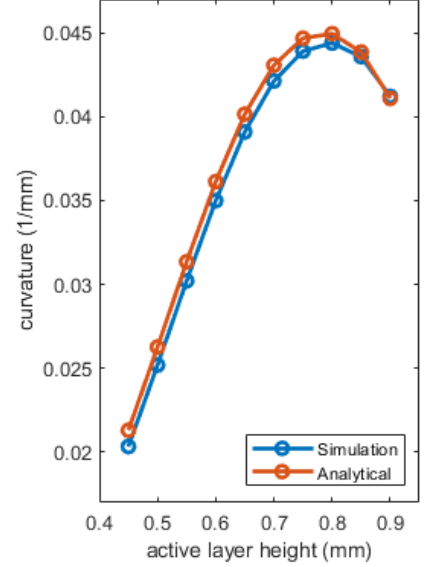
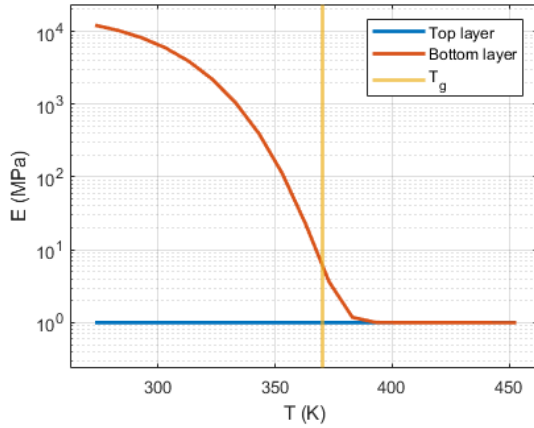
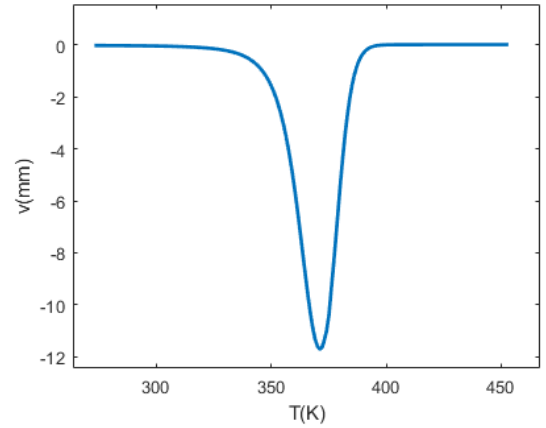


Figure 6.1: Active layer thickness vs curvature



(a) Glass transition curves of the polymers



(b) Displacement response

Figure 6.2: Two-way transformation properties

### 6.3 Multiple probe points

When including more probe points in the optimization, the objective function as stated in Equation 5.3 has to be slightly reformulated:

$$f = w \left( \sum_{i=1}^N \left( \frac{v_i - v_{i,target}}{v_{i,target}} \right)^2 \right) + (1 - w)V, \quad (6.1)$$

where  $v_i$  is the vertical displacement in point  $i$  and  $v_{i,target}$  is the targeted vertical displacement in point  $i$ . In the case that  $v_{i,target}$  is zero, it is replaced in the denominator by the normalizing term  $v_{norm} = 1$  mm, such that numerical errors due to division by zero are avoided.  $N$  is the number of probe points that is going to be examined.  $V$  is the average material volume fraction, which is a normalized volume of which the maximum value is equal to 1. The weight factor is chosen as  $w = 0.9$ . In the previous analyses, a target displacement was described for a probe point at the tip of the geometry only. Adding more probe points could lead to more complex topology results. However, when choosing target displacement values for the probe points, it should be taken into account that not all displacements can be realised. In the case of an unachievable target displacement, the optimizer will find a design that that is as close to the objective as possible. The earlier obtained maximum displacements indicate the range of target displacements that are feasible.

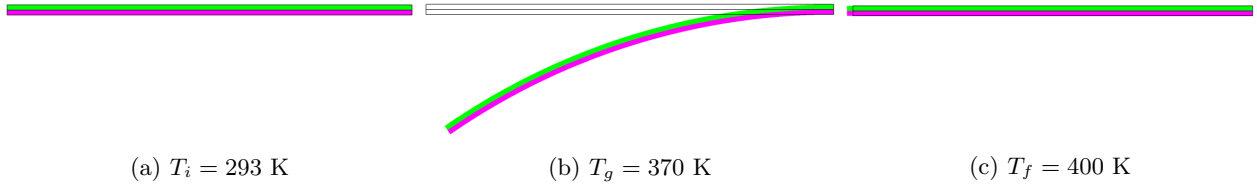


Figure 6.3: Deformation at various temperatures (green: low  $T_g$  polymer, magenta: high  $T_g$  polymer)

In the example shown in Figure 6.4a, two probe points are used. The  $x, y$ -coordinates of point 1 are  $(0, 0.5)$  mm and those of point 2 are  $(20, 0.5)$  mm. The target displacements of point 1 and point 2 are respectively set to  $v_{1,target} = -5$  mm and  $v_{2,target} = 0$  mm. The value of  $v_{1,target}$  is approximately the displacement the fully solid geometry would have, if the width was twice as small. The optimizer is therefore expected to produce a topology where the left half of the active material domain is solid and the right half is a void. The final displacements are  $v_1 = -4.995$  mm and  $v_2 = -0.002$  mm, which are both very close to the target displacements. The material distribution looks as expected. The average volume fraction is 0.52, which indicates that approximately half of the active material domain is solid. In a second example, shown in Figure 6.4b, the optimizer will be triggered to initiate a void elsewhere by choosing the target displacements as  $v_{1,target} = -10$  mm and  $v_{2,target} = -5$  mm. Here, the final displacements are  $v_1 = -10.706$  mm and  $v_2 = -4.299$  mm.

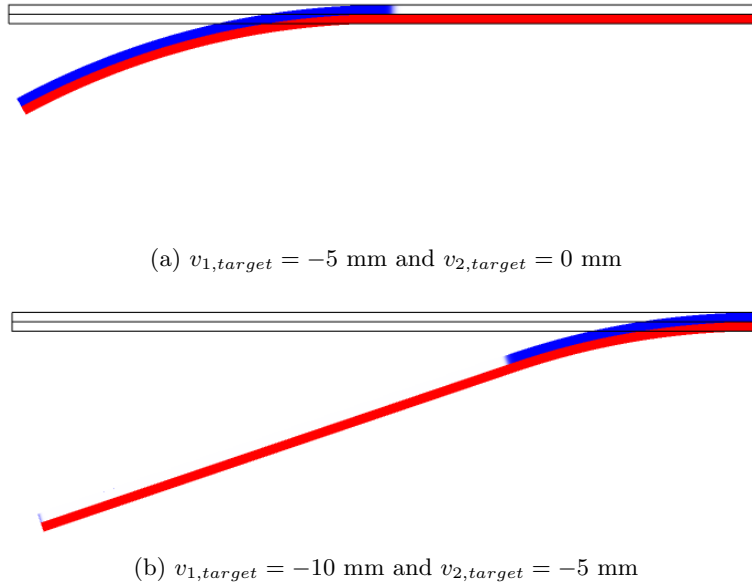


Figure 6.4: Multiple probe topology optimization results (blue: active material, red: passive material)

## 6.4 Shape matching

Instead of matching points in the geometry to targeted displacements, the edge (or plane in 3D) intersecting the active and passive layer can be matched to a target function that describes the desired shape. This method is similar to the methods used in the publications of Hamel et al. (2019) and Maute et al. (2015), discussed in Sections 2.4.1 and 2.4.7 respectively. The deformed shape will be matched to a function of the form:

$$y = -A \left( \frac{2(x-L)}{L} \right)^n. \quad (6.2)$$

This shape describing function is modeled as a boundary in the model. It is implemented in the objective function using a point-to-point map, which is called an ‘extrusion operator’ in the COMSOL software (Kindo, 2015). The type of extrusion operator that is used here is the general extrusion component coupling (Frei, 2017). It is specifically designed to find the point on a boundary for which the distance with another pre-defined point is smallest. Using mapping, variables from one component are mapped to another. In the problem described here, mapping involves two geometric entities: the target shape and the transforming structure. To find the distance between these two, the components of the transforming structure boundary should be mapped onto the

target shape boundary. The distance between the target shape and the transforming structure can be defined as:

$$d = \sqrt{(x_{target} - x)^2 + (y_{target} - y)^2}, \quad (6.3)$$

where  $x_{target}$  and  $y_{target}$  are the coordinates of the target shape boundary, and  $x$  and  $y$  are the coordinates of the transforming structure boundary mapped onto the target shape boundary. Distance function  $d$  is integrated over the boundary to get a scalar variable. This variable is replaced for the displacement matching term in the original objective function shown in Equation 5.3. Results for different values of  $A$  and  $n$  can be found in Table 6.2. Note that the target shape is given in green, and in all cases the generated structure is able to match it closely.

Table 6.2: Shape matching topology optimization results (green: target function, blue: active material domain, red: passive material domain)

$A = 2 \text{ mm}, n = 2$	
$A = -2 \text{ mm}, n = 3$	
$A = 0.5 \text{ mm}, n = 4$	
$A = -0.1 \text{ mm}, n = 5$	

## 6.5 Multiple active layers

In this section, a geometry with two active layers will be analyzed. The geometry is shown in Figure 6.5. It is slightly longer than the default geometry and a second Tango+ active layer is added at the bottom. The prestress in both active layers is equal and has a value of  $\sigma_0 = 18 \text{ kPa}$ . Two probe points are used, located at the tip and at half of the beam. The addition of a second active layer increases the design freedom, since it introduces the possibility to bend both upwards and downwards.

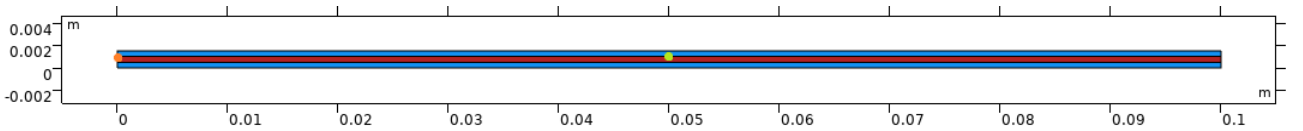


Figure 6.5: Geometry with two active layers (blue) and one passive layer (red) with probe point 1 (orange) and probe point 2 (green)

Since multiple probe points are considered in the optimization, the objective function described in Equation 6.5 can be used. Having two active layers introduces the need for some adaptations to the standard topology optimization approach as described earlier. In topology optimization processes with one active and one passive layer, the results from the initial study were used as an initial expression for the topology optimization. However with two active layers, no bending occurs in the initial study. Therefore, using the results of the initial study does not improve the topology optimization convergence. Instead, the prestress loading parameter is increased step-wise from zero to the actual initial stress  $\sigma_0$  during each optimization step. The goal is to achieve a sine-like deformation, and therefore the target displacements are chosen as  $v_{1,target} = 10 \text{ mm}$  and  $v_{2,target} = -10 \text{ mm}$ . The result of the topology optimization can be found in Figure 6.6a. Material and void

areas are well-defined and the displacements in the target points are found as  $v_1 = 10.746$  mm and  $v_2 = -10.683$  mm, which are close to the targeted displacements. A similar simulation is performed in 3D with the same dimensions and a depth of  $d = 5$  mm. Target displacements of  $v_{1,target} = 10$  mm and  $v_{2,target} = -10$  mm are imposed to probe edges instead of probe points, located at positions equivalent to the probe points in the 2D simulation. For this simulation, the displacement results are  $v_1 = 10.369$  and  $v_2 = -8.9173$ . The slight difference in topology compared to the 2D result can be explained by the fact that the optimizer has an additional design freedom in the in-plane direction. Besides that, a different element shape is used in the 3D mesh.

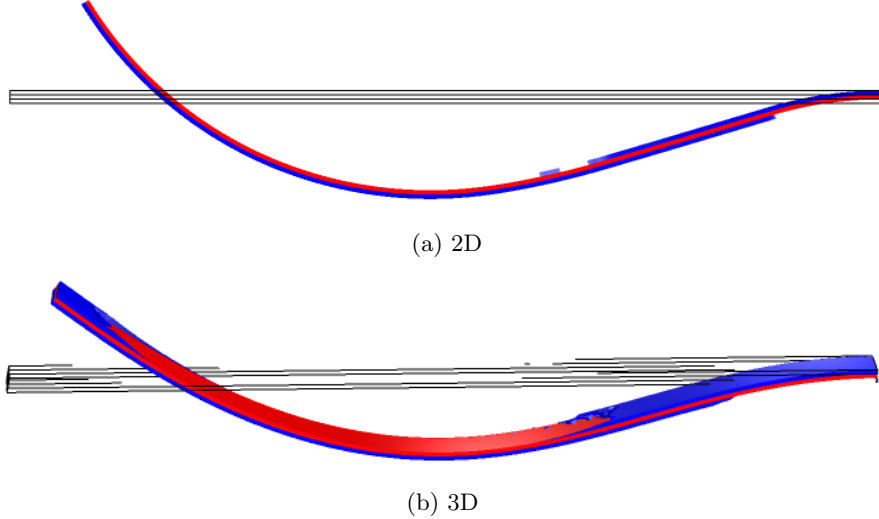


Figure 6.6: Topology optimized three-layer beam

Instead of using probe points to define the topology optimization's objective, a target function can be used, as introduced in the previous section. Having two active layers allows for more complex target shapes. A three-layer beam as shown in Figure 6.5 is matched to the following third order target function:

$$y = Ax(x - B)(x - C), \quad (6.4)$$

where  $A = -100$ ,  $B = 0.1$  and  $C = 0.095$ . Figure 6.7 shows the optimization result for matching the initial geometry in Figure 6.5 to the target shape described by Equation 6.4.

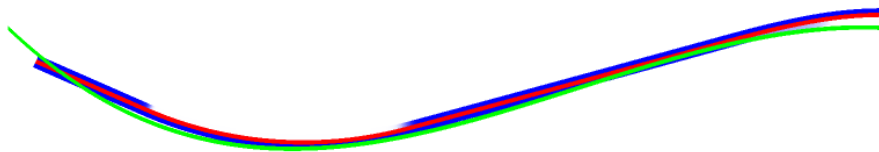


Figure 6.7: Topology optimized three-layer beam in 2D, matched to Equation 6.4

## 6.6 Topology optimization in active and passive layer (2D)

In the previous topology optimization studies, topology optimization was only performed in the active material domain. But in addition, it could be applied to the passive material domain. It can be studied whether the target displacements are approached better when topology optimization is used in both of the material layers. For this purpose, the optimization described in Section 6.5 is re-done with topology optimization in the active and passive material domain. The topology optimization method is identical for both materials. The objective function has to be changed slightly to

$$f = w \left( \sum_{i=1}^N \left( \frac{v_i - v_{i,target}}{v_{i,target}} \right)^2 \right) + (1 - w) \frac{V_{active} + V_{passive}}{2}, \quad (6.5)$$

where  $V_{active}$  is the volume fraction of the active material and  $V_{passive}$  is the volume fraction of the passive material. The weight factor is equal to  $w = 0.9$ . The topology resulting from optimization with this objective

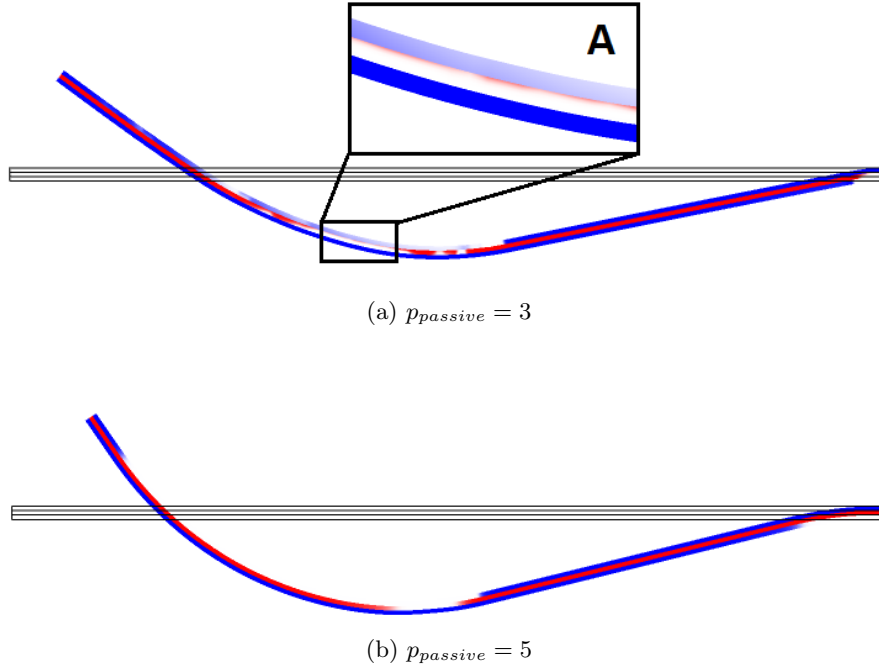


Figure 6.8: Topology optimization results with two active layers and topology optimization in all layers

can be found in Figure 6.8a. With this topology, deflections of  $v_1 = 11.241$  mm and  $v_2 = -8.8561$  mm are found, which show a substantial deviation with respect to the targeted displacements. In beam segments where all of the three layers are solid, no bending occurs. This behaviour occurs because the prestresses in the top and bottom layer are equal. However, segment A in the figure shows unexpected deformation behaviour. In this segment, the material volume fraction of the passive layer is equal to zero, but bending still occurs. When zooming in on this section, it can be seen that a very thin layer of passive material is present directly below the top active layer. Besides that, the topology has many intermediate density values. To avoid these problems, the penalization factor in the passive material is increased to  $p_{passive} = 5$ . The result in Figure 6.8b shows a design with less intermediate density areas compared to the previous design and the displacements are slightly closer to the targets:  $v_1 = 11.098$  mm and  $v_2 = -10.479$  mm.

## 6.7 Expanding lattice

The optimization approach can be used to create a lattice that expands in the  $y$ -direction. Such a lattice could find its use in self-assembling applications. The initial geometry of one component in the lattice is shown in Figure 6.9a. This geometry consists of two connected three-layer beams as described in Section 6.5. The boundary conditions are shown in Figures 6.9b and 6.9c. In the topology optimization, the objective is to achieve target displacements of  $v_{1,target} = 10$  mm for point 1 and  $v_{2,target} = -10$  mm for point 2 to get a total expansion of 20 mm. The symmetry of the geometry in  $y$ -direction is exploited to shorten the computation time. The result of the topology optimization is shown in Figure 6.10. The geometry obtained in the topology optimization is slightly modified to fit in a lattice structure. The total expansion in  $y$ -direction at  $T = 373$  K is four times the initial height at  $T = 293$  K.

A downside of the expanding lattice discussed previously, is that the width in  $x$ -direction of the structure decreases as it expands in the  $y$ -direction. For some applications, expansion in both the  $x$  and  $y$ -direction is necessary. Thus, the structure should have a negative Poisson's ratio in the rubbery state. Structures that exhibit such behaviour are referred to as auxetic structures (Liu and Hu, 2010). An example of an auxetic structure can be found in Figure 6.11a and b. This structure is intuitively designed and exhibits an expansion of 9.4% during the 4D-transformation. A second auxetic structure is designed with the help of topology optimization, as shown in Figure 6.11c and d. The structure expands with 9.8% compared to the original size.

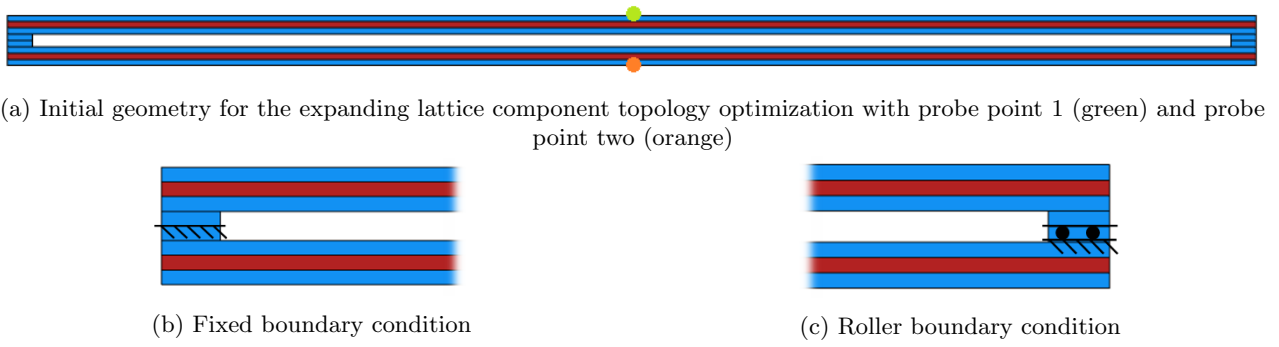


Figure 6.9: Initial geometry

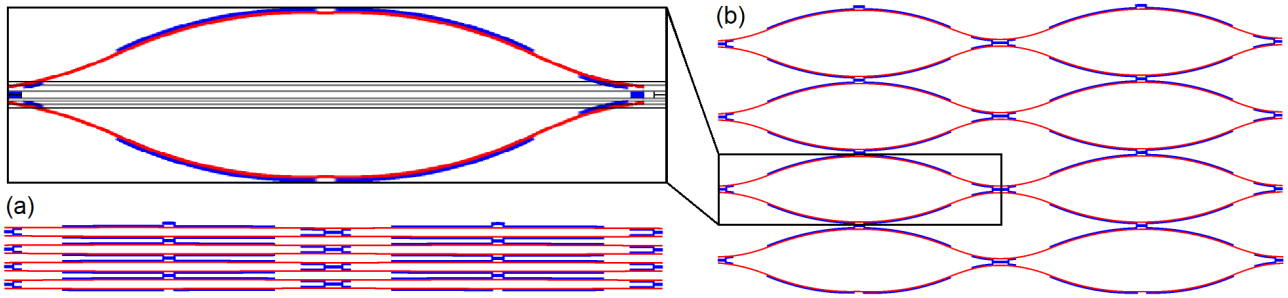


Figure 6.10: Topology optimization result of an expanding lattice, (a)  $T = 293K$ , (b)  $T = 373K$

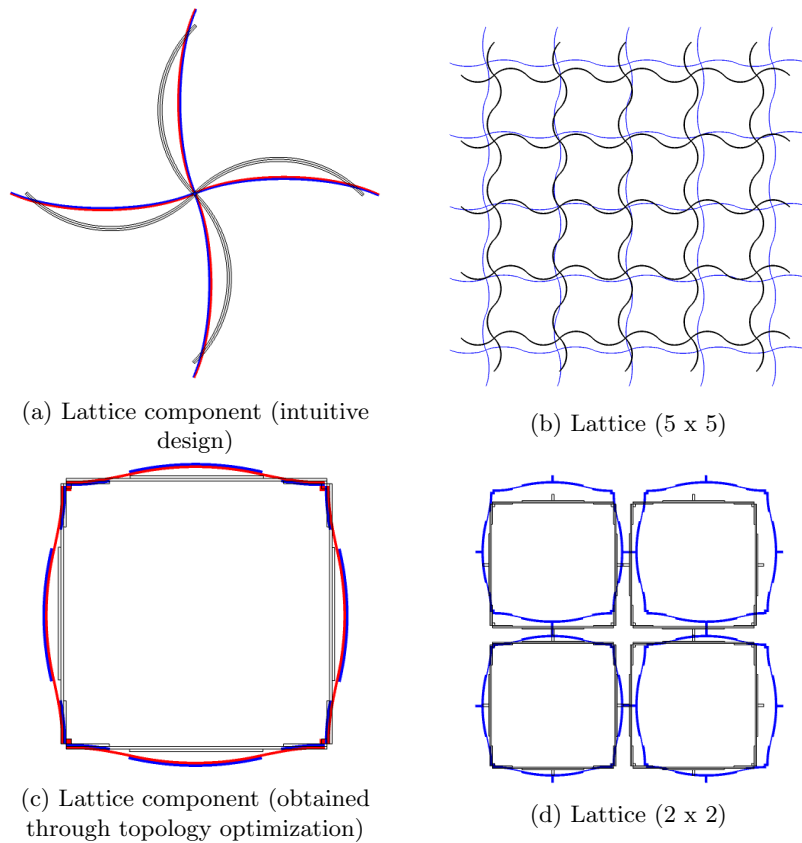
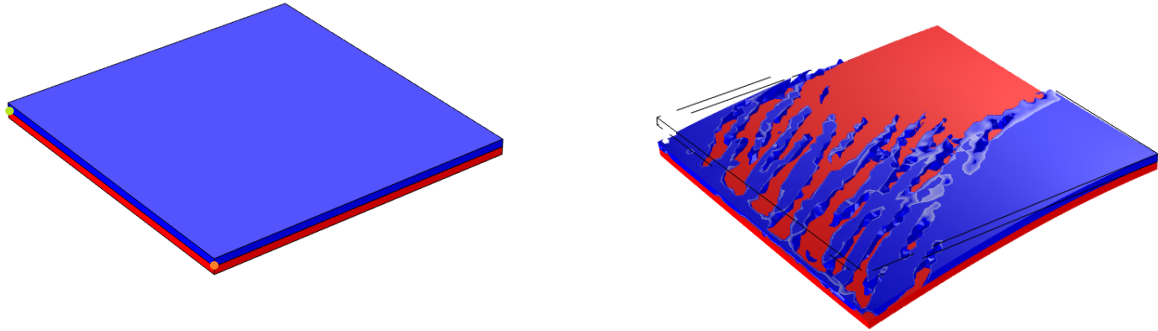


Figure 6.11: Auxetic structures (black:  $T = 293 K$ , red/blue:  $T = 373 K$ )

## 6.8 Twisting deformation (3D)

In the following topology optimization, a square, three-dimensional geometry as shown in Figure 6.12a is used as a base. This geometry is a modified version of the default geometry in the 3D modeling approach, where the depth is changed to  $d = 40 \text{ mm}$  and the layer height is changed to  $h_1 = h_2 = 1 \text{ mm}$ . In the first example the

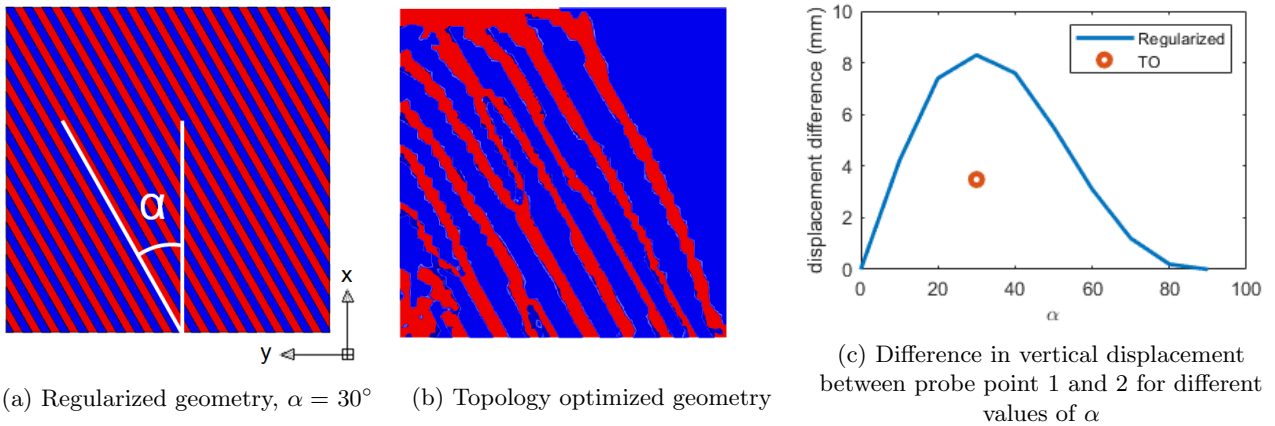
following target displacements are set:  $v_{1,target} = -5$  mm and  $v_{2,target} = -3$  mm, aiming at a combination of bending and twisting deformation. The results in Figure 6.12b show a distinctive diagonal pattern in the active layer. The final displacements are  $v_{1,target} = -4.964$  mm and  $v_{2,target} = -2.972$  mm.



(a) Initial geometry with probe point 1 (orange) and probe point 2 (green) (b) Topology optimized geometry at  $T = 373$  K

Figure 6.12: Twisting deformation problem

From this topology optimization result can be learned that diagonal strips of active material on top of the passive material lead to a combined bending-twisting deformation. This mechanism can be further analyzed, to find the angle of the diagonal strips for which the twisting deformation is maximized. A regularized version of the geometry is created, where variable  $\alpha$  is the angle between the active strips and the  $x$ -axis as shown in Figure 6.13a. The simulation is repeated for different values of  $\alpha$ , ranging from  $0^\circ$  to  $90^\circ$ . The results in Figure 6.13c show that the largest difference in displacement of the corner points (i.e. maximum twisting) is obtained for an angle of  $30^\circ$  between the active strips and the  $x$ -axis. This corresponds to the angle that was found in the topology optimization result in Figure 6.13b, where the objective was to maximize the difference in displacement between the two free corners. This difference is smaller in the topology optimization result, because the diagonal strip width is limited by the Helmholtz filter. This filter constrains the minimum feature size in the optimization, as discussed in Section 2.3.4.



(a) Regularized geometry,  $\alpha = 30^\circ$  (b) Topology optimized geometry

(c) Difference in vertical displacement between probe point 1 and 2 for different values of  $\alpha$

Figure 6.13: Comparison of regularized angle optimization and topology optimization

# Chapter 7

## Experiments

### 7.1 Experiment goal

Doing experiments with the topology optimized structures is a way to validate the 2D and 3D modeling approaches that are created during this research project. To be able to do experiments, real samples have to be printed and tested. Both are done at the University of Pavia, Italy. The control variable in the experiment is the temperature, which is increased gradually to deform the printed sample. As described earlier, the principle of the 4D-transformation relies on the prestress in one of the printed layers. However, it is not possible to precisely tune the stress introduced by the printing process. For that reason, a first set of experiments is done with bi-layered structures of different sizes. The data obtained during these experiments represent the relation between material layer height and deformation. These data are used to calibrate the numerical model to find the prestress. Once this prestress is found, topology optimized structures can be generated, printed and tested.

### 7.2 Sample specifications

The materials that are used in the modeling approach described in the previous chapters of this report are unfortunately not available for printing. Instead, materials with similar properties are used. For the passive layer, as a replacement of the VeroClear material, Acrylonitrile Butadiene Styrene (ABS) is used. The active layer is printed with thermoplastic polyurethane (TPU) instead of Tango+. The material properties of these materials are listed in Table 7.1 and Figure 7.1 (Selva-Priya et al., 2019).

Table 7.1: Material properties of TPU and ABS

Property	TPU	ABS
Young's modulus	12 MPa	<i>see Figure 7.1</i>
Poisson's ratio	0.48	0.3
Mass density	1.47 g/cm <sup>3</sup>	1.11 g/cm <sup>3</sup>
Glass transition temperature	-35 °C	85 °C

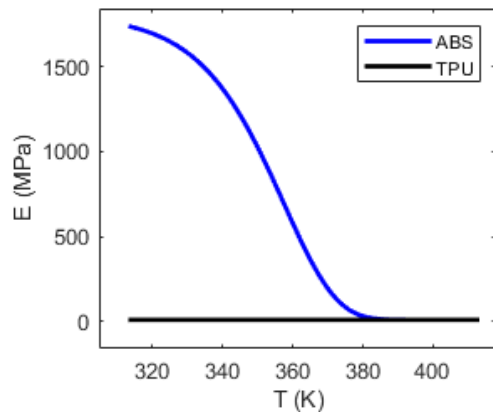


Figure 7.1:  $E - T$  curve of TPU and ABS

Five different groups (labeled A-E) of uniform bi-layered samples with varying layer heights  $h_1$  and  $h_2$  are printed for the purpose of initial stress calibration, as shown in Figure 7.2 and Table 7.2. A mounting part is added to the bi-layer structure, to be able to easily clamp it while testing. Three samples are made for each sample group, such that the experiments can be repeated. With new settings adapted to the printing materials, two printing sample designs were created using topology optimization. Both are based on topology optimizations considered earlier in this report. Sample F in Figure 7.3a is designed such that the free corners have a difference in vertical displacement. Its design is very similar to the twisting deformation design shown in Figure 6.12b of the previous chapter. Sample G, which is shown in Figure 7.3b, is designed to deform into a

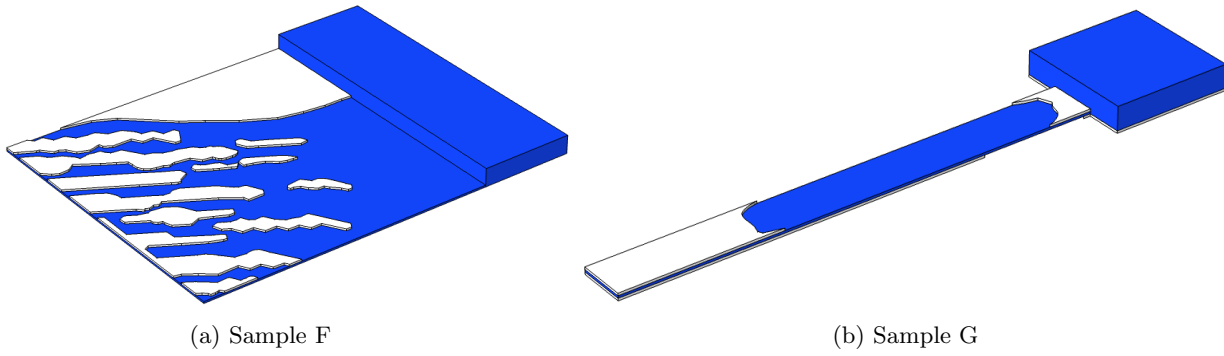


Figure 7.3: Sample designs obtained with topology optimization (blue: ABS, white: TPU)

sinusoidal shape. It is based on the topology optimization of the three-layer beam in Figure 6.6b.

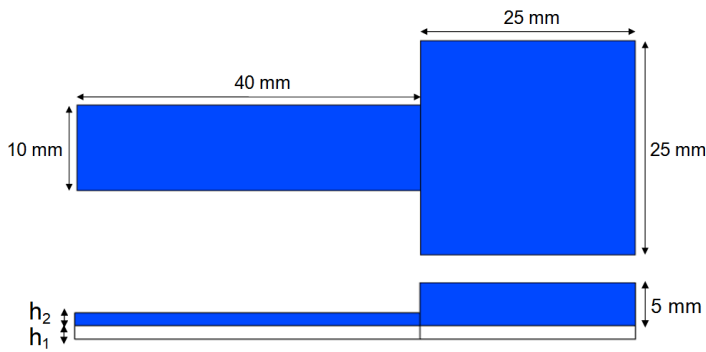


Figure 7.2: Sample dimensions (blue: ABS, white: TPU)

Table 7.2: Sample group dimensions

Sample label	$h_1$ (mm)	$h_2$ (mm)
A	0.48	0.48
B	0.24	0.24
C	0.96	0.98
D	0.96	0.48
E	0.48	0.96

### 7.3 Printing process

The samples are printed with an 3NTR A4V3 3D-printer. It has a high resolution, with a positioning precision of  $11 \mu\text{m}$  on the  $x, y$ -plane and  $5 \mu\text{m}$  on the  $z$ -axis. The maximum dimensions of a printed sample are  $300 \times 200 \times 200 \text{ mm}$ . It uses a Fused Filament Fabrication (FFF) method, where layers of molten polymer are deposited through a nozzle. The printer is equipped with a three extruders, which allows for printing with three different materials at the same time. Besides TPU (NinjaFlex Snow White by NinjaTek) and ABS (Filofalfa), High Impact PolyStyrene (HIPS) is used as a support material. The TPU layer is printed directly on top of the HIPS base. HIPS is selected specifically for its chemical compatibility with TPU, which allows the two materials to stick together during printing and to easily detach once the temperature has lowered, in order to avoid damages during the removal of the sample from the HIPS base. To translate the computer aided design into a set of instructions for the printer, a so-called slicer is used with a dedicated printing profile (Cura 4.7). The main challenge in the development of the printing profile is to guarantee a good adhesion between ABS and TPU, which is mainly affected by temperatures and velocities. The following slicer settings are used:

- The layer thickness is set to  $0.24 \text{ mm}$ , to ensure the highest dimensional accuracy according to the printer motor units' resolution;
- The extrusion width is set to  $0.4 \text{ mm}$ , which is the same value as the minimum feature size of the topology optimization designs;
- The infill type is set to rectilinear, with extrusion lines parallel to the longest side of the beam;
- The number of perimeters is set to one.

In most publications from the state-of-the-art, the prestress is introduced by exposing the active material to UV-light. This causes crosslinking reactions in the material that lead to a prestress. The prestress induction mechanism in FFF is different: here, the working principle is based on the temperature gradient. The employed polymers tend to expand when heated, while cooling causes them to shrink. Therefore, the prestress in the material is highly dependent on the printing temperature. The printing process allows for controlling the temperature at which the materials are deposited. The ABS, TPU and HIPS are printed at  $240^\circ\text{C}$ ,  $230^\circ\text{C}$  and  $250^\circ\text{C}$  respectively. The prestress is also affected by the printing velocity. The printing velocity is set to

20 mm/s for TPU and ABS, and to 40 mm/s for HIPS. Small variations in velocities are present for different printing works (e.g. slightly lower for the first layer or perimeters). All printed samples are shown in Figure 7.4.

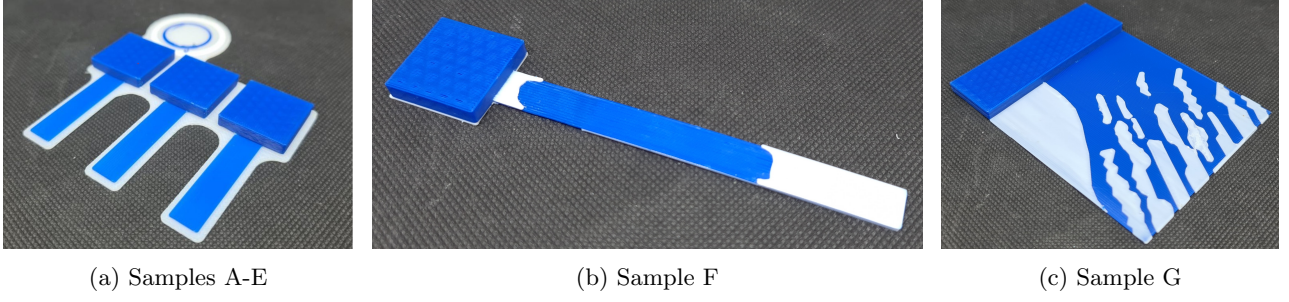


Figure 7.4: Printed samples

## 7.4 Method

This section describes the methodology of the experiments as executed at the 3D-printing laboratory of the University of Pavia. To control the sample temperature, an open heating bath circulator is used (type Corio C by Julabo). The heating bath with integrated thermometer is shown in Figure 7.5 and its specifications are listed in Table 7.3. The water in the tank is constantly stirred and therefore the water temperature can be assumed to be uniform. Thus, the water temperature can easily be controlled without the need to calibrate. The sample is clamped inside the water tank as shown in Figure 7.6. The water is heated from an initial temperature of 20°C (room temperature) to a final temperature of 98° C. The heating process has a duration of approximately five minutes. When the final temperature is reached, the samples can be removed from the water to measure the displacement using a caliper. Three samples are tested for each group label A-E. After immersion, the deflection of each of these beam-shaped samples is measured. For group labels F and G, one sample was tested and measured.



Figure 7.5: Open heating bath circulator

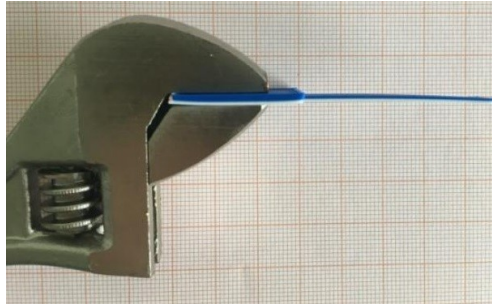


Figure 7.6: Clamping mechanism

Table 7.3: Corio C-BT9 specifications

Property	Value
Heating capacity	2 kW
Working temperature range	20-100 °C
Filling volume	6-9 L
Dimensions	320 x 380 x 380 mm

## 7.5 Results

The data obtained from the first set of experiments contain the relation between layer heights  $h_1$  and  $h_2$ , and vertical tip displacement  $v$ . For each sample group, three samples are printed and tested. This means that  $n = 3$  data points are found for every sample group. The mean of these data points can be found as follows:

$$\mu = \frac{1}{n} \left( \sum_{i=1}^n v_i \right) = \frac{v_1 + v_2 + v_3}{3}. \quad (7.1)$$

Subsequently, the standard deviation can be calculated using the following equation:

$$S = \sqrt{\frac{1}{n-1} \sum_{i=1}^n |v_i - \mu|^2}. \quad (7.2)$$

A complete overview of the experimental data, the mean displacement results for each sample group and the standard deviations can be found in Table 7.4. A number of data points of  $n = 3$  is rather small for calculating

the standard deviation, although it yields an insight in the reliability of the measurements. Ideally, a larger number of samples should be printed and tested to get a more precise image of the accuracy.

Table 7.4: Experimental results, means and standard deviations. All values in the table are in mm.

Size parameters		Experimental results			Mean	Standard deviation
$h_1$	$h_2$	$v_1$	$v_2$	$v_3$		
0.48	0.48	7.40	8.71	8.57	8.23	0.72
0.24	0.24	24.52	22.24	22.20	22.99	1.33
0.96	0.96	3.28	3.70	3.70	3.56	0.24
0.48	0.96	2.10	2.10	2.00	2.07	0.06
0.96	0.48	7.20	7.50	8.90	7.87	0.91

The averaged displacement results of each sample group are shown in Table 7.6. The temperature range, the material properties, and the sample dimensions are adapted in the numerical model to match the conditions of the experiments. Numerical simulations are run for different prestress values, ranging from 230 kPa to 310 kPa. This range of prestresses corresponds to compressive prestrains of around 0.02-0.03, which are common values for prestrain introduced by a direct 4D-printing process (Ding et al., 2017). The absolute deviations (AD), or the differences between the mean experimental displacement results and the numerical displacement results, are calculated for each sample group. The average absolute deviation is calculated for each prestress value and plotted in Figure 7.7a. Numerical data can be found in Table 7.5.

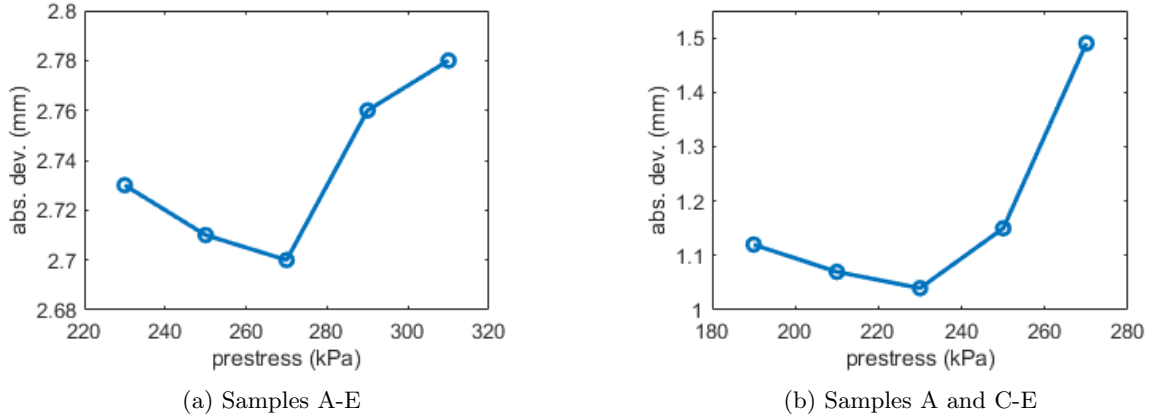


Figure 7.7: Absolute deviation from experimental results for different prestress values

Table 7.5: Displacement ( $v$ ) results and absolute deviations (AD) for different prestress values. All values are given in mm.

Size parameters		Experimental results	Numerical results									
$h_1$	$h_2$		230 kPa		250 kPa		270 kPa		290 kPa		310 kPa	
		$v$	$v$	AD	$v$	AD	$v$	AD	$v$	AD	$v$	AD
0.48	0.48	8.23	7.38	0.85	7.69	0.54	8.60	0.37	8.87	0.64	9.44	1.21
0.24	0.24	22.99	13.52	9.47	14.06	8.93	15.44	7.55	15.96	7.03	17.69	5.30
0.96	0.96	3.56	3.76	0.20	3.93	0.37	4.41	0.85	4.55	0.99	4.86	1.30
0.48	0.96	2.07	1.77	0.30	1.84	0.23	2.07	0.00	2.14	0.07	2.29	0.22
0.96	0.48	7.87	10.89	3.02	11.33	3.46	12.60	4.73	12.97	5.10	13.75	5.88
<b>Average absolute deviation</b>			2.77		2.71		2.70		2.76		2.78	

The prestress for which the average absolute deviation is minimal, is chosen as the calibrated prestress. From the numerical simulations can be concluded that this is the case for  $\sigma_0 = 270$  kPa. The numerical results obtained using this calibrated prestress are shown in Table 7.6, along with their absolute and relative deviation with respect to the experimental results. Figure 7.8a shows the experimental and numerical displacement results for all sample groups. The error bars on the experimental results represent the standard deviation. The error bars

on the computational data are based on the deviations from established data that were found when validating the 2D and 3D modeling approach, as described in Sections 3.4 and 4.3.

Table 7.6: Experimental and numerical results of samples A-E ( $\sigma_0 = 270$  kPa)

Sample label	Experiment	Numerical (2D)			Numerical (3D)		
	$v$ (mm)	$v$ (mm)	AD (mm)	RD (%)	$v$ (mm)	AD (mm)	RD (%)
A	8.23	7.57	0.66	8.0	8.60	0.37	4.0
B	22.99	14.41	8.58	37	15.44	7.55	33
C	3.56	3.82	0.26	7.3	4.41	0.85	24
D	7.87	10.57	2.70	34	12.60	4.73	60
E	2.07	1.85	0.22	11	2.07	0.00	0.0

Overall, the numerical and experimental results show a good match. The average absolute relative deviation is 2.7 mm. However, the simulation did not perform well for sample group B and, to a lesser extent, for sample group D. Note that sample group B features the smallest thickness of all samples. Although the exact reason of the unexpected result for sample group B is unknown, there are several possible explanations. Firstly, the prestress introduced during printing by a thermal expansion process could be larger because of the smaller layer thickness. Secondly, the anisotropy in a thin layer could be higher. The more printing layers (e.g. the thicker the layers) the more the anisotropy in a single layer is evened out, until at a certain point in-plane isotropy can be assumed. The thinnest sample may not have enough layers to assume an in-plane isotropic material model. Lastly, the diverging result can be caused by assumptions made in the modeling approach, such as the linear elastic material model. If the result of sample B would be considered an outlier, it can be omitted, which leads to an average absolute deviation of 1.49 mm for a prestress of 270 kPa. However, if one of the datapoints is excluded, the calibrated prestress will change. Figure 7.7b shows the absolute deviation for the remaining datapoints, which is minimized for the new calibrated prestress of 230 kPa. Results for this new prestress can be found in Table 7.7 and Figure 7.8b. The average absolute deviation is brought back to 1.04 mm. This means the modeling approach is capable of approximating the deformation of 4D-printed structures with layer thicknesses between 0.5 mm and 1 mm within a reasonable error margin.

Table 7.7: Experimental and numerical results of samples A and C-E ( $\sigma_0 = 230$  kPa)

Sample label	Experiment	Numerical (2D)			Numerical (3D)		
	$v$ (mm)	$v$ (mm)	AD (mm)	RD (%)	$v$ (mm)	AD (mm)	RD (%)
A	8.23	6.61	1.62	20	7.11	1.12	14
C	3.56	3.31	0.25	7.0	3.61	0.05	1.4
D	7.87	8.97	1.10	14	10.49	0.37	33
E	2.07	1.62	0.45	22	1.70	2.62	18

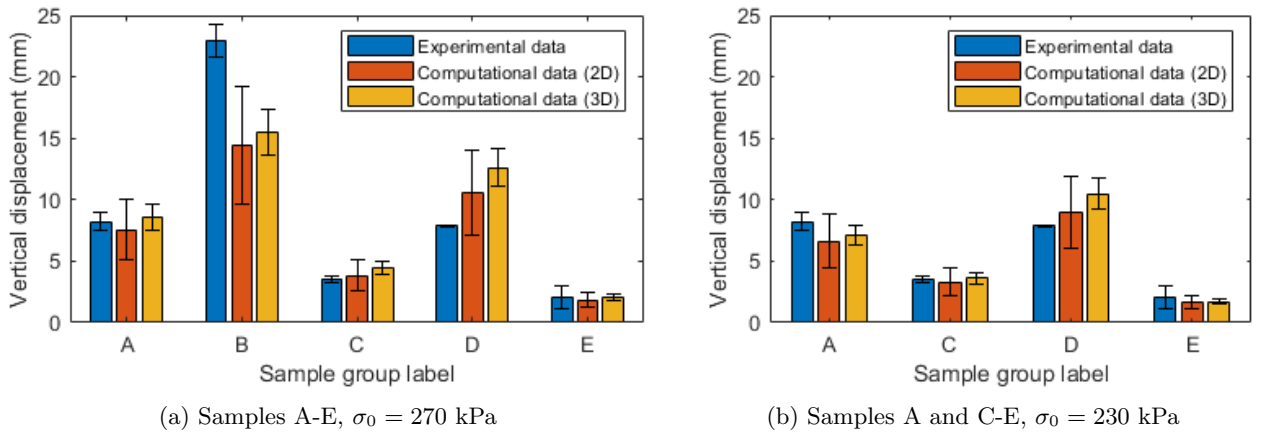


Figure 7.8: Comparison of experimental and numerical results

When the printing stress was found and the modeling approach was validated by the experimental results, a

second round of tests was performed with topology optimized samples F and G. These designs were generated using the calibrated prestress of 270 kPa. The performance of the topology optimized designs is shown in Table 7.8. For sample F, probe point 1 is located in the middle of the beam and probe point 2 is located at the tip. In this sample, bending occurs where the sample has only a single passive layer (indicated as section I in Figure 7.9a). Because of this unexpected behaviour, the experimental displacements are much larger than predicted by the numerical model. This bending can be caused by the effect of environmental factors, such as gravity or drag forces due to stirring of the water in the tank. Another possibility is that there is a gradient prestress in the passive layer which causes the bending. The numerical model that was used to obtain the results in Table 7.8 was slightly adapted, such that it accounts for gravitational effects. With these effects included the approximation is improved, but the displacements are still underestimated in the simulation. Apart from the single material section (section I), the experimental and numerical deformations appear similar. The deformation of sample G is shown in Figure 7.10, where probe point 1 is the left free corner and probe point 2 is the right free corner. The difference in displacement between these two points indicates the amount of twist, which is larger in the printed sample. Accounting for gravitational forces improves the simulation results slightly. The difference in amount of twist could be explained by the same unforeseen effects as for sample F. But in addition, the fact that this sample is very irregular could affect the prestress distribution in the active material.

Table 7.8: Experimental and numerical results of samples F and G

Sample label	Experiment		Numerical		Absolute deviation			Relative deviation		
	$v_{1,exp}$ (mm)	$v_{2,exp}$ (mm)	$v_{1,num}$ (mm)	$v_{2,num}$ (mm)	$v_1$ (mm)	$v_2$ (mm)	avg. (mm)	$v_1$ (%)	$v_2$ (%)	avg. (%)
F	-30	-53	-12.6	-18.6	17	34	26	57	64	60
G	-15	-26	-15.8	-19.0	1	7	4	7	27	17

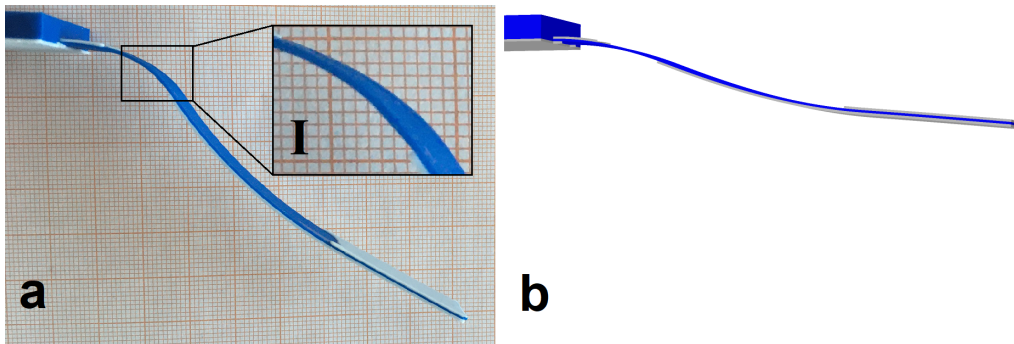


Figure 7.9: Sample F deformation, a) experimental, b) numerical (gravitational effects included)

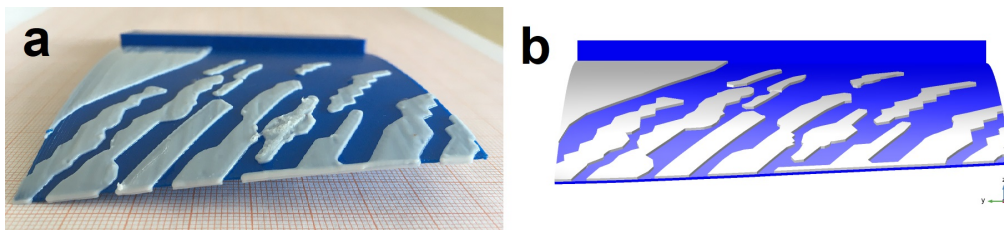


Figure 7.10: Sample G deformation, a) experimental, b) numerical (gravitational effects included)

# Chapter 8

## Conclusion and Outlook

### 8.1 Conclusion

This thesis is the result of an exploration of the possibilities for the use of topology optimization to design 4D-printed structures. Concluding from the background information that was gathered about 4D-printing, printing with bi-layer amorphous polymers to exploit the glass transition principle is well suited for creating stiff and stable structures that can potentially be used for structural applications. This specific type of 4D-printed structures comprises a glassy and a rubbery polymer layer, of which the latter is prestressed. Upon the increase of temperature, the stiffness of the glassy polymer drops, causing the structure to transform into another configuration. After analyzing the current state-of-the-art, it was found out that, although some progress in the area of research had already been made, there were still enough challenges left. Current modeling and topology optimization approaches are highly complex, and thus one of the challenges is to find a simpler approach. Furthermore, a larger variety of objective functions and displacements can be targeted to demonstrate the possibilities of this area of research.

A 2D modeling approach to simulate the transformation of bi-layered 4D-printed structures was developed using commercial software. As opposed from state-of-the-art approaches, a linear elastic material model was adopted, which makes the simulations less complex and less computationally intensive. From convergence studies, it was learned that this problem should ideally be discretized by quadratic finite elements with a characteristic length equal to the layer height of the structures. Here, the trade-off between precision and computation time was taken into account. The approach was validated using published and analytical data. It can be concluded that the numerical simulation results match well with these data, especially for low strain values. This can be explained by the fact that a linear elastic material model is used, which is usually only valid for small strains. After a proof of concept in 2D, the approach was extended to 3D. Convergence studies showed again that quadratic elements provide a sufficiently high precision. Simulation data were compared to the same published and analytical data as before, and again the deviations were small.

A density-based topology optimization method was adopted to describe the optimization problem in both 2D and 3D. A multiobjective approach was introduced, balancing deformed shape accuracy with usage of the active material. A weighted sum formulation was used to cast this into a single-objective problem, and it was found that the material usage weight factor directly influenced the resulting design. Through numerical tests, a suitable value was identified for which the density-based approach was able to produce well-defined solid-void domains. The capabilities of this topology optimization approach were shown by several variations of the original. It was expanded to e.g. design problems aimed at matching the displacements of multiple points in the material domain to multiple target displacements. Another variation was to match an entire surface to a target function. Two-way transformation was also simulated using the modeling approach, by introducing a second prestress in the glassy polymer. It was demonstrated that, besides bending transformation, a twisting transformation could be obtained by changing the target displacement settings in the optimization. The number of layers was expanded, such that the range of target displacements became larger. This way, more complex target shapes could be obtained, such as expanding lattices.

In addition to validating with published and analytical data, the 3D simulation results were validated with experiments. The printing prestress was calibrated first, since it is highly dependent on many printing parameters such as temperature and velocity. By minimizing the differences between experimental and numerical results,

the calibrated prestress was found. It was concluded from this first round of experiments that the numerical model performs best for layer sizes of 0.5 mm and 1 mm, and that smaller layer sizes show a high deviation. Using the calibrated prestress, new topology optimized designs were generated, printed and tested. From these tests was concluded that single layer sections behave differently from what was expected. It was found out that gravity plays a role, but the deformation is further influenced by other factors such as additional forces, disturbances and environmental factors during the experiments. Apart from the single layer sections, numerical and experimental results appear similar. Although this experimental validation partly raises new questions, it can be considered a confirmation of the appropriateness of the developed modeling and optimization method for 4D printed structures. Moreover, by using this method to explore a range of design problems, the aim of this thesis has been reached.

## 8.2 Future work

To further improve on the presented approach to use topology optimization for 4D-printed structures, many opportunities for future work exist. These opportunities can be divided in three categories: modeling, topology optimization and experiments.

- Modeling:
  - It could be investigated if a hyperelastic material model obtains results that resemble the experimental results better than a linear elastic material model.
  - The role played by anisotropy in the printed materials can be looked into.
  - Factors in the testing environment, such as drag forces caused by stirring of the water, gravity and heat transfer might also play a role. These factors were all neglected in the current work.
  - If enough computational power is available, more extreme deformations can be looked into by simulating geometries with smaller layer heights.
- Topology optimization:
  - The modeling and topology optimization approach can be taken to a next level by aiming for more complex target displacements.
  - To further increase the design freedom of the optimizer, a material optimization could be used instead of using fixed material domains as a starting point for the topology optimization. By doing this, structures of increased complexity can be generated.
  - Structures can be optimized such that they aim to match different desired shapes at multiple pre-defined temperatures instead of only at the final temperature, to obtain a multi-stage transformation.
- Experiments:
  - Doing more experiments with a larger number of samples would help in getting a greater insight in the accuracy of the measurements and the performance of the modeling approach.
  - Although the numerical model is capable of predicting the transformations at intermediate temperature values, intermediate deformations were not measured during the experiments. Filming the transformation of the samples gains new data that can be used to further validate the modeling approach.
  - Experiments with two-way transforming structures may lead to new insights and possibilities.
  - Unforeseen effects of the testing environment could be circumvented by changing the test setup. The samples could be oriented such that gravity plays a smaller role and the need for a stirred water tank could be avoided.
  - In the prestress calibration method used in the current work, the minimum difference between the experimental and numerical result is picked out manually. A more elegant solution is to use parameter optimization to find the correct prestress.
  - The dependence of prestress on layer thickness can be investigated to be able to accurately compare the numerical and experimental results;

Besides this thesis, the research that was done during this graduation project has lead to another product: a paper titled “*Modeling, Topology Optimization and Experimental Validation of Glass-Transition-Based 4D-Printed Polymeric Structures*”, which was written in collaboration with Giulia Scalet, Stefania Marconi, Ferdinando Auricchio and Matthijs Langelaar. Another future activity related to this work is to present this paper to the

conference “*11th Int. Conference on Couple Problems in Science and Engineering (COUPLED 2021)*”. It will be held in Chia Laguna, South Sardinia, Italy on 13-16 June, 2021. The paper can be found as published in Appendix A.4.

# Bibliography

- Ahmed, E. M. (2015). Hydrogel: Preparation, characterization, and applications: A review. *Journal of Advanced Research*, 6(2):105–121.
- Akbari, S., Sakhaei, A. H., Kowsari, K., Yang, B., Serjouei, A., Yuanfang, Z., and Ge, Q. (2018). Enhanced multimaterial 4D printing with active hinges. *Smart Materials and Structures*.
- Amestoy, P. R., Duff, I. S., L'Excellent, J.-Y., and Koster, J. (2000). MUMPS: A General Purpose Distributed Memory Sparse Solver.
- Bendsoe, M. and Sigmund, O. (2003). *Topology Optimization - Theory, Methods and Applications*. Springer-Verlag Berlin Heidelberg.
- Bendsøe, M. P. (1989). Optimal Shape Design as a Material Distribution Problem. *Structural Optimization*, 1(January 1989):193–202.
- Bodaghi, M., Damanpack, A. R., and Liao, W. H. (2016). Self-expanding/shrinking structures by 4D printing. *Smart Materials and Structures*, 25(10).
- Bodaghi, M., Serjouei, A., Zolfagharian, A., Fotouhi, M., Rahman, H., and Durand, D. (2020). Reversible energy absorbing meta-sandwiches by FDM 4D printing. *International Journal of Mechanical Sciences*, 173(September 2019).
- Boley, J., van Rees, W., Lissandrello, C., Horenstein, M., Truby, R., Kotikian, A., Lewis, J., and Mahadevan, L. (2019). Shape-shifting structured lattices via multimaterial 4d printing. *Proceedings of the National Academy of Sciences*, 116:201908806.
- Briassoulis, D. (1989). On the basics of the shear locking problem of c0 isoparametric plate elements. *Computers & Structures*, 33(1):169 – 185.
- Carrell, J., Tate, D., Wang, S., and Zhang, H. C. (2011). Shape memory polymer snap-fits for active disassembly. *Journal of Cleaner Production*, 19(17-18):2066–2074.
- Chen, T., Bilal, O. R., Lang, R., Daraio, C., and Shea, K. (2019). Autonomous Deployment of a Solar Panel Using Elastic Origami and Distributed Shape-Memory-Polymer Actuators. *Physical Review Applied*, 11(6).
- COMSOL (2008). Structural Mechanics Module. <https://doc.comsol.com/5.4/doc/com.comsol.help.sme/StructuralMechanicsModuleUsersGuide.pdf>.
- COMSOL (2018). Optimization Module. <https://doc.comsol.com/5.4/doc/com.comsol.help.opt/OptimizationModuleUsersGuide.pdf>.
- Ding, Z., Yuan, C., Peng, X., Wang, T., Qi, H. J., and Dunn, M. L. (2017). Direct 4D printing via active composite materials. *Science Advances*, 3(4).
- Fernandes, R. and Gracias, D. H. (2012). Self-folding polymeric containers for encapsulation and delivery of drugs. *Advanced Drug Delivery Reviews*, 64(14):1579–1589.
- Frei, W. (2013a). Solutions to linear systems of equations: Direct and iterative solvers. <https://www.comsol.com/blogs/solutions-linear-systems-equations-direct-iterative-solvers/>. Accessed: 1-08-2020.
- Frei, W. (2013b). Solving nonlinear static finite element problems. <https://www.comsol.com/blogs/solving-nonlinear-static-finite-element-problems/>. Accessed: 1-08-2020.

- Frei, W. (2017). How to compute distances between objects in comsol multiphysics. <https://www.comsol.com/blogs/how-to-compute-distances-between-objects-in-comsol-multiphysics/>. Accessed: 1-08-2020.
- Fuchi, K., Ware, T. H., Buskohl, P. R., Reich, G. W., Vaia, R. A., White, T. J., and Joo, J. J. (2015). Topology optimization for the design of folding liquid crystal elastomer actuators. *Soft Matter*, 11(37).
- Ge, Q., Sakhaei, A. H., Lee, H., Dunn, C. K., Fang, N. X., and Dunn, M. L. (2016). Multimaterial 4D Printing with Tailorable Shape Memory Polymers. *Scientific Reports*, 6(August):1–11.
- Geiss, M. J., Boddeti, N., Weeger, O., Maute, K., and Dunn, M. L. (2019). Combined Level-Set-XFEM-Density Topology Optimization of Four-Dimensional Printed Structures Undergoing Large Deformation. *Journal of Mechanical Design, Transactions of the ASME*, 141(5):1–14.
- Geiss, M. J. and Maute, K. (2018). Topology optimization of active structures using a higher-order level-set-XFEM-density approach. *2018 Multidisciplinary Analysis and Optimization Conference*, pages 1–13.
- Hager, M. D., Bode, S., Weber, C., and Schubert, U. S. (2015). Shape memory polymers: Past, present and future developments. *Progress in Polymer Science*, 49-50:3–33.
- Hamel, C. M., Roach, D. J., Long, K. N., Demoly, F., Dunn, M. L., and Qi, H. J. (2019). Machine-learning based design of active composite structures for 4D printing. *Smart Materials and Structures*, 28(6).
- Huang, W., Zhao, Y., Wang, C. C., Ding, Z., Purnawali, H., Tang, C., and Zhang, J. (2012). Thermo/chemo-responsive shape memory effect in polymers: a sketch of working mechanisms, fundamentals and optimization. *Journal of Polymer Research*, 19(September):1–34.
- Inverardi, N., Pandini, S., Bignotti, F., Scalet, G., Marconi, S., and Auricchio, F. (2020). Sequential Motion of 4D Printed Photopolymers with Broad Glass Transition. *Macromolecular Materials and Engineering*, 305(1):1–11.
- Ionov, L. (2011). Soft microorigami: Self-folding polymer films. *Soft Matter*, 7(15):6786–6791.
- Kindo, T. (2015). Accessing Nonlocal Variables with Linear Extrusion Operators. <https://www.comsol.com/blogs/accessing-non-local-variables-with-linear-extrusion-operators/>. Accessed: 01-11-2020.
- Kwok, T. H., Wang, C. C., Deng, D., Zhang, Y., and Chen, Y. (2015). Four-Dimensional Printing for Freeform Surfaces: Design Optimization of Origami and Kirigami Structures. *Journal of Mechanical Design, Transactions of the ASME*, 137(11):1–10.
- Lazarov, B. and Sigmund, O. (2011). Filters in topology optimization based on helmholtz-type differential equations. *International Journal for Numerical Methods in Engineering*, 86(6):765–781.
- Lee, A. Y., An, J., and Chua, C. K. (2017). Two-Way 4D Printing: A Review on the Reversibility of 3D-Printed Shape Memory Materials. *Engineering*, 3(5):663–674.
- Liu, J., Gaynor, A. T., Chen, S., Kang, Z., Suresh, K., Takezawa, A., Li, L., Kato, J., Tang, J., Wang, C. C., Cheng, L., Liang, X., and To, A. C. (2018). Current and future trends in topology optimization for additive manufacturing. *Structural and Multidisciplinary Optimization*, 57(6):2457–2483.
- Liu, Y. and Hu, H. (2010). A review on auxetic structures and polymeric materials. *Scientific research and essays*, 5:1052–1063.
- Mahieux, C. A. and Reifsnider, K. L. (2001). Property modeling across transition temperatures in polymers: A robust stiffness - Temperature model. *Polymer*, 42(7):3281–3291.
- Maute, K., Tkachuk, A., Wu, J., Qi, H. J., Ding, Z., and Dunn, M. L. (2015). Level Set Topology Optimization of Printed Active Composites. *Journal of Mechanical Design, Transactions of the ASME*, 137(11).
- Melocchi, A., Uboldi, M., Inverardi, N., Briatico-Vangosa, F., Baldi, F., Pandini, S., Scalet, G., Auricchio, F., Cerea, M., Foppoli, A., Maroni, A., Zema, L., and Gazzaniga, A. (2019). Expandable drug delivery system for gastric retention based on shape memory polymers: Development via 4d printing and extrusion. *International Journal of Pharmaceutics*, 571:118700.
- Miao, S., Castro, N., Nowicki, M., Xia, L., Cui, H., Zhou, X., Zhu, W., jun Lee, S., Sarkar, K., Vozzi, G., Tabata, Y., Fisher, J., and Zhang, L. G. (2017). 4D printing of polymeric materials for tissue and organ regeneration.

- Momeni, F., M.Mehdi Hassani, N. S., Liu, X., and Ni, J. (2017). A review of 4D printing. *Materials and Design*, 122:42–79.
- Ngo, T. D., Kashani, A., Imbalzano, G., Nguyen, K. T., and Hui, D. (2018). Additive manufacturing (3D printing): A review of materials, methods, applications and challenges. *Composites Part B: Engineering*, 143(December 2017):172–196.
- Selva-Priya, M., Naresh, K., Jayaganthan, R., and Velmurugan, R. (2019). A comparative study between in-house 3d printed and injection molded ABS and PLA polymers for low-frequency applications. *Materials Research Express*, 6(8):085345.
- Shettar, R. and Sheeparamatti, G. (2013). Excerpt from the Proceedings of the 2013 COMSOL Conference in Bangalore Modeling and Analysis of Thermal Bimorph Using COMSOL.
- Shin, D. G., Kim, T. H., and Kim, D. E. (2017). Review of 4D printing materials and their properties. *International Journal of Precision Engineering and Manufacturing - Green Technology*, 4(3):349–357.
- Shrivastava, A. (2018). Introduction to Plastics Engineering. *Introduction to Plastics Engineering*, pages 1–16.
- Sigmund, O. and Maute, K. (2013). Topology optimization approaches: A comparative review. *Structural and Multidisciplinary Optimization*, 48(6):1031–1055.
- Sossou, G., Demoly, F., Belkebir, H., Qi, H. J., Gomes, S., and Montavon, G. (2019). Design for 4D printing: Modeling and computation of smart materials distributions. *Materials and Design*, 181:108074.
- Stolpe, M. and Svanberg, K. (2001). An alternative interpolation scheme for minimum compliance topology optimization. *Struct. Multidiscip. Optim.*, 22(2):116–124.
- Sydney Gladman, A., Matsumoto, E. A., Nuzzo, R. G., Mahadevan, L., and Lewis, J. A. (2016). Biomimetic 4D printing. *Nature Materials*, 15(4):413–418.
- Taylor, D. L. and in het Panhuis, M. (2016). Self-Healing Hydrogels. *Advanced Materials*, 28(41):9060–9093.
- Tibbits, S. (2014). 4D printing: Multi-material shape change. *Architectural Design*, 84(1):116–121.
- Tolley, M. T., Felton, S. M., Miyashita, S., Aukes, D., Rus, D., and Wood, R. J. (2014). Self-folding origami: Shape memory composites activated by uniform heating. *Smart Materials and Structures*, 23(9).
- Van Dijk, N. P., Maute, K., Langelaar, M., and Van Keulen, F. (2013). Level-set methods for structural topology optimization: A review. *Structural and Multidisciplinary Optimization*, 48(3):437–472.
- Wang, F., Lazarov, B., and Sigmund, O. (2011). On projection methods, convergence and robust formulations in topology optimization. *Structural and Multidisciplinary Optimization*, 43(6):767–784.
- Wang, Y., Luo, Z., Kang, Z., and Zhang, N. (2015). A multi-material level set-based topology and shape optimization method. *Computer Methods in Applied Mechanics and Engineering*, 283:1570–1586.
- Willems, B., Dewulf, W., and Dufflou, J. R. (2007). Active snap-fit development using topology optimization. *International Journal of Production Research*, 45(18-19):4163–4187.
- Wu, J., Yuan, C., Ding, Z., Isakov, M., Mao, Y., Wang, T., Dunn, M. L., and Qi, H. J. (2016). Multi-shape active composites by 3D printing of digital shape memory polymers. *Scientific Reports*, 6(November 2015):1–11.
- Zhou, Y. and Min, W. (2015). Shape memory effect in polymeric materials : mechanisms and optimization. *Procedia IUTAM*, 12:83–92.
- Zolfagharian, A., Denk, M., Bodaghi, M., Kouzani, A. Z., and Kaynak, A. (2019). Topology-Optimized 4D Printing of a Soft Actuator. *Acta Mechanica Solida Sinica*, 33:418–430.

# Appendix A

## Appendix

### A.1 Single material 4D-printing with amorphous polymers

The single material 4D-printing technique called **dual-state mechanism (DSM)** exploits the glass transition temperature  $T_g$  of polymers, where ‘dual-state’ refers to the rubbery and glassy states of the material (Zhou and Min, 2015; Lee et al., 2017). The printed structure is heated above  $T_g$ , such that it becomes rubbery, and is deformed by applying a load to introduce a prestress. While maintaining the deformation, the temperature is lowered below  $T_g$ . The material becomes glassy again and will largely remain in the deformed state. The resulting product of this printing and programming process is a one-way shape memory polymer (SMP). The SMP will not change its shape until it is heated above  $T_g$ , which will permanently transform the SMP into the originally printed shape. Another single material 4D-printing method is the so-called **partial-transition mechanism (PTM)** (Huang et al., 2012). Here, the structure is only partially heated. This causes some parts of the structure have a rubbery behaviour and some parts to have a glassy behaviour. A prestress is stored in the material in the same way as described for the DSM technique. The structure will deform once heated to a temperature within the transition range.

### A.2 Genetic algorithm topology optimization methods

Topology optimization in 4D-printing can be done with a heuristic approach, such as the use of a Genetic Algorithm (GA). This type of algorithm is based on the principle of evolution. A population of  $\mu$  candidate solutions are created and their performance is tested with a fitness function  $F$ . A new generation is created based on the best performing candidate functions from  $\mu$ . The candidate functions that were not selected can crossover and/or mutate, depending on the type of GA. This process is repeated until the fitness function value  $F$  is below a certain threshold. Compared to the other methods, GA is somewhat computationally inefficient and time-consuming. The GA method is used by Hamel et al. (2019) and Sossou et al. (2019) to perform topology optimization. Both publications are limited to a low design resolution and two or three different materials and no void. More information about these studies can be found in Section 2.4: ‘*State-of-the-art*’.

### A.3 Solver settings

For the 2D model, a multifrontal massively parallel sparse direct solver (MUMPS) is used. This type of solver is suitable for a wide range of problems (Amestoy et al., 2000), which is why it is the default solver in COMSOL. It is a direct solver, which uses matrix factorization to directly solve systems of the form  $\mathbf{K}\mathbf{u} = \mathbf{p}$ . For geometrical nonlinear problems, it is recommended to ramp up a loading parameter to its final value in sufficiently small steps to solve the problem incrementally (COMSOL, 2008). By doing this, the solver will converge towards the correct solution. In the problem that is modeled here, either the temperature or the prestress loading parameters could be used for this purpose. The temperature loading parameter is already incremental and this is sufficient to make the solver converge to the correct solution. Therefore, there is no need to ramp up another loading parameter.

By default, COMSOL uses the ‘automatic’ Newton-Raphson nonlinear method. This method can find the roots of a function vector of the form  $f(\mathbf{u}) = \mathbf{p} - \mathbf{K}(\mathbf{u})\mathbf{u}$ : it finds  $\mathbf{u}$  such that  $f(\mathbf{u}) = \mathbf{0}$ . To begin with, an initial solution  $\mathbf{u}_0$  should be found. In this study, the initial solution is chosen as zero. The following equation is used to calculate the first iteration:

$$\mathbf{u}_1 = \mathbf{u}_0 - J_f(\mathbf{u}_0)^{-1}f(\mathbf{u}_0), \quad (\text{A.1})$$

where  $J_f(\mathbf{u}_0)$  is the Jacobian matrix, defined over the function vector  $f(\mathbf{u})$ . The process is continued with more iterations using the following equation:

$$\mathbf{u}_{n+1} = \mathbf{u}_n - J_f(\mathbf{u}_n)^{-1}f(\mathbf{u}_n), \quad (\text{A.2})$$

until the value of  $f(\mathbf{u})$  is below a certain threshold. It is desirable that for every iteration, the solution of  $f(\mathbf{u})$  gets closer to zero, or in other words:  $|f(\mathbf{u}_{n+1})| < |f(\mathbf{u}_n)|$ . However in some cases, an iteration can be steered towards a region where there are no roots. This could cause the problem to not converge at all. Once it is detected that the solution is diverging from the root (when  $|f(\mathbf{u}_{n+1})| > |f(\mathbf{u}_n)|$ ), COMSOL adds an extra step to the algorithm. It finds  $\mathbf{u}_{damped}$  for  $|f(\mathbf{u}_{damped})| < |f(\mathbf{u}_n)|$ :

$$\mathbf{u}_{damped} = \mathbf{u}_n + \alpha(\mathbf{u}_{n+1} - \mathbf{u}_n), \quad (\text{A.3})$$

where  $0 < \alpha \leq 1$  is a damping factor. If  $\alpha = 1$ , there is no damping. The default method in COMSOL is referred to as ‘automatic’, because it automatically finds a suitable damping factor for every iteration. Although the introduction of this damping factor improves convergence, it decreases the computational speed because of the extra computation steps per iteration. Therefore, problems with large deformations and/or many degrees of freedom require a slightly different approach to speed up the computation process. The damping factor is set to a constant value of 1, which means there is no damping at all. In COMSOL, this approach is called the constant Newton method (Frei, 2013b).

The solver settings of the topology optimization study do are very similar to the initial study solver settings. One difference is that the topology optimization uses the solution of the initial study as the initial solution. In addition to that, the optimization module has its own solver where the method of moving asymptotes (MMA) is used. MMA is an iterative method, meaning that the solution is approached in steps.

In the 2D model, the number of degrees of freedom is low enough to use a direct solver. However in the 3D model, the number of degrees of freedom is much larger. With an iterative solver method, the solution is approached in steps. The memory cost of this method is much smaller than that of a direct method. Therefore, an iterative solver is preferred for large 3D models such as the model that is described in this chapter. A downside of iterative solvers is that they are more sensitive and do not converge as easily as direct solvers (Frei, 2013a). The type of iterative solver that is used is the conjugate gradients method.

## A.4 Research paper

The following six pages comprise a scientific paper titled “Modeling, Topology Optimization and Experimental Validation of Glass-Transition-Based 4D-Printed Polymeric Structures”, which is a product of the research presented in this thesis. The paper will be submitted to *11th Int. Conference on Couple Problems in Science and Engineering (COUPLED 2021)*, which will take place in Chia Laguna, South Sardinia, Italy on 13-16 June, 2021. The website of this conference can be visited using the following url:

<https://congress.cimne.com/Coupled2021/frontal/default.asp>

Please note that the research paper is not included in the thesis version that is uploaded to the TU Delft repository for copyright reasons.